

Retinal Image Analysis and its use in Medical Applications

by

Yibo Zhang

A thesis
presented to the University of Waterloo
in fulfillment of the
thesis requirement for the degree of
Doctor of Philosophy
in
Electrical and Computer Engineering

Waterloo, Ontario, Canada, 2011

© Yibo Zhang 2011

AUTHOR'S DECLARATION

I hereby declare that I am the sole author of this thesis. This is a true copy of the thesis, including any required final revisions, as accepted by my examiners.

I understand that my thesis may be made electronically available to the public.

Abstract

Retina located in the back of the eye is not only a vital part of human sight, but also contains valuable information that can be used in biometric security applications, or for the diagnosis of certain diseases. In order to analyze this information from retinal images, its features of blood vessels, microaneurysms and the optic disc require extraction and detection respectively.

We propose a method to extract vessels called MF-FDOG. MF-FDOG consists of using two filters, Matched Filter (MF) and the first-order derivative of Gaussian (FDOG). The vessel map is extracted by applying a threshold to the response of MF, which is adaptively adjusted by the mean response of FDOG. This method allows us to better distinguish vessel objects from non-vessel objects.

Microaneurysm (MA) detection is accomplished with two proposed algorithms, Multi-scale Correlation Filtering (MSCF) and Dictionary Learning (DL) with Sparse Representation Classifier (SRC). MSCF is hierarchical in nature, consisting of two levels: coarse level microaneurysm candidate detection and fine level true microaneurysm detection. In the first level, all possible microaneurysm candidates are found while the second level extracts features from each candidate and compares them to a discrimination table for decision (MA or non-MA). In Dictionary Learning with Sparse Representation Classifier, MA and non-MA objects are extracted from images and used to learn two dictionaries, MA and non-MA. Sparse Representation Classifier is then applied to each MA candidate object detected beforehand, using the two dictionaries to determine class membership. The detection result is further improved by adding a class discrimination term into the Dictionary Learning model. This approach is known as Centralized Dictionary Learning (CDL) with Sparse Representation Classifier.

The optic disc (OD) is an important anatomical feature in retinal images, and its detection is vital for developing automated screening programs. Currently, there is no algorithm designed to automatically detect the OD in fundus images captured from Asians, which are larger and have thicker vessels compared to Caucasians. We propose such a method to complement current algorithms using two steps: OD vessel candidate detection and OD vessel candidate matching.

The proposed extraction/detection approaches are tested in medical applications, specifically the case study of detecting diabetic retinopathy (DR). DR is a complication of diabetes that damages the retina and can lead to blindness. There are four stages of DR and is a leading cause of sight loss in industrialized nations. Using MF-FDOG, blood vessels were extracted from DR images, while DR

images fed into MSCF and Dictionary and Centralized Dictionary Learning with Sparse Representation Classifier produced good microaneurysm detection results. Using a new database consisting of only Asian DR patients, we successfully tested our OD detection method. As part of future work we intend to improve existing methods such as enhancing low contrast microaneurysms and better scale selection. In addition, we will extract other features from the retina, develop a generalized OD detection method, apply Dictionary Learning with Sparse Representation Classifier to vessel extraction, and use the new image database to carry out more experiments in medical applications.

Acknowledgements

First and foremost I would like to thank my Ph.D. supervisor Dr. Fakhri Karray. Without his guidance, leadership and support, this thesis and its work would not be possible. I am also grateful to my committee members, Dr. Prabir Bhattacharya, Dr. Mohamed Kamel, Dr. Zhou Wang, and Dr. Andrew Wong for their help and support.

To the members of PAMI, you have contributed immensely to my personal and professional development at Waterloo. I will always look back with fond memories. Acknowledgement also goes to the Electrical and Computer Engineering graduate studies office staff for their assistance.

Last but not least, I want to thank my parents for their unconditional love and support. I am forever indebted to them.

Table of Contents

AUTHOR'S DECLARATION	ii
Abstract	iii
Acknowledgements	v
Table of Contents	vi
List of Figures	x
List of Tables	xv
List of Abbreviations	xvii
Chapter 1 Introduction	1
1.1 The Human Eye: Rich Source of Information.....	1
1.2 Retinal Image Capture	3
1.3 Features Extracted from Retinal Images.....	5
1.3.1 Blood Vessel Features.....	5
1.3.2 Microaneurysm Features	6
1.3.3 Optic Disc Feature.....	7
1.4 Applications Spawned from Retinal Image Analysis	8
1.5 Organization.....	11
Chapter 2 Literature Review	14
2.1 Blood Vessel Extraction	14
2.1.1 Edge Detection	14
2.1.2 Filter-based.....	14
2.1.3 Mathematical Morphology.....	15
2.1.4 Geometry-based.....	15
2.1.5 Machine Learning: Supervised.....	16

2.2 Microaneurysm Detection.....	16
2.2.1 Pixel Classification.....	18
2.2.2 Mathematical Morphology.....	18
2.2.3 Fusion Technology.....	19
2.2.4 Template-based.....	19
2.2.5 Supervised Learning	20
2.3 Optic Disc Detection	21
2.3.1 Template-based.....	21
2.3.2 Supervised Learning	21
2.3.3 Property-based	22
2.3.4 Transform-based.....	22
2.3.5 Vessel Model-based	23
2.4 Assessment.....	23
2.5 Summary	24
Chapter 3 Retinal Vessel Extraction by Matched Filter with First-Order Derivative of Gaussian	25
3.1 Introduction.....	25
3.2 The Matched Filter	26
3.3 The MF-FDOG.....	27
3.4 Experimental Results.....	31
3.5 Summary	38
Chapter 4 Detection of Microaneurysms using Multi-scale Correlation Coefficients.....	40
4.1 Coarse Level: Microaneurysm Candidate Detection	40
4.2 Fine Level: True Microaneurysm Classification	46
4.3 Experimental Results and Analysis	50

4.4 Summary	57
Chapter 5 Microaneurysm Detection via Dictionary and Centralized Dictionary Learning with Sparse Representation Classifier	58
5.1 Introduction.....	58
5.2 Sparse Representation Classifier	58
5.3 Dictionary and Centralized Dictionary Learning with SRC	60
5.4 DL and CDL with SRC at MA Detection.....	62
5.5 Experimental Results.....	74
5.6 Summary	81
Chapter 6 Detecting Optic Disc on Asians by Multi-scale Gaussian Filtering and a Vessels' Directional Matched Filter.....	82
6.1 Introduction.....	82
6.2 Material.....	85
6.3 Proposed Asian OD Detection Method.....	86
6.3.1 OD Vessel Candidate Detection	86
6.3.2 OD Vessel Candidate Matching	89
6.4 Experimental Results.....	90
6.5 Discussion	92
6.6 Summary	97
Chapter 7 Future Work	99
7.1 Improvements to Current Methods.....	99
7.1.1 MF-FDOG at Vessel Detection	99
7.1.2 Enhancing Low Contrast Microaneurysms	99
7.1.3 Dictionary and Centralized Dictionary Learning with Sparse Representation Classifier..	99
7.1.4 OD Detection of Asians.....	100

7.1.5 <i>Better Scale Selection</i>	100
7.2 Future Work.....	100
7.2.1 <i>Extraction of other Retinal Features</i>	100
7.2.2 <i>Developing a General Purpose Automatic OD Detection Method</i>	100
7.2.3 <i>Conducting Further Experiments on HIT</i>	101
7.2.4 <i>Vessel Extraction via Dictionary and Centralized Dictionary Learning with SRC</i>	101
7.3 Publication List	101
7.3.1 <i>Journal Publications</i>	102
7.3.2 <i>Conference Publications</i>	102
Bibliography	104

List of Figures

Figure 1.1: Anatomy of the eye [2].	1
Figure 1.2: Concealing the identity of an individual (a) can be accomplished by covering their eyes (b).	2
Figure 1.3: Architecture of a generic retinal image analysis system.	3
Figure 1.4: Most common diabetic retinopathy screening techniques (a) FA and (b) color retinal image.	4
Figure 1.5: Canon fundus camera [36].	5
Figure 1.6: The corresponding color bands red (a), green (b) and blue (c) of the color retinal image (Fig. 1.4 (b)).	6
Figure 1.7: Two fundus images (a), (b) and its corresponding vessel map (c), (d).	7
Figure 1.8: Examples of different microaneurysms shown on the top with its equivalent green channel on the bottom.	8
Figure 1.9: Four cropped images of the optic disc.	8
Figure 1.10: What a person with normal vision (a) will see. Same scene viewed by a person with diabetic retinopathy (b) [85].	9
Figure 1.11: Retinal images to show the different stages of diabetic retinopathy.	11
Figure 1.12: The organizational structure of this document.	13
Figure 2.1: Using traditional edge detection methods to enhance retinal blood vessels Sobel (a), Prewitt (b), Roberts (c), Laplacian of Gaussian (d) and Canny (e).	17
Figure 3.1: Cross-section plot of five different retinal blood vessels. The x -axis is the cross-section width while the y -axis represents pixel intensity.	27
Figure 3.2: Responses of the MF and the FDOG to a Gaussian line cross-section and an ideal step edge. The x -axis is the cross-section width while the y -axis represents magnitude. (a) A Gaussian line cross-section and an ideal step edge; (b-1) the MF and (b-2) its filter response; (c-1) the FDOG and (c-2) its filter response; (d) the local mean of the response to the FDOG.	29

Figure 3.3: Illustration of the proposed MF-FDOG retinal vessel extraction scheme. (a) The original image im0001 from the STARE database. (b) The response map to MF. (c) The local mean of the response to FDOG. (d) The vessel extraction result after applying a global threshold to the MF response map. (e) The extraction result of the proposed scheme. (f) The ground truth vessel map. 32

Figure 3.4: (a) The original image im0002 from the STARE database; (b) The ground truth vessel map; the vessel extraction results by (c) MF; (d) Hoover [29]; (e) Soares [26]; and (f) the proposed MF-FDOG..... 33

Figure 3.5: The original image 3 from the DRIVE database; (b) The ground truth vessel map; the vessel extraction result by (c) the proposed MF-FDOG. 37

Figure 3.6: ROC curves for both STARE and DRIVE with $FP < 0.05$ by the proposed method. The solid line represents STARE while the dotted line is DRIVE..... 38

Figure 4.1: The detection of microaneurysms in a color retinal image. (a) and (b) illustrate two microaneurysms found in Fig. 1.4 (b). The corresponding mesh plots of (a) and (b) are shown in (c) and (d) respectively. 41

Figure 4.2: The mesh plots of the Gaussian kernel with different scale factors. (a) scale factor = 1 and (b) scale factor = 1.5..... 42

Figure 4.3: The responses of microaneurysms to different Gaussian kernels. (a) and (b) are responses for microaneurysms in Fig. 4.1 (a) and (b) at a small scale, (c) and (d) are responses for microaneurysms in Fig. 4.1 (a) and (b) at a larger scale, where the maximum coefficient is placed below each response. 42

Figure 4.4: The final response of a testing image. (a) the input retinal image (b) the output. 43

Figure 4.5: Result after segmenting Fig. 4.4 (b) with a threshold of 0.4. The white spots marked are possible microaneurysms. 44

Figure 4.6: The vascular map of a retinal image. (a) the sample image given in Fig. 4.4 (a) and (b) the output of its vascular map. 45

Figure 4.7: The remaining candidates from Fig. 4.5 after candidates on the blood vessels were removed. 47

Figure 4.8: Result of region growing on the candidates in Fig. 4.7.	48
Figure 4.9: Sub-band image I_{SC} obtained by subtracting I_{bg} from I_{green}	48
Figure 4.10: Matched image I_{match} which shows possible microaneurysms. This image was processed by removing vessels from Fig. 4.9 and enhancing its result with a Gaussian filter.	50
Figure 4.11: The output of microaneurysm detection. (a) the original retinal image, (b) the output of coarse-level detection and (c) the final output of fine-level classification where the green squares mark the approximate location of the detected microaneurysms using the proposed algorithm. .	51
Figure 4.12: Plot of FROC comparing MSCF (dotted curve) with Math Morph (solid curve) on the training data.	52
Figure 4.13: Plot of FROC comparing MSCF (dotted curve) with Math Morph (solid curve) on the test data.	54
Figure 4.14: True microaneurysm being recognized as part of the blood vessel. (a) A cropped retinal image marked with true microaneurysms. (b) candidates detected in (a). (c) vascular map of (a). The central microaneurysm enclosed with dashes in (a), and (b) is detected as part of the blood vessel in (c).	55
Figure 4.15: True microaneurysms with low contrast.	56
Figure 4.16: False positive microaneurysm candidates with high contrast.	57
Figure 5.1: Demonstration of the idea of SRC applied to face recognition. (a) plot of the representation coefficients vs. training samples/dictionary and (b) plot of Residual vs. Subject.	59
Figure 5.2: (a) A fundus image from the DIARETDB1 dataset and (b) its final response after Multi-scale Correlation Filtering.	63
Figure 5.3: (a) Result after thresholding and vessel removal; (b) region growing applied to (a).	64
Figure 5.4: Using an example of a MA (top) and a non-MA (bottom) from ROC training, the procedure of extracting the object and converting it into a 121×1 column vector is shown.	65
Figure 5.5: Using an example of a MA (top) and a non-MA (bottom) from DIARETDB1, the procedure of extracting the object and converting it into a 121×1 column vector is demonstrated.	67

Figure 5.6: Example of a learnt MA dictionary with 20 samples.	71
Figure 5.7: Example of a learnt non-MA dictionary with 20 samples.	71
Figure 5.8: Plot of the representation coefficients vs. dictionary elements where 1-20 are MA elements and 21-40 are non-MA elements. Since the most significant coefficient is between 1-20, the candidate is most likely a MA object.	72
Figure 5.9: Plot of the representation coefficients vs. dictionary elements where 1-20 are MA elements and 21-40 are non-MA elements. Since the most significant coefficient is between 21-40, the candidate is most likely a non-MA object.	74
Figure 5.10: Example of CDL with SRC based MA detection. (a) is a cropped MA object; (b) is its fusion $r_{MA} + d_{\phi}$ and (c) is $r_{NMA} + d_{\psi}$; (d) is the detected result by applying the rule in (5.11). We see that the MA object is well detected.	75
Figure 5.11: FROC curves of the proposed methods in comparison with Candidate Detection and Math Morph using 30 test images from ROC.	76
Figure 5.12: FROC curves of the proposed methods in comparison with Candidate Detection using DIARETDB1 test images.	78
Figure 5.13: ROC training FROC curves of CDL with SRC comparing the use of various λ_1 and λ_2 values.	79
Figure 5.14: DIARETDB1 FROC curves of CDL with SRC evaluating the use of various λ_1 and λ_2 values.	80
Figure 5.15: FROC curves comparing different λ (5.5) values.	81
Figure 6.1: Comparison of Caucasian retina (a) to Asian (b). Disc area, cup volume, maximal cup depth, and vertical cup-disc ratio are larger in (b) compared to (a).	83
Figure 6.2: Thick (a) and (b); thin (c) and (d) vessel cross-sections. The solid line is Asian while the dotted comes from Caucasian, taken from two individuals.	84
Figure 6.3: (a), (c), and (e) Normal fundus image from HIT. (b), (d), and (f) fundus diagnosed with moderate NPDR from HIT.	85
Figure 6.4: Gaussian filter design at three different scales and eight directions.	88

Figure 6.5: Multi-scale filters and scale production: s is the original signal; f is the noisy measurement of s ; R_1 , R_2 and R_3 are the filter responses to f at different scales; Max is the maximum values among R_1 , R_2 and R_3 ; $P_{1,3}$ is the scale production of R_1 and R_2 , and $P_{2,3}$ is the scale production of R_2 and R_3 89

Figure 6.6: Steps of the proposed method applied to a fundus image (a). (b) is the scale production of (a). The result of double thresholding on (b) is (c). The thinned vessels of (c) is (d). (e) is the OD vessel candidates after removing pixels with low intensities. The detected OD center is illustrated in (f) by a cross..... 93

Figure 6.7: Results of the proposed method where a white cross represents the detected OD center.. 94

Figure 6.8: A small vessel map is covered with the 61×21 template (a). Medium to large maps are covered using the 121×41 template (b)..... 95

Figure 6.9: The result of average distance compared with various scale factors applied to the templates. From right to left, the first point is +1.5, next is the current template size, and the left point is -1.5. 96

Figure 6.10: Visual comparison of the OD detection results (proposed method with others). 97

List of Tables

Table 3.1: Vessel extraction results on the STARE database.	34
Table 3.2: Vessel extraction results on the STARE database (normal vs. abnormal cases).	35
Table 3.3: Vessel extraction results for the DRIVE database.	36
Table 3.4: Running time per image on the STARE database.	37
Table 4.1: The list of 31 features.	45
Table 4.2: The discrimination table of different retinal features.	49
Table 4.3: The average number of false positives per image for training data.	53
Table 4.4: The average number of false positives per image for test data.	53
Table 4.5: True microaneurysms with low intensity contrast.	56
Table 4.6: Examples of false positive candidates that resemble true microaneurysms.	57
Table 5.1: Gaussian function with sigma equal to 1.5 compared with two MAs. Using (4.2) the maximum coefficient values of the two MAs are 0.7342 and 0.8132.	62
Table 5.2: ROC training unlearned MA dictionary (\mathbf{A}), dimensions of 121×336	66
Table 5.3: ROC training unlearned non-MA dictionary (\mathbf{B}), dimensions of 121×7796	66
Table 5.4: DIARETDB1 unlearned MA dictionary (\mathbf{A}), dimensions of 121×284	68
Table 5.5: DIARETDB1 unlearned MA dictionary (\mathbf{B}), dimensions of 121×16739	68
Table 5.6: ROC training learned MA dictionary (Φ), dimensions 121×20	69
Table 5.7: ROC training learned non-MA dictionary (Ψ), dimensions 121×20	69
Table 5.8: DIARETDB1 learned MA dictionary (Φ), dimensions 121×20	70
Table 5.9: DIARETDB1 learned non-MA dictionary (Ψ), dimensions 121×20	70
Table 5.10: MA and non-MA representation coefficients from Fig. 5.6 compared with its corresponding class mean coefficients.	73
Table 5.11: MA and non-MA representation coefficients from Fig. 5.7 compared with its corresponding class mean coefficients.	75

Table 5.12: Average sensitivity of different algorithms at various false positive points for the 30 ROC test dataset.....	77
Table 5.13: Average sensitivity of different algorithms at various false positive points for the DIARETDB1 test dataset.....	77
Table 6.1: A vessels' directional matched filter designed for HIT.	90
Table 6.2: OD detection result on HIT using 80 pixels as standard.....	91
Table 6.3: OD detection result on HIT using 60 pixels as standard.....	92
Table 6.4: Average distance (in pixels) of detected and actual OD.	92

List of Abbreviations

FA	Fluorescein Angiograms
TVEP	Transient Visual Evoked Potential
OD	Optic Disc
DR	Diabetic Retinopathy
WHO	World Health Organization
NPDR	Non-Proliferative Diabetic Retinopathy
PDR	Proliferative Diabetic Retinopathy
MA	Microaneurysm
NVD	Neovascularization of the Disc
MF	Matched Filter
FDOG	First-order Derivative of Gaussian
MSCF	Multi-scale Correlation Filtering
SRC	Sparse Representation Classifier
DL	Dictionary Learning
CDL	Centralized Dictionary Learning
VDMF	Vessels' Directional Matched Filter
NN	Neural Network
STARE	Structured Analysis of the Retina
DRIVE	Digital Retinal Images for Vessel Extraction
FOV	Field of View
TPR	True Positive Rate
FPR	False Positive Rate
ROC	Retinopathy On-line Challenge
FROC	Free-response Receiver Operating Characteristic
DIARETDB1	Standard Diabetic Retinopathy Database
HIT	Harbin Institute of Technology

Chapter 1

Introduction

1.1 The Human Eye: Rich Source of Information

The eye is an important organ that provides the magic of sight. It allows us to observe, react and adapt to surrounding environments by interpreting shapes, colors and dimensions of objects seen. This is accomplished when the lens of the eye focuses light onto the photoreceptive cells of the retina. The photons of light trigger a response by producing neural impulses which are processed by different parts of the brain. The anatomy of the eye seen in Fig. 1.1 can be divided into three different layers [1] – external, intermediate and internal. The external layer consists of the sclera and cornea. The intermediate layer is split into two parts: iris and ciliary body. The internal layer is the retina.

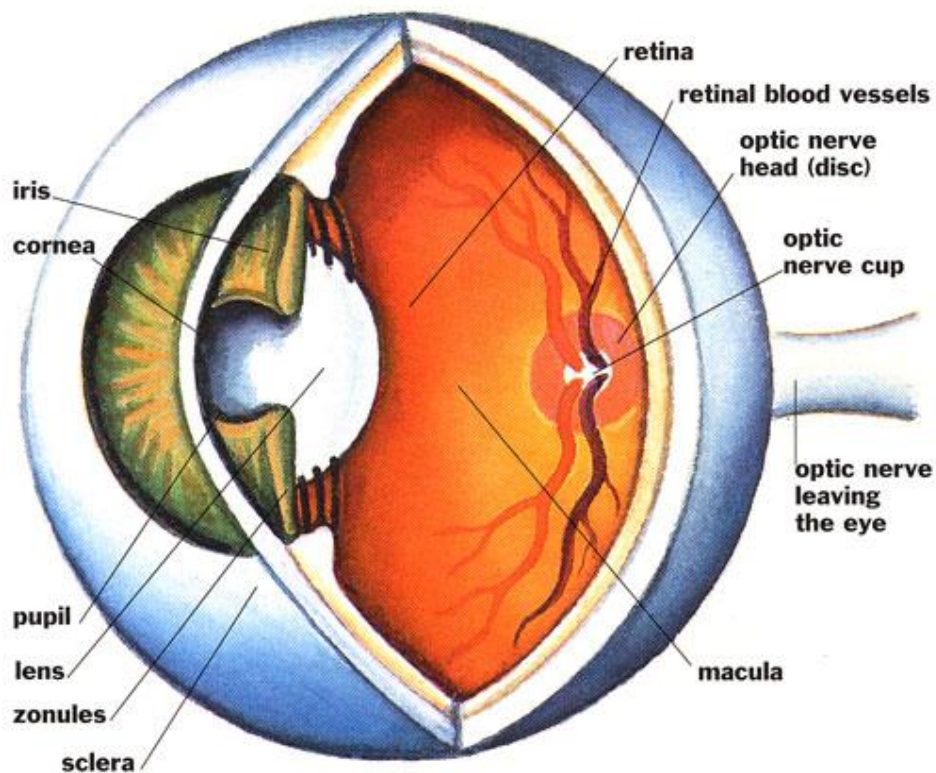


Figure 1.1: Anatomy of the eye [2].

A description of the components in each layer is provided below [1]:

Sclera – the tough white tissue that serves as the eye’s protective outer coat.

Cornea – the transparent front part of the eye that covers the iris and pupil.

Iris – the annular region between the pupil and white sclera.

Ciliary body – a ring of tissue that surrounds the lens.

Retina – a multilayered light sensitive membrane lining the inner eyeball and is connected by the optic nerve to the brain.

The eyes contain a vast amount of information. For example, in order to conceal the identity of an individual, simply covering their eyes will suffice. Fig. 1.2 illustrates this. As can be seen, the identity of this individual is concealed in Fig. 1.2 (b) by covering their eyes. A person’s eyes can reveal how they are feeling, or what they are thinking. The eyes also communicate more data than a person even consciously wishes to express. Pupil dilation for example is a significant cue to a level of excitement, attraction, or pleasure, while constricted pupils send the opposite signal.



Figure 1.2: Concealing the identity of an individual (a) can be accomplished by covering their eyes (b).

The shape of the eyeball has aided the study of astigmatism [3] and can be used in classifying normal, myopic and hyperopic eyes. In [3] through experimentation, the left and right side curvatures, eccentricity, and above curvature (of the eyeball) have been identified as the most discriminative features linked to astigmatism. Iris is primarily used for personal identification and can be found in biometric security systems [4], [5], [6], [7], [8], [9], [10]. Another use of iris is in medical

applications for detecting alimentary canal disease [11] and nerve system disease [11]. Retina can be applied in the same two areas, and a recent review by [12] has shown its analysis to accurately indicate problems in other parts of the circulatory system, the heart [13], the brain, the kidney and ailment within the eye itself. In this thesis we concentrate on the retina.

Fig. 1.3 shows the system architecture of a generic retinal image analysis system, which consists of five components, 1) Sensors, 2) Extractors, 3) Classifiers, 4) Threshold and 5) Decision. After the retina is captured, it is processed to facilitate feature extraction. Once the features are mined a feature vector can be built and used for classification by a classifier. The result of classification will be some matching score. A threshold can then be subsequently applied to this score in order to arrive at a decision of match or non-match.

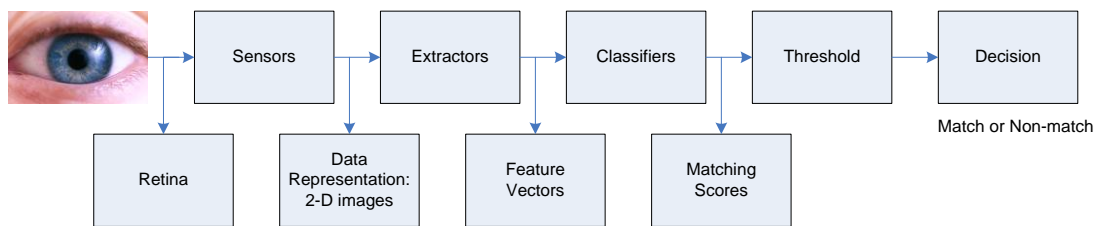
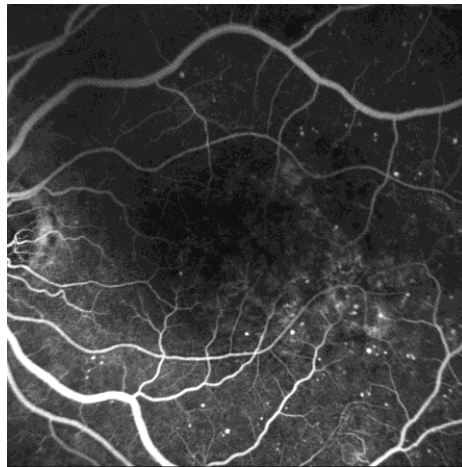


Figure 1.3: Architecture of a generic retinal image analysis system.

1.2 Retinal Image Capture

The retina can be observed and recorded using several methods including Fluorescein Angiograms (FA) [14], [15], [16], [17], [18], Transient Visual Evoked Potential (TVEP) [19] or fundus camera [20], [21], [22], [23], [24], [25], [26], [27], [28], [29], [30], [31], [32], [33], [34], [35]. FA is a medical estimation tool that injects fluorescein into the body before image capture so vessel features (arteries, capillaries and veins) can stand out and be photographed. Although FA produces very clear gray-scale retinal images as seen in Fig. 1.4 (a), it is not well-accepted by patients because of its intrusive nature. TVEP applied by [19], measures an electrical response produced when the retina is stimulated. The procedure for generating a TVEP signal is complicated and time-consuming which makes it unpopular. Therefore, it is essential to develop a safe, fast, easy, and comfortable way to observe and capture the retina. The analysis of color retinal images seen in Fig. 1.4 (b) (aka fundus image, produced by a fundus camera displayed in Fig. 1.5) is viewed as this feasible approach

because the acquisition of color retinal images is non-intrusive, very fast and easy. A fundus camera is essentially a specialized microscope with an attached camera that allows you take photographs of the interior surface of the eye. Processing of color retinal images taken with a fundus camera is usually conducted in its green channel (I_{green}) since vessels and vessel like structures have the highest contrast with its background, evident in Fig. 1.6 (b).



(a)



(b)

Figure 1.4: Most common diabetic retinopathy screening techniques (a) FA and (b) color retinal image.

1.3 Features Extracted from Retinal Images

To analyze retinal images described above and extract information, features need to be mined. These features include blood vessels, microaneurysms and the optic disc.



Figure 1.5: Canon fundus camera [36].

1.3.1 Blood Vessel Features

Lines are composed of edges. Awcock and Thomas defined an edge in a digitized image as a sequence of connected edge points where an edge is characterized by abrupt changes in intensity indicating the boundary between two regions in an image [37], [38], [39], [40], [41], [42], [43], [44], [45], [46], [47], [48], [49]. Based on this, a line according to their definition is a region of constant intensity found between two edges which act as a boundary for the line. Blood vessels in the retina match the criteria of a line. Fig. 1.7 shows two examples of blood vessels. Throughout the retina the major blood vessels supply the capillaries that run into the neural tissue. Capillaries are found running through all parts of the retina from the nerve fiber layer to the outer layer [40], [41], [42], [45], [46], [47], [48], [49]. There are two sources of blood supply to the mammalian retina: the central retinal artery and the choroidal blood vessels. The choroid receives the greatest blood flow (65%-85%) [39] and is vital for the maintenance of the outer retina (particularly the photoreceptors) and the remaining 20%-30% flows to the retina through the central retinal artery from the optic nerve head to nourish the inner retinal layers [41], [42].

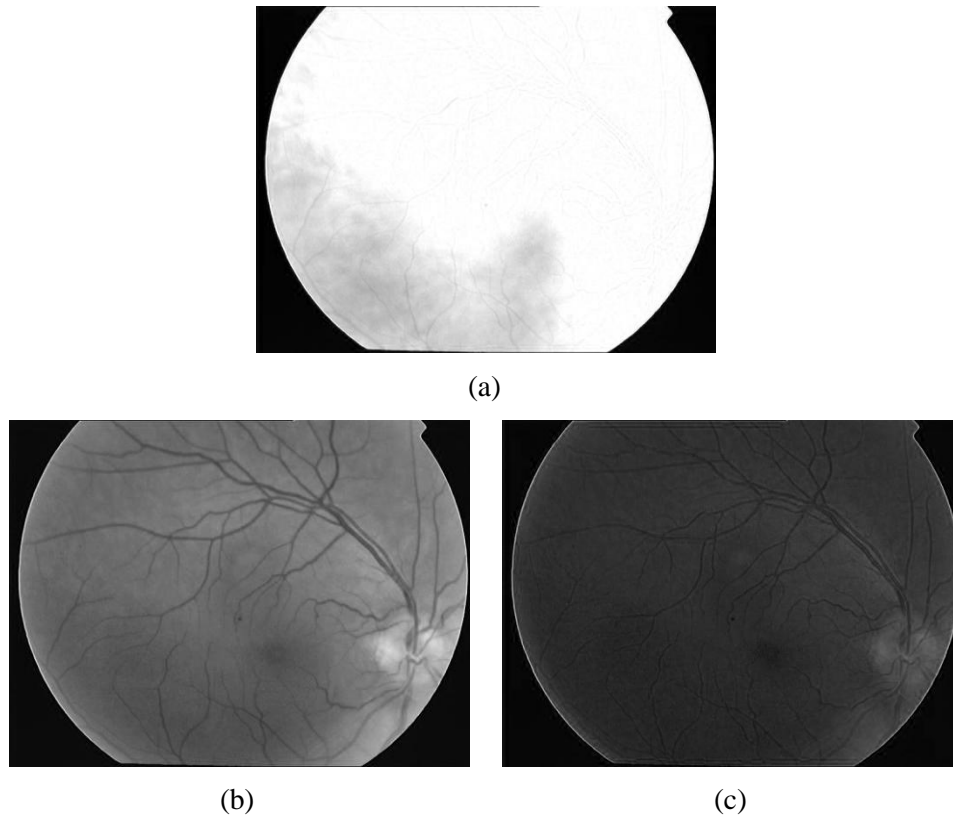


Figure 1.6: The corresponding color bands red (a), green (b) and blue (c) of the color retinal image (Fig. 1.4 (b)).

1.3.2 Microaneurysm Features

Microaneurysms are the dilation of retinal capillaries [50], [51], [52], [53], [54], [55], [56], [57], [58]. They are round intra-retinal lesions ranging from 10 to 100 micrometers in size and red in color [59], [60], [61], [62], [63], [64]. The cross-section of a microaneurysm exhibits a Gaussian distribution. Fig. 1.8 illustrates examples of different microaneurysms taken from color retinal images. The top part shows their original format while the bottom depicts them in the green channel (so their shape is more visible). Researchers at the European Association for the Study of Diabetes 45th Annual Meeting in Vienna, Austria, reported that an increase in the number of retinal microaneurysms is associated with worse retinopathy prognosis in patients with Type 1 or 2 diabetes.

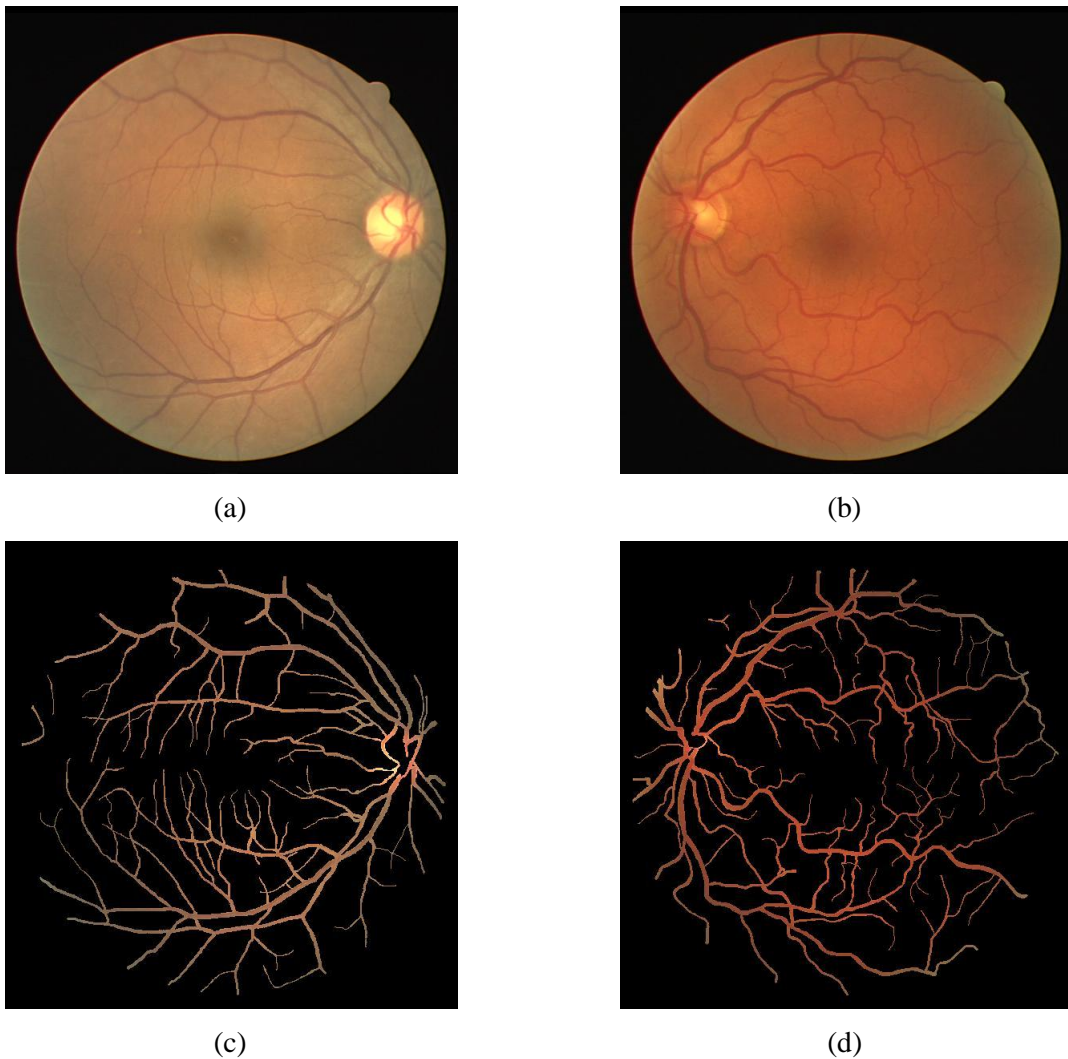


Figure 1.7: Two fundus images (a), (b) and its corresponding vessel map (c), (d).

1.3.3 Optic Disc Feature

The optic disc (OD) or optic nerve head, another commonly used name, is a vertical oval with average dimensions of 1.76mm (horizontally) \times 1.92mm (vertically), and situated 3-4mm to the nasal side of the fovea [1], [65], [66], [67], [68], [69], [70], [71], [72], [73], [74]. There are no receptors in this part of the retina since all of the axons of the ganglion cells exit the retina to form the optic nerve. In fundus imaging the OD is usually brighter than its surrounding area, and is the convergence of the retinal blood vessel network. This can be seen in Fig. 1.9 which shows four different ODs.

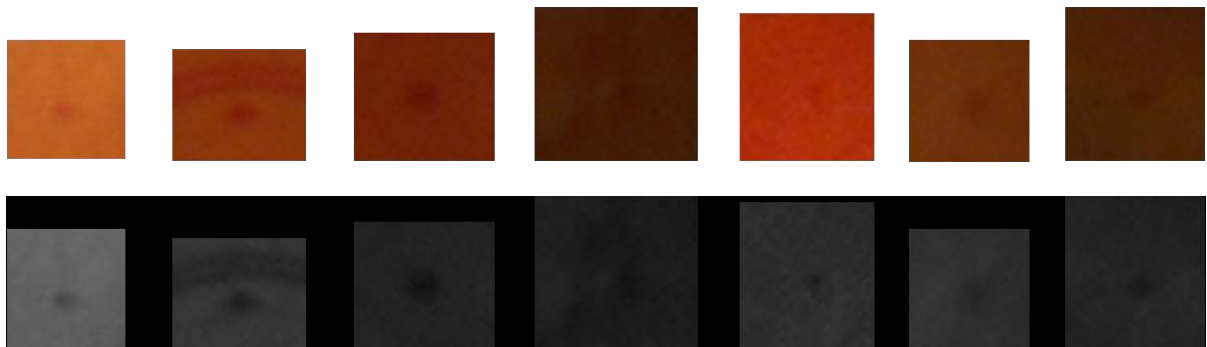


Figure 1.8: Examples of different microaneurysms shown on the top with its equivalent green channel on the bottom.

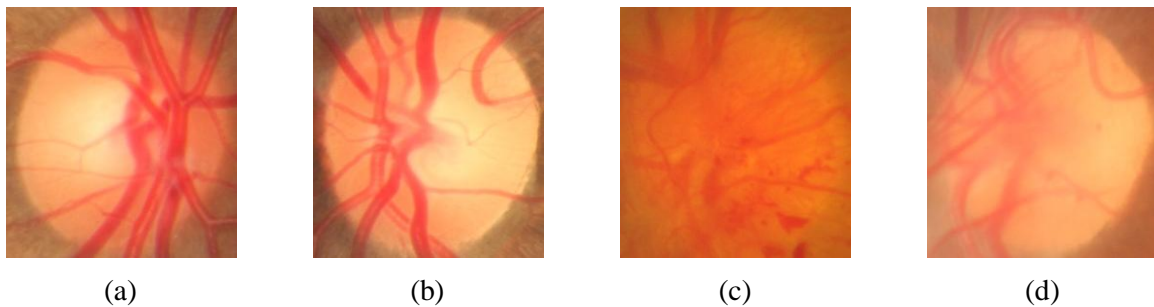


Figure 1.9: Four cropped images of the optic disc.

1.4 Applications Spawned from Retinal Image Analysis

Two major applications can be spawned from retinal image analysis. They are biometrics security and medicine. In this thesis we focus on the latter, primarily the case study of detecting diabetic retinopathy (DR).

Because of the complex structure of the capillaries that supply the retina with blood, each person's retina is unique. The network of blood vessels in the retina is so complex that even identical twins do not share a similar pattern. Although retinal patterns may be altered in cases of diabetes, glaucoma or retinal degenerative disorders, the retina typically remains unchanged from birth until death. Due to its unique and unchanging nature, the retina appears to be the most precise and reliable biometric [75], [76], [77], [78], [79]. Therefore, security-wise, retina [75], [76], [77], [78], [79], [80] has been used at the FBI, CIA, and NASA government agencies as a biometric security system for

identification/verification purposes. These systems are hard to deceive due to the nature of the retina being an internal organ and any modification (to the retina) requires permanent sight loss.

World Health Organization (WHO) has estimated that in 2000 there were 171 million people worldwide with diabetes and this number will increase to 366 million by 2030 [81], [82]. This makes diabetes among the leading causes of disabilities, death and economic hardship in the world. DR is a microvascular complication of diabetes that changes the blood vessels of the retina and is also responsible for 4.8% of the 37 million cases of blindness in the world, estimated by WHO [81], [82]. Blood vessels may swell and leak fluid in some people with DR, while in other people, abnormal new blood vessels grow on the surface of the retina. DR can be found in 80% of all patients who have had 10 or more years of diabetes [83], [84] and between 40%-45% of Americans diagnosed with diabetes are in some stage of DR [84], [85]. Financial expenses to treat or control DR are expected to increase as the number of patients' rise [86], [87]. Fig. 1.10 (a) illustrates what a person with normal vision will see, while (b) shows the same vision with DR.

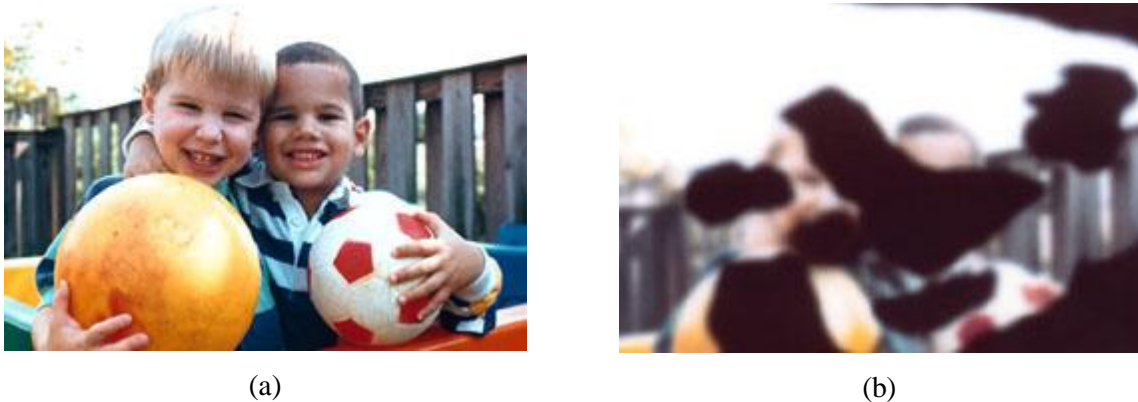


Figure 1.10: What a person with normal vision (a) will see. Same scene viewed by a person with diabetic retinopathy (b) [85].

In general, DR can be classified into four stages [85], [88]: mild Non-Proliferative Diabetic Retinopathy (NPDR), moderate NPDR, severe NPDR, and Proliferative Diabetic Retinopathy (PDR). Below, each stage is explained in more detail [85], [88] with an accompanying retinal image showing typical pathologies at this stage (Fig. 1.11):

- Mild Non-Proliferative Retinopathy – At this earliest stage, microaneurysms occur. They are small areas of balloon-like swelling in the retina’s tiny blood vessels.
- Moderate Non-Proliferative Retinopathy – As the disease progresses, some blood vessels that nourish the retina are blocked.
- Severe Non-Proliferative Retinopathy – Many more blood vessels are blocked, depriving several areas of the retina with their blood supply. These areas of the retina send signals to the body to grow new blood vessels for nourishment.
- Proliferative Retinopathy – At this advanced stage, the signals sent by the retina for nourishment trigger the growth of new blood vessels. This condition is called proliferative retinopathy. These new blood vessels are abnormal and fragile. They grow along the retina and along the surface of the clear vitreous gel that fills the inside of the eye. By themselves these blood vessels do not cause symptoms or vision loss. However, they have thin fragile walls. If they leak blood severe vision loss and even blindness can result.

What makes the retina suitable for DR detection is the fact that DR affects the smallest vessels in the body, and only inspection of the retina allows us to observe this disease. The earliest sign of mild NPDR and for that matter DR is the presence of microaneurysm (MA). By investigating a retinal blood vessel’s width, color, reflectivity, tortuosity and abnormal branching, through the extraction of its vessels, one can diagnose DR [14], [15], [16], [17], [19], [20], [21], [22], [23], [24], [33], hypertension [89], glaucoma [90] and obesity [91]. Detection of the OD is useful in the diagnosis of glaucoma [92], [93], [94], optic neuropathies [95], optic neuritis [96], anterior ischemic optic neuropathy [97] or papilledema [98] and optic disc drusen [99]. It can also be used as a marker to help locate fovea/macula [100], [101], [102], as well as decide if the image is of the left or right eye. For DR, detection of the OD assists physicians identifying neovascularization of the disc (NVD) in the advanced stage of DR, proliferative diabetic retinopathy.

The damage caused by DR can be reduced and major vision loss [103], [104] prevented if it is diagnosed and treated in its early stages. Thus, regular examination of diabetic patients’ retina is very important. During the first three stages of DR [85], [86] no treatment is needed. To prevent progression of diabetic retinopathy, people with diabetes should control their levels of blood sugar, blood pressure, and blood cholesterol. Proliferative retinopathy is treated with laser surgery [85], [86]. This procedure is known as scatter laser treatment and helps to shrink the abnormal blood vessels.

The doctor places 1,000 to 2,000 laser burns in areas of the retina away from the macula, causing the abnormal blood vessels to shrink. Although scatter laser achieves high success rates, it unfortunately does not cure diabetic retinopathy. Once a patient has proliferative retinopathy, s/he will always be at risk for new bleeding.

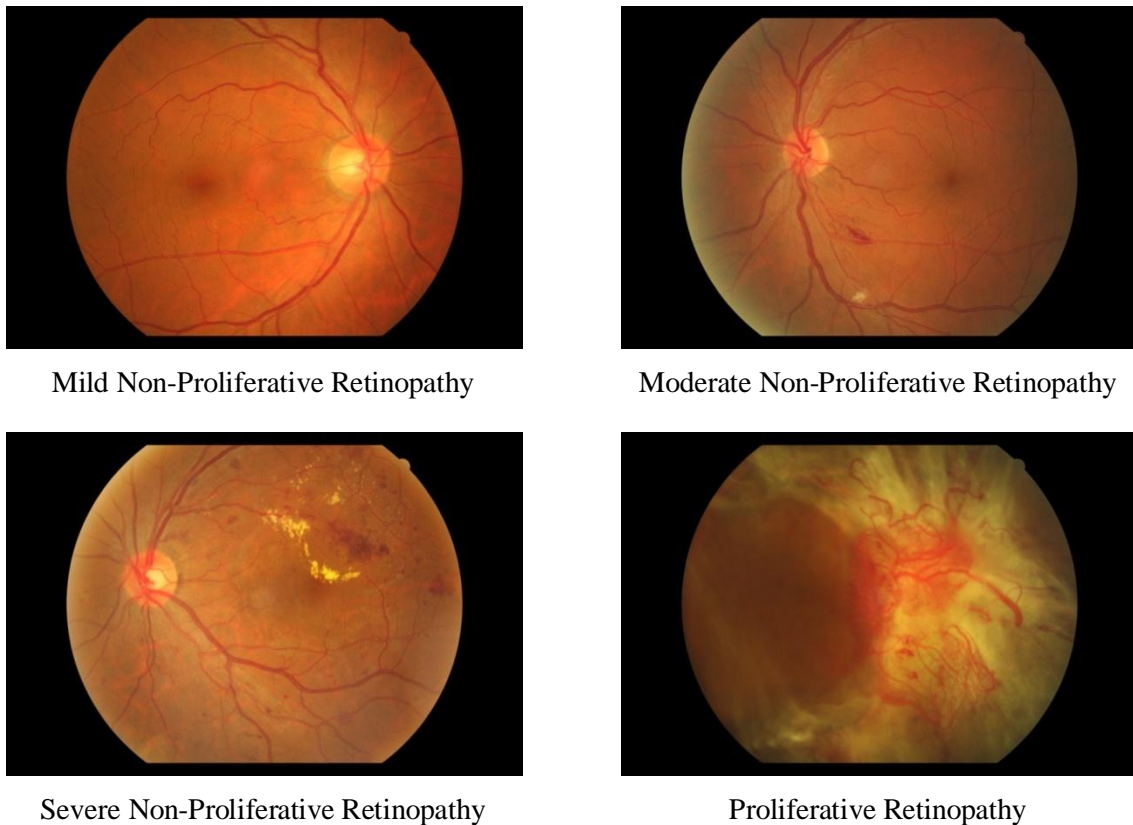


Figure 1.11: Retinal images to show the different stages of diabetic retinopathy.

1.5 Organization

The organization of this thesis is displayed in Fig. 1.12 with a brief description of each chapter provided below.

Chapter 2 is a literature review of current vessel extraction, microaneurysm and OD detection methods. Vessel extraction methods can be grouped into filter-based, mathematical morphology, geometry-based and machine learning (supervised). Microaneurysm detection algorithms include

pixel-based, mathematical morphology, the combination of the two, template-based and supervised learning. OD detection is categorized into template-based, supervised learning, property-based, transform-based and vessel model-based.

We propose a novel extension of the Matched Filter (MF) approach, namely the MF-FDOG [105] in Chapter 3, to extract retinal blood vessels and suppress noise. The proposed MF-FDOG is composed of the original MF, which is a zero-mean Gaussian function, and the first-order derivative of Gaussian (FDOG). The vessels are detected by thresholding the retinal image's response to the MF, while the threshold is adjusted by the image's response to the FDOG.

In Chapter 4 we present an innovative approach that applies a hierarchical methodology to the detection of microaneurysm in color retinal images [106], [107], [108]. The approach makes use of Multi-scale Correlation Filtering (MSCF) with dynamic thresholding and has a two level hierarchical architecture. In Microaneurysm Candidate Detection (coarse level), we detect all possible candidates using MSCF. In the True Microaneurysm Classification (fine level), we classify coarse level candidates using 31 features.

A new approach to detect microaneurysm via Dictionary Learning with Sparse Representation Classifier (SRC) [109], [110] is presented Chapter 5. First, all MA candidates are located by MSCF and then classified with SRC. Particularly, two sub-dictionaries, one for MA and one for non-MA, are learnt from example MA and non-MA structures. This detection result is further improved using another form of Dictionary Learning (DL) known as Centralized Dictionary Learning (CDL) [111]. CDL requires the sparse coding coefficients of the training samples over each learnt sub-dictionary to have a minimal variance. Thereby, allowing the representation of the training samples from the same class to be made as close as possible to its class center. Subsequently when classifying MA, both the reconstruction error and the coding coefficients distance to its class center (from CDL) are used.

In Chapter 6 we propose a method to automatically detect the OD of Asians [112], [113], [114] which is larger than Caucasians using OD vessels. This method consists of two steps: OD Vessel Candidate Detection and OD Vessel Candidate Matching. The first step is achieved with Multi-scale Gaussian Filtering, scale production, and double thresholding to initially extract the vessels' directional map (candidates) of various thicknesses. In the second step, a Vessels' Directional Matched Filter (VDMF) of various dimensions is applied to the candidates to be matched, and the pixel with the smallest difference designated the OD center.

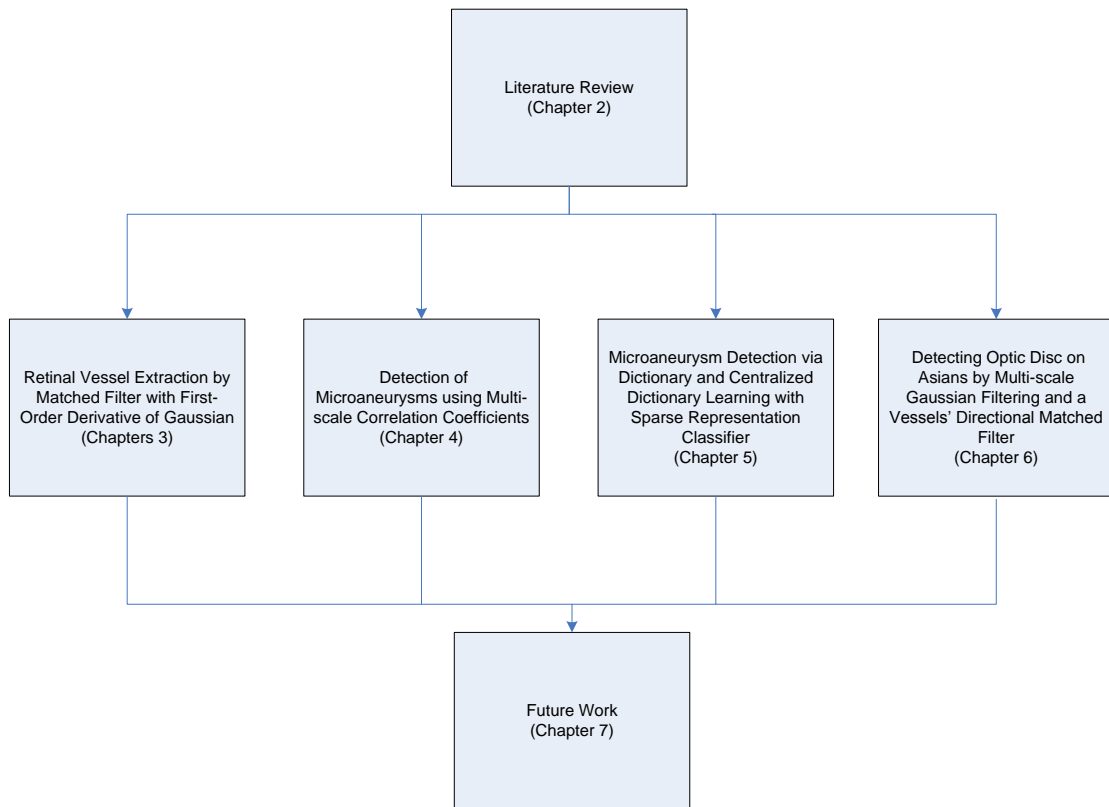


Figure 1.12: The organizational structure of this document.

We conclude with Chapter 7 which discusses future work in the area of improving existing methods, extracting additional features from the retina, developing a generalized automatic OD detection method, and providing a list of publications produced by this research.

Chapter 2

Literature Review

This chapter is a literature review of current and well known methods to extract the vascular map and detect both microaneurysms and the optic disc. Blood vessel extraction methods are given in Section 2.1 followed by microaneurysm and optic disc detection algorithms in Section 2.2 and 2.3 respectively. An assessment of the literary work is provided in Section 2.4 which indentifies their flaws and shortcomings. We conclude with a summary in Section 2.5.

2.1 Blood Vessel Extraction

Vessel extraction in retinal images can be broken down into many groups. They are edge detection, filter-based, mathematical morphology, geometry-based and machine learning (supervised). Each one is explained in more detail below. A list of these methods (except edge detection and supervised learning) tested on STARE [29] and DRIVE [25] databases are located in Section 3.4.

2.1.1 Edge Detection

Blood vessels appear in retinal images as edges and locating them is primarily an edge detection problem. Traditional edge detection methods such as Sobel, Prewitt, Roberts, Laplacian of Gaussian and Canny cannot be applied since noise in the image degrades the result. Even though Canny is regarded by many as an optimal detector because it addressed the issues and shortcomings of other edge detectors at the time, it still fails at vessel detection. Another issue with these methods is that other objects along with edges such as the optic disc and lesions are also picked up. Fig. 2.1 illustrates the result of using edge detectors mentioned above at vessel detection. Additionally, the traditional methods can be classified as general edge detectors and do not consider the unique properties of blood vessels (two edges of a vessel always run parallel to each other).

2.1.2 Filter-based

A popular approach to vessel extraction is filter-based methods [26], [29], [34]. Here, various filters such as Gaussian [29], [34] or Gabor [26] are designed to match and maximize the response to vessel-like structures. The responses are then combined and either a global or adaptive threshold is used to remove noise and extract the vessels. [34] first introduced a method based on the optical and spatial properties of vessels. Specifically the gray level profile of a vessel cross-section is approximated by a

Gaussian shaped curve. The Matched Filter was therefore conceived for the detection of piece-wise linear segments of blood vessels with twelve different templates constructed to search for vessel segments along all possible directions. [29] improved upon [34] by applying piece-wise threshold probing. The blood vessel network is segmented by iteratively probing an area of the Matched Filter response. At each iteration region based features of the piece are tested to determine the probe's continuation, which ultimately decides if the piece is a vessel. The advantage of this approach allows both local and regional features to be used. 2-D Gabor wavelet and supervised classification was used in [26]. This method classified each image pixel as vessel or non-vessel based on the pixel's feature vector. The feature vectors are composed of the pixel's intensity as well as its responses to 2-D Gabor wavelet transform with multiple scales. Using the Gabor wavelet allows for tuning to specific frequencies where noise filtering and vessel enhancement can be achieved in a single step. For classification the Bayesian classifier with Gaussian mixture models was used.

2.1.3 Mathematical Morphology

Mathematical morphology [31], [115] is another approach applying morphological operators such as opening and closing. These operators are built using dilation and erosion. The idea of mathematical morphology is to repeatedly reduce and enlarge objects which will eliminate noise and smaller details by shrinking them while retaining larger objects. [31] designed a way to combine mathematical morphology with center-line detection to extract vessels. Their method consisted of three phases. In the preprocessing phase, the background was removed from the image and thin vessels were enhanced. In the next phase, vessel center-line detection, candidates of the center-line were detected and connected. Finally, in the last phase morphological operations and region growing reconstructed the complete vessel using results of the previous phase. Mathematical morphology and curvature evaluation was used by [115] to detect vessels. They defined a vessel as a bright pattern, piece-wise connected and locally linear. With this definition mathematical morphology was well suited. However, to deal with cases where other patterns fit such a morphological description, a cross-curvature evaluation was performed. This was based on a vessel having a Gaussian like profile where its curvature varies smoothly along the vessel.

2.1.4 Geometry-based

These methods use geometric features such as shapes and measurements to help extract vessels. This can be accomplished by calculating the vessel's curvature [115], [116], center-line [31] or tracing the

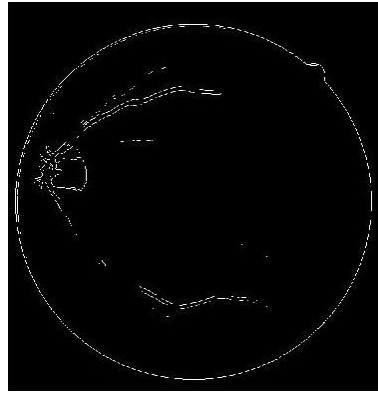
vessel's movement. Ridge detection [25] is one well known example based on the observation that the vessels can be modeled as ridges, where for each pixel a gradient is determined based on the intensity of that pixel and its surrounding pixels. The direction of the maximum curvature can be calculated along a line covering several pixels and the peak of the ridge is a point at which the gradient is zero. Once the ridges have been identified, further processing is done to link ridges and classify pixels based on their gradients as well as neighboring vessel pixels. When visualizing a 3-D color retinal image in its green channel, the blood vessels form topographical trenches. Therefore, the problem of vessel detection becomes trench detection. [116] presented an unsupervised curvature based method where the vessels are modeled as trenches using curvature measurements based on medial lines. Medial lines of trenches are characterized by high magnitudes of curvature along the direction perpendicular to the trench.

2.1.5 Machine Learning: Supervised

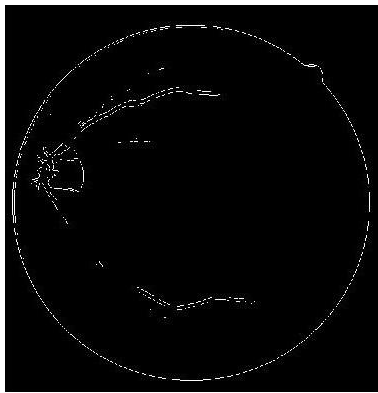
Methods in this group involve classification. Neural network (NN) [33], [35] and k -NN [25] are the most common classifiers in training vessel recognition. In NN, a single pixel or a block of pixels can be fed as input in order to determine if it is a vessel. For k -NN, a feature vector is constructed for an object involving feature extraction to determine if the object is also a vessel. Both classifiers require a test set to assess the learnt knowledge. In [33], NN was used to automatically classify blood vessels. The NN consisted of an input pixel layer, hidden layer and output layer, and was trained to recognize features such as blood vessels, exudates and hemorrhages. Each image was divided into 30×30 and 20×20 squares pixels depending on the feature being detected and a trained observer then classified the squares as normal retina not showing blood vessels (normal), normal retina showing normal blood vessels (vessel), retina showing exudates (exudates), or retina showing hemorrhages or microaneurysms (hemorrhage). Detection rate for recognition of vessels was 91.7%. Once the ridges in [25] were extracted and used to form the line elements, a feature vector was built for each pixel. This vector consisted of the properties of the patches and the line elements. The feature vector was classified using k -NN and sequential forward feature selection.

2.2 Microaneurysm Detection

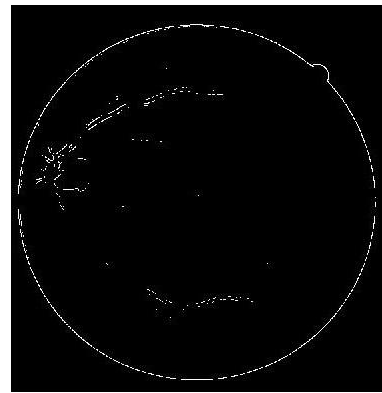
Microaneurysms can be detected by pixel classification, mathematical morphology, the fusion of the two, template-based and supervised learning. A description of each is provided below.



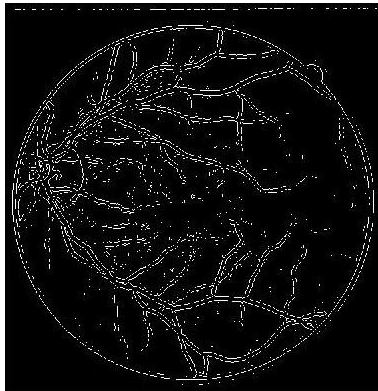
(a)



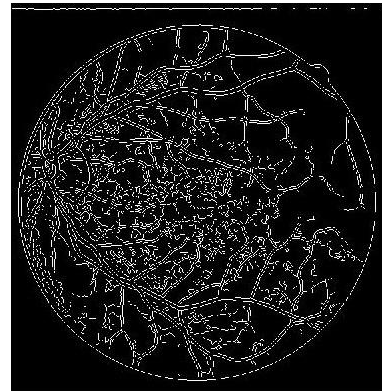
(b)



(c)



(d)



(e)

Figure 2.1: Using traditional edge detection methods to enhance retinal blood vessels Sobel (a), Prewitt (b), Roberts (c), Laplacian of Gaussian (d) and Canny (e).

2.2.1 Pixel Classification

[24] developed a method to detect microaneurysms by integrating a vessel segmentation technique. Both the vessel map and possible microaneurysms are extracted at once, with the map subsequently separated from the microaneurysm candidate objects. Pixel classification being a supervised method requires the training of examples. All the pixels in the training set were thus assigned a label and a feature vector. After experimenting with different classifiers, they found the k -NN classifier produced the best result. The first step in [108] was to resize the image converted to its green plane so the field of view had a certain width. The image was then normalized by subtracting an estimate of the image background. This background was determined by filtering the image with a large median kernel. Using an unsupervised mixture model based clustering method, the microaneurysm candidates were detected from the normalized image intensities. Each pixel was assigned one of three classes, class 1 background elements; class 2 foreground elements, e.g. vessels, optic disc and lesions; class 3 outliers. A three class Gaussian mixture model was applied to fit the image intensities and a group of microaneurysm candidates were segmented by thresholding the fitted model. The vessel map was extracted and used to remove any candidates that lie on the vasculature. With logistic regression, a likelihood for each of the remaining candidates was calculated based on color, shape and texture properties.

2.2.2 Mathematical Morphology

This algorithm was developed by [17] and improved by [14]. In the image preprocessing stage the image background is removed to create a “shade corrected” image. This is accomplished by subtracting the image with the result of a 25×25 median filter applied to the image. Afterwards, candidate extraction is performed on the “shade corrected” image by extracting vessels with morphological opening using 12 rotated linear structuring elements at 15° and producing 12 responses. Taking the maximum pixel values of all 12 responses at each pixel location produces a vascular map which is subsequently removed from the “shade corrected” image. The remaining candidates inside this image should no longer contain elongated structures but microaneurysms. Region growing is applied to each candidate before 13 features based on shape and color intensities are extracted. This is used to construct a feature vector for classification. [108] is a variant of [17], [14]. After normalization by subtracting a median filtered version of the image, noise was subsequently removed by another median filter with a small kernel. A top hat transform by morphological reconstruction using an elongated structuring element at different orientations was

employed to detect the vasculature. With the vasculature removed, a microaneurysm matched filtering step was applied to locate the position of the candidates by thresholding. Region growing was directed at each of the remaining candidate before a number of features based on color, intensity and shape were extracted. A Bayesian classifier was then used to assign a likelihood of being a true microaneurysm to each of the detected candidates.

2.2.3 Fusion Technology

[24] devised another way to detect microaneurysms in fundus images based on candidate detection and classification. Candidate detection consisted of locating all possible microaneurysms by combining mathematical morphology [14] with pixel classification. The combination was accomplished by placing all candidate objects in a set. Afterwards, all objects were checked to see if they overlap with one another in the set. In case of an overlap, one of the objects is removed. When both candidate detection systems detect the same object it does not matter which object is removed. The pixels were classified using a k -NN classifier with a reference standard that manually marked each image pixel. After the candidates are combined, the procedure extracts 68 features (from each candidate), again using k -NN to classify the candidate as either microaneurysm or non-microaneurysm. This work reported a 100% true positive rate with an 87% true negative rate when deciding if an image had a microaneurysm.

2.2.4 Template-based

Template-based algorithms [55], [108] design templates to match with microaneurysms. The algorithm presented in [55] applied wavelet image decomposition. It compared a small window of the image with a microaneurysm template modeled by a Gaussian curve. The comparative result was the squared errors sum between coefficients of each sub-band and the microaneurysm's corresponding coefficients. Thresholds were used to separate microaneurysms from other structures. [108] based their method on template matching also in the wavelet domain. To perform template matching in the wavelet domain, the wavelet transform of the Gaussian microaneurysm model at several different standard deviations was used. The coefficients of the wavelet transform model were compared to the coefficients of the wavelet transform of the image. Places in the image where a difference below a certain threshold existed, were assigned the microaneurysm locations. The size of the detected microaneurysm was determined by parameters of the matched model. Any candidates on the vasculature were removed based on a vessel segmentation step using wavelet analysis. For each of the

remaining candidates, a likelihood determined by the local difference in wavelet coefficients was assigned.

2.2.5 Supervised Learning

Methods in this group use NN [33], [108], k -NN [24], [56], Bayesian [57] and SVM [139] to distinguish microaneurysm candidates from non-microaneurysm ones. The algorithm [108] initially begins by preprocessing the fundus image to reduce the differences in intensity and contrast. This is accomplished by brightness and gamma correction as well as contrast enhancement. Microaneurysm detection is performed using a modified double ring filter. The double ring filter was originally designed to detect areas in an image where the average pixel intensity is lower than the average pixel intensity in an area surrounding it. [108] modified this filter to detect areas where the average pixel intensity in the surrounding area is lower by a certain fraction of the number of pixels under the filter. This is done to reduce false positive detections on smaller capillaries. A vessel map is next detected using the original double ring filter with different parameter settings to remove any candidates that lie on the vasculature. Afterwards, 12 features are extracted from each of the remaining candidates which had region growing applied to it. The features include shape, intensity, color and contrast features. An artificial neural network was trained and used to separate microaneurysms from non-microaneurysms. Local contrast normalization with local vessel detection was regarded as another useful approach to detect microaneurysms [56]. After the initial preprocessing stage, a watershed retinal region growing method was applied to be used for contrast normalization of each candidate microaneurysm. Local vessel detection detected vessels that occur with microaneurysms and a k -NN classifier was used to classify the candidates. The algorithm presented in [57] can be divided into four steps. The first step consisted of image enhancement: shade correction and image normalization of the green channel. The second step was candidate detection using diameter closing with an automatic threshold scheme. The third step involved feature extraction to facilitate the forth step of classification which was based on kernel density estimation in conjunction with Bayesian risk minimization. [139] employed a two stage process to detect microaneurysms. The approach first used intensity information from red and green channels of the fundus image to correct non-uniform illumination. Matched filters were then applied to enhance the contrast of microaneurysms against the background. The enhanced microaneurysms were segmented by a thresholding scheme which maintains the spatial structure of the microaneurysm segments. The vasculature was then removed from the image and detected via

morphological top hat transform. The remaining candidates after the previous stage were classified using SVM to separate microaneurysms from other dark segments.

2.3 Optic Disc Detection

OD detection is categorized into template-based, supervised learning, property-based, transform-based and vessel model-based. In the following each one will be described.

2.3.1 Template-based

In [117] the authors' applied template matching to locate the OD center. They first used illumination equalization based on Hoover and Goldbaum [29] to smooth the image with a 40×40 running window. Afterwards, Adaptive Histogram Equalization (AHE) is applied to normalize and enhance the contrast within the image. AHE is more effective than the classical histogram equalization especially at detecting small blood vessels with low contrast levels. The retinal blood vessels are next segmented using MFs with one scale and 12 directions based on the result of AHE. Applying the MFs to the AHE image improves the segmentation algorithm and increases the sensitivity and specificity of the detected vessels. The segmented vessels are thinned and the corresponding highest 4% in the illumination equalized image remain as the candidates. Of the remaining vessel candidates four Vessels' Direction Matched Filters are applied to roughly match the direction of the vessels in the OD vicinity. The pixel with the least accumulated difference between its candidates and Vessels' Direction Matched Filters is selected the OD center.

2.3.2 Supervised Learning

Supervised learning is another group consisting of feature extraction and classification with a Bayesian [102] or k -NN [100], [101] classifier. [102] first used [115] to segment the vessels in the retina. Afterwards, they used the binary representation of the segmented vessel map along with a luminance representation to generate four features that help determine the OD. These features include retinal luminance, vessel density, average vessel thickness and average vessel orientation. Using Bayes rule they classified each pixel to locate the OD center. In [100] a template was initially used to approximate the location of the OD. Afterwards, a set of features based on its surrounding vessels including the number of vessels, average width of the vessels, maximum vessel width..., etc were extracted. A single point distribution model was applied to each image in [101] to locate the OD, macula and vascular arch. The correct position of each model point was calculated using global and local features. Global features were the orientation and width of the vessels, while local features were

found from the image structure around the points of the model. To facilitate vessel extraction the vessel map was segmented beforehand using pixel classification [100], [101]. A k -NN classifier was applied to both [100] and [101] after the features were extracted.

2.3.3 Property-based

High pixel intensity and its oval shape are some examples of properties [35], [118], [119], [120] used to detect the OD. In [35] the appearance of the OD was characterized by a relatively rapid variation in intensity due to the blood vessels being beside the nerve fibers. Therefore, the variance of intensity in adjacent pixels to the OD was calculated and used for recognition. [118] first determined the candidate regions by clustering the brightest pixels in an intensity image. Principal Component Analysis was then applied to the candidate regions with the minimum distance between the original retinal image and its projection designated the center of the OD. The authors' of [118] improved their detection method by additionally detecting the shape of the OD using a modified active shape model [119]. Based on the brightness and roundness of the OD, [121] presented a method using algorithms which included repetitive thresholding, detection of object roundness and circle detection. After finding several areas with high intensity variation, the proposed method selected all rounded areas. For each edge of the rounded area the OD contour is estimated with the Hough transform. The Hough transform detects the number of OD candidates outlined by circles and selects the circle which has a higher intensity as the OD.

2.3.4 Transform-based

Two different kinds of transforms, Hough [121], [122], [123], [124] and watershed [125], [126] have also been applied to locate the edges of the OD and subsequently its center. Based on the properties of the OD, both [122] and [124] used Sobel to initially extract the edges in the image. The Hough transform was then applied to detect circles that encompass the area of the OD, with the highest intensity circle assigned the OD. [125] used a threshold to first obtain parts of the OD. With an approximate location a filter was applied to eliminate large gray level variations. Next, the vessels in this area were removed and the contours of the OD were detected using the watershed transform. A combination of the watershed transform and active contours called "watersnake" was proposed in [126]. The first step was initializing the OD boundary using watershed. In the second step, snake is employed to detect the actual boundary of the OD.

2.3.5 Vessel Model-based

Methods in this group [29], [100], [101], [127], rely on the geometrical directional pattern of the retinal vascular system, which implicitly holds information on the OD position as the point of convergence of all vessels. Fuzzy convergence developed by [29] determined the originating vessel map convergence point near the OD center as the focal point of the blood vessels network. The algorithm is a voting type method that works in the spatial domain of the image. The input to the algorithm is a binary segmentation of the blood vessels where each vessel is modeled by a fuzzy segment that contributes to a cumulative voting image. The output from the algorithm is a convergence image that is then thresholded to locate its strongest points. [127] proposed a method that is based on a model of the geometrical directional pattern of the retinal vascular system. This system implicitly holds the information on the OD position as the point of vessel convergence. Using the vessel center-line points and the corresponding vessel directions provided by any vessel identification procedure, the model parameters were identified by a means of simulated annealing. These estimated values provide the coordinates of the OD center.

2.4 Assessment

Even though filter-based methods are simple to implement their results are not ideal as non-vessel objects can be enhanced and the choice of a suitable global threshold value difficult. Mathematical morphology techniques are more complex than filter-based which make them harder to execute and understand. The extracted vessels also suffer from noise due to pathologies in the images and finer vessels such as capillaries are lost. Some geometry-based methods rely on traditional edge detection, mentioned above as unsuitable for vessel extraction. Supervised machine learning methods require feature extraction and depending on the actual method these features can be extracted with little or no ease. As for classification, the classifier needs to be trained and this can be time consuming.

Pixel classification found in [24], [108] involves medical experts labeling each pixel, something not feasible when using a greater number of images. A limitation of mathematical morphology [17], [14], [108] is that when the length of the structuring element is increased to be able to detect larger objects, the vessel segmentation deteriorates leading to more spurious candidate objects being detected on the vessel. The problem with template-based methods is designing suitable templates to match the microaneurysm. This requires studying the microaneurysms in the training dataset beforehand and adjusting parameters to achieve the best detection result. Supervised learning methods

[24], [33], [56], [57], [108], also suffer from the same problems as pixel classification, requiring labeling of each microaneurysm and a long training time.

Template-based methods for OD detection require fine tuning parameters such as the template, to better match the images from the database in question. Selecting suitable training images and the time constraint are issues of supervised learning. Also, in the case of [100], [101], the vessels are segmented via pixel classification, a time consuming process. Using properties of the OD sound simple but in actuality these properties only hold true under ideal imaging conditions. In most cases lighting and other environmental factors contribute to non-ideal situations. Finally, transform and vessel model based methods are computationally complex, their performance is dependent on the model, and they are not flexible to manage abnormal images.

2.5 Summary

This chapter gave a literature review on the current works involving blood vessel extraction, microaneurysm and OD detection. Blood vessel extraction methods can be broken down into the following categories: filter-based, mathematical morphology, geometry-based and supervised learning. For microaneurysm detection there are pixel-based, mathematical morphology, a hybrid algorithm that is the fusion of the previous two, template-based and supervised learning. OD detection is grouped into template-based, supervised learning, property-based, transform-based and vessel model-based. An assessment of each work was given in Section 2.4. Much more is yet to be done in all areas in order to overcome current problems and achieve better results.

In the succeeding chapter a novel vessel extraction method called MF-FDOG that can distinguish between vessel and non-vessel object is proposed. MSCF is discussed in Chapter 4 to locate microaneurysm based on a hierarchical approach of Candidate Detection and True Microaneurysm Classification. In Chapter 5 both Dictionary and Centralized Dictionary Learning with Sparse Representation Classifier are used to detect microaneurysms. A method that describes automatic optic disc detection of Asians is provided in Chapter 6. Improvements to all of the proposed methods are depicted in Chapter 7, including plans for future work.

Chapter 3

Retinal Vessel Extraction by Matched Filter with First-Order Derivative of Gaussian

This chapter presents our proposed method on vessel extraction using Matched Filter (MF) with FDOG. Section 3.1 begins with an introduction on the theory of blood vessel extraction. This is followed by an explanation of the original MF in Section 3.2. Section 3.3 describes the proposed method, MF-FDOG which uses thresholding. Experimental results generated using two publicly available databases STARE and DRIVE are given in Section 3.4. We conclude with a summary in Section 3.5.

3.1 Introduction

In Chapter 1 the importance of retinal blood vessels to medical diagnosis of disease was presented along with a review of vessel extraction algorithms in Chapter 2. Among the various retinal vessel extraction methods, the classical Matched Filter [34] method is a representative one and has advantages of simplicity and effectiveness. The MF detects vessels by simply filtering and thresholding the original image. Considering the fact that the cross-section of a vessel can be modeled as a Gaussian function, a series of Gaussian shaped filters can be used to “match” the vessels for detection. However, the MF will have strong responses to not only vessels but also non-vessel edges, for example, the edges of bright blobs and red lesions in retinal images. Therefore, after thresholding the response image, many false detections can result.

Although the MF employs the prior knowledge that the cross-section of vessels in a retinal image is Gaussian shaped (this can be seen in Fig. 3.1 where the cross-sections of five vessels are plotted), it does not fully exploit other information of the vessel profile, in particular that the Gaussian shaped cross-section is symmetric with respect to its peak position. If this property can be properly used, it is possible to distinguish the symmetric vessel structures from those asymmetrical non-vessel edges (e.g. the step edge) in a simple but efficient way, and hence the vessel extraction accuracy can be improved.

To this end, this chapter proposes a novel method, namely the matched filter with first-order derivative of the Gaussian (MF-FDOG), as an extension and generalization of the MF. Considering that the cross-section of a vessel is a symmetric Gaussian function, we use a pair of filters, the zero-

mean Gaussian filter (i.e. the MF) and the first-order-derivative of Gaussian (FDOG), to detect the vessels. For a true vessel, it will have strong response to MF around its peak position, while the local mean of its response to FDOG will be close to zero around the peak position. In contrast, for non-vessel structures, for example the step edge, it will have high response to MF but the local mean of its response to FDOG will also be high. Such a difference implies that vessels and non-vessel edges can be better distinguished by MF-FDOG than by using the MF.

By applying the MF-FDOG filters to the retinal image, two response maps H (by MF) and D (by FDOG) can be obtained. The vessel map is detected by applying a threshold T to H , while the threshold T is adjusted by D so as to remove the non-vessel edges and extract the fine vessels. As a filtering-based method, the proposed MF-FDOG preserves the simplicity of the original MF; however, it could achieve much higher vessel detection accuracy than the MF, and even comparable to the results of state-of-the-art methods [25], [26], [28], [30], [31], [32], [115], [116], [128], which have much higher complexity than the MF-FDOG.

3.2 The Matched Filter

The Matched Filter was first proposed in [34] to detect vessels in retinal images. It makes use of the prior knowledge that the cross-section of the vessels can be approximated by a Gaussian function. Therefore, a Gaussian-shaped filter can be used to “match” the vessels for detection. The MF is defined as:

$$f(x, y) = \frac{1}{\sqrt{2 \cdot \pi} \cdot s} \exp\left(-\frac{x^2}{2 \cdot s^2}\right) - m, \quad \text{for } |x| \leq t \cdot s, \quad |y| \leq L/2 \quad (3.1)$$

where s represents the scale of the filter:

$$m = \left(\int_{-t \cdot s}^{t \cdot s} \frac{1}{\sqrt{2 \cdot \pi} \cdot s} \exp\left(-\frac{x^2}{2 \cdot s^2}\right) dx \right) / (2 \cdot t \cdot s)$$

is used to normalize the mean value of the filter to 0 so that the smooth background can be removed after filtering, and L is the length of the neighborhood along the y -axis to smooth noise; the criterion t is a constant and is usually set to 3 because more than 99% of the area under the Gaussian curve lies within the range $[-3s, 3s]$. The parameter L is also chosen based on s . When s is small, L is set relatively small, and vice versa. In the implementation, $f(x, y)$ will be rotated to detect the vessels of different orientations.

The simplicity of the MF makes it popular in vessel detection. However, a well-known problem of the approach is that it responds not only to vessels but also to non-vessel edges. Fig. 3.2 (a) and (b)

illustrate this problem by showing the responses of the MF to a Gaussian function (i.e. the cross-section of a vessel) and an ideal step edge. We can see clearly that the MF has strong responses to both the vessel and the step edge. After thresholding, both the vessel and the non-vessel edge will be detected. Therefore, the aim of this method is to find a simple filtering technique to distinguish the vessels from non-vessel step edges.

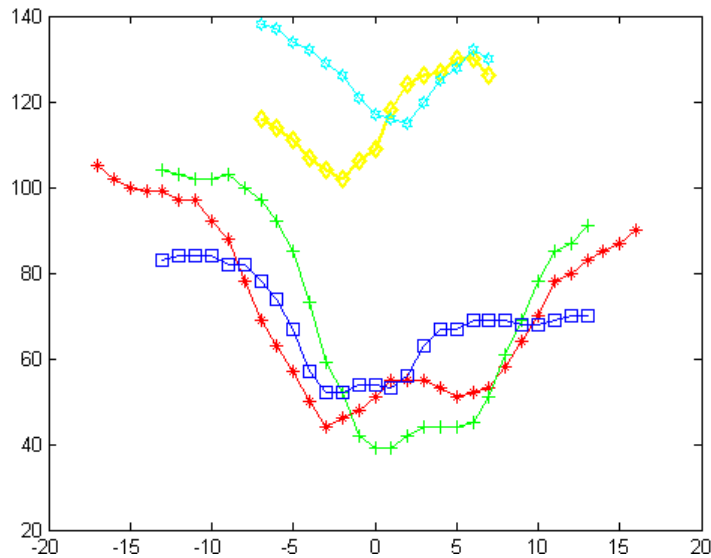


Figure 3.1: Cross-section plot of five different retinal blood vessels. The x -axis is the cross-section width while the y -axis represents pixel intensity.

3.3 The MF-FDOG

As can be seen in Section 3.2, the MF has strong responses to both vessels and step edges because it can “match” the shape of both vessels and step edges to some extent. Thus it is hard to distinguish the two types of structures only by the response of MF. Based on the fact that the vessel cross-section is a symmetric Gaussian function while the step edge is asymmetric, we propose a simple scheme by using a pair of filters, instead of only one filter, to distinguish Gaussian vessel structures from non-vessel edges.

The MF is a zero-mean Gaussian filter and it is defined in (3.1). It can be readily derived that the first-order derivative of the Gaussian (FDOG) is:

$$g(x, y) = -\frac{x}{\sqrt{2 \cdot \pi} \cdot s^3} \exp\left(-\frac{x^2}{2 \cdot s^2}\right) - m, \quad \text{for } |x| \leq t \cdot s, \quad |y| \leq L/2 \quad (3.2)$$

In this chapter, we use the MF and the FDOG as “MF-FDOG” for vessel detection. The idea comes from the fact that the Gaussian function (i.e. the cross-section of a vessel) will have a strong positive response to the MF but its response to the FDOG is anti-symmetric. In contrast, although the non-vessel step edge will have partially strong positive responses to MF, its response to the FDOG is positive and symmetric. Fig. 3.2 shows this by using a synthetic signal. Fig. 3.2 (a) plots a Gaussian function and an ideal step edge; Figs. 3.2 (b-1) and (b-2) show the MF and its response to the synthetic signal; Figs. 3.2 (c-1) and (c-2) show the FDOG and its response. Denote by h the signal’s response to the MF. Suppose that we apply a threshold T to h to detect the vessels. Obviously, some of the step edge’s responses will be wrongly classified as vessels. However, if we could properly exploit their different responses to FDOG, as shown in Fig. 3.2 (c-2), the vessels and non-vessel edges can be better distinguished by thresholding their responses to MF.

Denote by d the response of the input signal to the FDOG. Let us calculate the local mean of d , denoted by d_m . The local mean value of an element in d is defined as the average of its neighboring elements. Fig. 3.2 (d) shows the d_m of the response d in Fig. 3.2 (c-2). We can see that in the peak area of the Gaussian function, there are strong responses in h (refer to Fig. 3.2 (b-2)), while the corresponding responses in d_m (refer to Fig. 3.2 (d)) are very low. In contrast, in the neighborhood of the step edge there are also strong responses in h but the corresponding responses in d_m are very high. Therefore, the local mean signal d_m can be used to adjust the threshold T to detect the true vessels while removing non-vessel edges. In other words, T should depend on d_m . If the magnitude in d_m is low, this implies that a vessel may appear in the neighborhood, and hence the threshold T applied to h can be small to detect the vessels; if the magnitude in d_m is high, this implies that some non-vessel edges may appear, and hence the threshold T can be high to suppress the non-vessel edges.

We propose a thresholding scheme by using the MF-FDOG for retinal vessel detection. The threshold is applied to the retinal image’s response of MF but the threshold level is adjusted by the image’s response to FDOG. After filtering the retinal image with the MF-FDOG filters, two response images H (by the MF) and D (by FDOG) are obtained. In actuality multiple MF-FDOGs along different orientations will be used, but for the convenience of discussion we consider only one MF-FDOG here. The local mean image of D is calculated by filtering D with a mean filter:

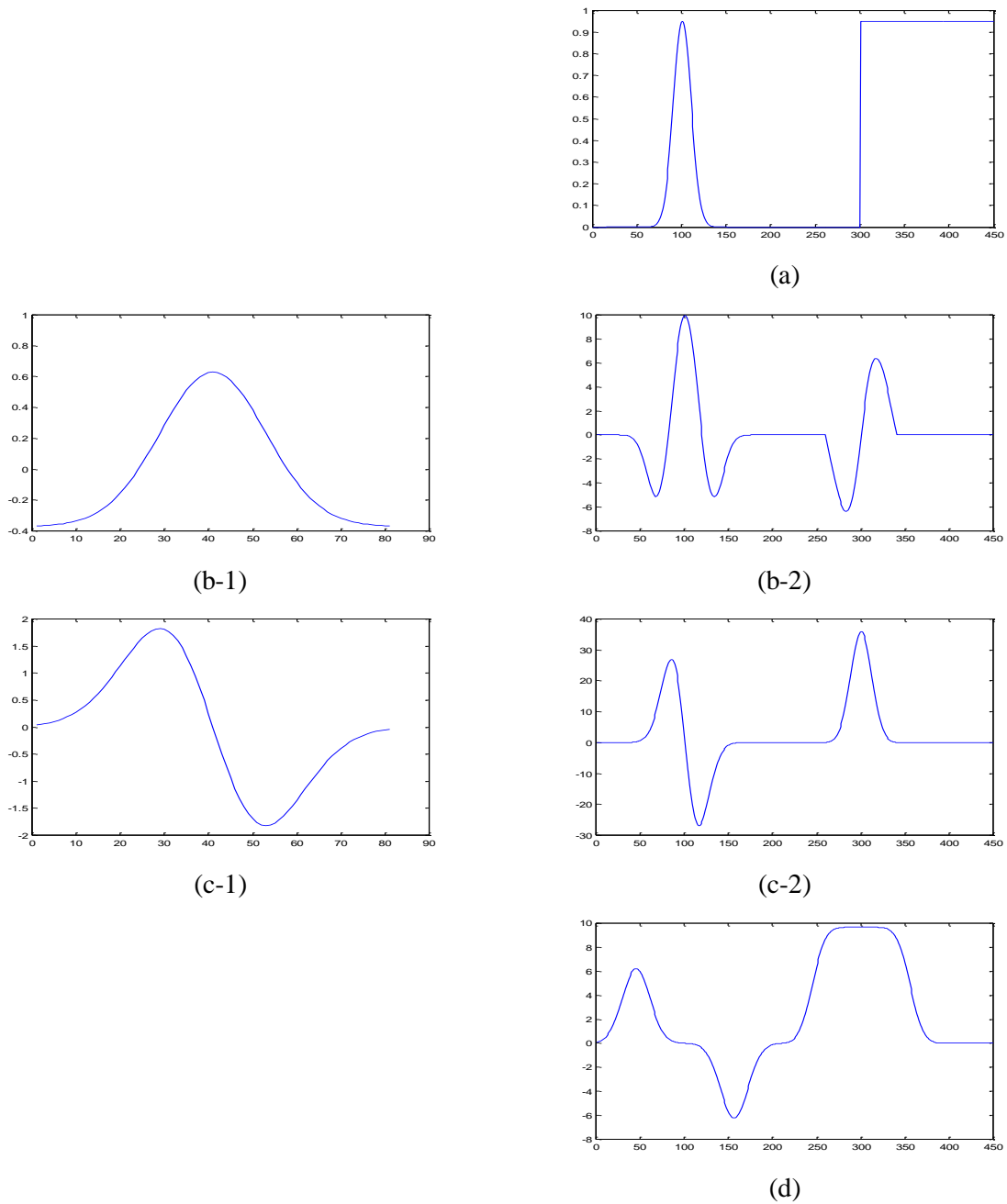


Figure 3.2: Responses of the MF and the FDOG to a Gaussian line cross-section and an ideal step edge. The x -axis is the cross-section width while the y -axis represents magnitude. (a) A Gaussian line cross-section and an ideal step edge; (b-1) the MF and (b-2) its filter response; (c-1) the FDOG and (c-2) its filter response; (d) the local mean of the response to the FDOG.

$$D_m = D * W \quad (3.3)$$

where W is a $w \times w$ filter whose elements are all $1/w^2$. The local mean image D_m is then normalized so that each element is within the interval 0 and 1. We denote by \bar{D}_m the normalized image of D_m .

The threshold T is then set as:

$$T_H = (1 + \bar{D}_m) \cdot T_c \quad (3.4)$$

where T_c is a reference threshold. We set T_c as follows:

$$T_c = c \cdot \mu_H \quad (3.5)$$

where μ_H is the mean value of the response image H , and c is a constant that can be set between 2 and 3 based on our experimental experience. By applying T to H , the final vessel map M_H is obtained as:

$$\begin{cases} M_H = 1 & H(x, y) \geq T(x, y) \\ M_H = 0 & H(x, y) < T(x, y) \end{cases} \quad (3.6)$$

It can be seen from (3.3)-(3.6) that if there is a vessel in the image, then at the corresponding area the magnitude in \bar{D}_m will be weak, and hence the threshold T_H will be lowered. Thus this vessel can be easily detected by (3.6). If there are some non-vessel structures in the image, the corresponding magnitude in \bar{D}_m will be high, and hence the threshold T_H is raised. Thus these non-vessel edges can be suppressed.

We use an example to illustrate the proposed MF-FDOG scheme in Fig. 3.3. Fig. 3.3 (a) shows an original image “im0001” from the STARE database where there are bright lesions in the middle of the image. Fig. 3.3 (b) is the response map to MF and illustrates strong responses to both vessels and the bright lesions. Fig. 3.3 (c) depicts the local mean map of the response to FDOG, i.e. \bar{D}_m . It can be seen that the FDOG response has a higher magnitude (brighter pixels) in the center area where hard exudates are located, while the surrounding vessels produce a lower magnitude (darker pixels). Fig. 3.3 (d) is the vessel extraction result of the MF by applying a global threshold to Fig. 3.3 (b), while Fig. 3.3 (e) is the result of the proposed approach. It can be clearly viewed that the false detection caused by the bright lesion is greatly reduced, while many fine vessels missed in Fig. 3.3 (d) are detected in Fig. 3.3 (e). The ground truth for this image is shown in Fig. 3.3 (f). We see that the proposed MF-FDOG scheme more effectively discriminates between true retinal vessels and non-vessel edges than the conventional MF.

3.4 Experimental Results

In order to extract both thick and thin vessels in the retinal image, we apply a multi-scale MF-FDOG approach. In other words, we use a large scale to detect thick vessels and a small scale to locate thin vessels. The results of both extractions are then combined using the logical OR operation. More on multi-scale in Section 6.3.1. The key parameters in our experiments were set as follows: $s = 1.5$ and $L = 9$ (used for wide vessels), $s = 1$ and $L = 5$ (used for thin vessels) (refer to (3.1) and (3.2)), $W = 31 \times 31$ (refer to (3.3)), and $c = 2.3$ (refer to (3.5)) and 8 directions were used in MF-FDOG filtering. These parameters were chosen based on our experimental experience.

We tested the proposed MF-FDOG method on two publicly available databases, STARE database and the DRIVE database. The STARE database consists of retinal images captured by the TopCon TRV-50 fundus camera at a 35° field of view (FOV), which were digitized with 24-bit gray-scale resolution and a spatial resolution of 700×605 pixels. There are 20 images, ten of which are from healthy ocular fundus and the other ten are from unhealthy ones. The database also provides hand-labeled images as the ground truth for vessel segmentation so that the algorithms can be evaluated for comparison. The DRIVE database consists of 40 images captured by the Canon CR5 camera at 45° FOV, which were digitized at 24 bit with a spatial resolution of 565×584 pixels. The 40 images were divided into a training set and a test set by the authors of the database. The results of the manual segmentation are available for the two sets. For the images in the test set, a second independent manual segmentation is also available.

To compare different retinal vessel segmentation algorithms, we select (3.7) detection accuracy, (3.8) the corresponding TPR (true positive rate), and (3.9) the FPR (false positive rate) at that accuracy as our performance measurements. These performance measurements are defined and widely used in literature [23], [25], [26], [27], [28], [29], [30], [31], [32], and is considered the norm in vessel extraction. The detection accuracy is defined as the ratio of the total number of correctly classified pixels to the number of pixels inside the FOV. The TPR is defined as the ratio of the number of correctly classified vessel pixels to the number of total vessel pixels in the ground truth. The FPR is defined as the ratio of the number of non-vessel pixels inside the FOV but classified as vessel pixels, to the number of non-vessel pixels inside the FOV in the ground truth.

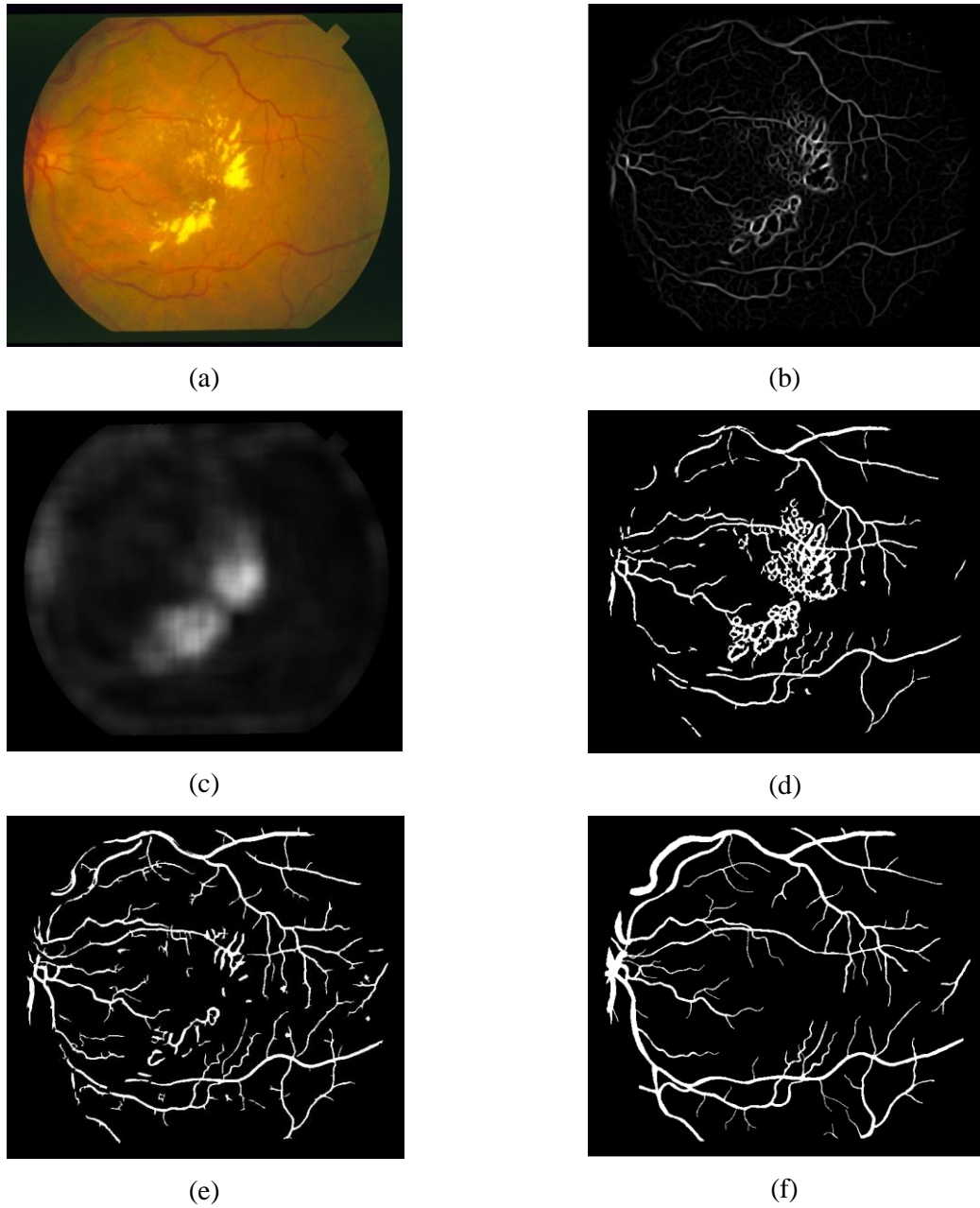


Figure 3.3: Illustration of the proposed MF-FDOG retinal vessel extraction scheme. (a) The original image im0001 from the STARE database. (b) The response map to MF. (c) The local mean of the response to FDOG. (d) The vessel extraction result after applying a global threshold to the MF response map. (e) The extraction result of the proposed scheme. (f) The ground truth vessel map.

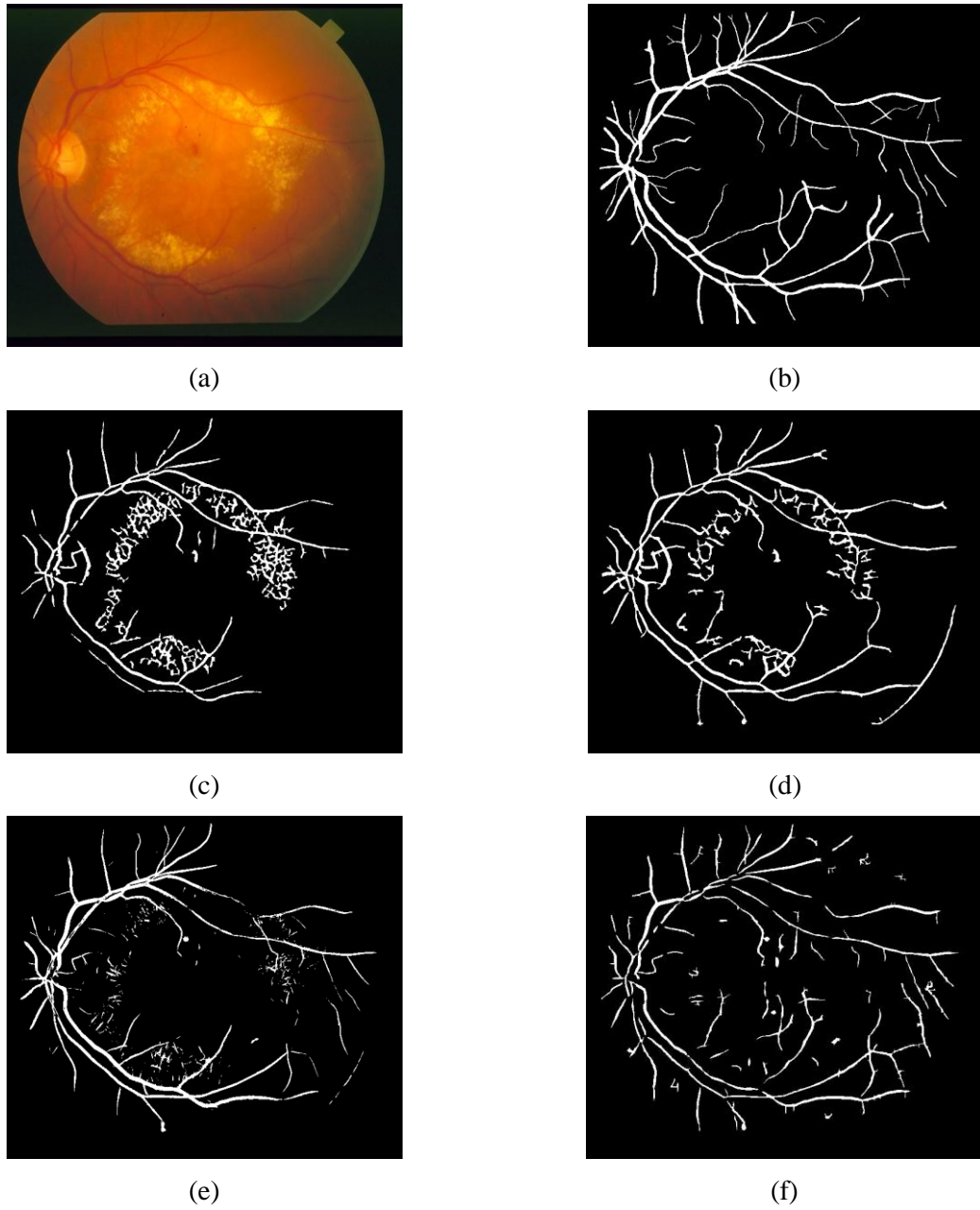


Figure 3.4: (a) The original image im0002 from the STARE database; (b) The ground truth vessel map; the vessel extraction results by (c) MF; (d) Hoover [29]; (e) Soares [26]; and (f) the proposed MF-FDOG.

$$accuracy = \frac{(TP + TN)}{(P + N)} \quad (3.7)$$

$$TPR = \frac{TP}{(TP + FN)} \quad (3.8)$$

$$FPR = \frac{FP}{(FP + TN)} \quad (3.9)$$

Table 3.1: Vessel extraction results on the STARE database.

Method	TPR	FPR	Accuracy
2nd Human observer	0.8949	0.0610	0.9354
Hoover [29]	0.6751	0.0433	0.9267
Staal [25]	0.6970	0.0190	0.9516
Soares [26]	0.7165	0.0252	0.9480
Mendonça [31]	0.6996	0.0270	0.9440
Martinez-Perez [32]	0.7506	0.0431	0.9410
Matched filter [34]	0.6134	0.0245	0.9384
MF-FDOG	0.7177	0.0247	0.9484

Table 3.1 presents the experimental results on the STARE database by different methods. The performance measures of Staal [25], Mendonça [31] and Martinez-Perez [32] were obtained from their original papers. For Soares [26] and Hoover [29], their performance measures were calculated using the segmented images from their websites. The FOV used for the STARE database was generated by the code provided by Soares. All 20 images in STARE were used in this experiment. (Staal’s method [25] used 19 of the 20 images for testing with 10 normal and 9 pathological). The hand-labeled images by the first human expert were used as ground truth. The TPR measure of Martinez-Perez’s method [32] is higher than others because it was calculated at a higher FPR level. Overall its accuracy is similar to that of others. To facilitate the comparison of our method with

Soares’ [26] and Mendonça’s [31] methods, we calculated the average TPR corresponding to an FPR of around 0.025. The experimental results on the STARE database show that the proposed MF-FDOG performs much better than the original MF, also outperforms Hoover’s and Mendonça’s methods, and is slightly better than Soares’ method. It has similar performances to the other state-of-the-art methods but with much less computational cost.

Table 3.2: Vessel extraction results on the STARE database (normal vs. abnormal cases).

Method	TPR	FPR	Accuracy
Normal cases			
2 nd Human observer	0.9646	0.0764	0.9283
Hoover [29]	0.6766	0.0338	0.9324
Mendonça [31]	0.7258	0.0209	0.9492
Soares [26]	0.7554	0.0188	0.9542
Matched filter [34]	0.7335	0.0218	0.9486
MF-FDOG	0.7526	0.0221	0.9510
Abnormal cases			
2 nd Human observer	0.8252	0.0456	0.9425
Hoover [29]	0.6736	0.0528	0.9211
Mendonça [31]	0.6733	0.0331	0.9388
Soares [26]	0.6869	0.0318	0.9416
Matched filter [34]	0.5881	0.0384	0.9276
MF-FDOG	0.7166	0.0327	0.9439

As stated before, one important motivation of the proposed MF-FDOG method is to suppress the false response of MF to lesions and blobs that will often appear in the abnormal retinal images. In order to demonstrate the performance of our method in such pathological cases, we compared the results by different methods on the normal and abnormal images in the STARE database (see Table 3.2). Since the result of Staal’s method [25] is not available for this experiment, it is not listed in Table 3.2. The experimental results clearly show that for the abnormal cases, the proposed MF-FDOG method performs significantly better than the MF and Hoover’s method, and it achieves better results

than Mendonça’s and Soares’ methods. Fig. 3.4 shows an example for visual inspection. The color fundus image (a) contains a lot of hard exudates in a circular region along the middle. With MF, Hoover and Soares shown in (c), (d) and (e) respectively, most of the hard exudates are extracted along with vessels. However, using the proposed method (f) only a few strains of hard exudates are segmented while the majority of the vessel map is extracted compared to (b), the ground truth of (a).

Table 3.3: Vessel extraction results for the DRIVE database.

Method	TPR	FPR	Accuracy
2nd Human observer	0.7761	0.0275	0.9473
Staal [25]	0.7194	0.0227	0.9442
Soares [26]	0.7283	0.0212	0.9466
Mendonça [31]	0.7344	0.0236	0.9452
Matched filter [34]	0.6168	0.0259	0.9284
Jiang [30]	–	–	0.9212
Zana [115]	–	–	0.9377
Martinez-Perez [32]	0.7246	0.0345	0.9344
Garg [116]	–	–	0.9361
Perfetti [128]	–	–	0.9261
Cinsdikici [129]	–	–	0.9293
Al-Rawi [130]	–	–	0.9510
MF-FDOG	0.7120	0.0276	0.9382

The proposed MF-FDOG is competitive with other state-of-the-art methods when using the STARE database (see Table 3.1), and is particularly strong in all three performance measures when dealing with abnormal cases (see Table 3.2). It falls behind some state-of-the-art methods when the DRIVE database is used (see Table 3.3) because the proposed MF-FDOG has advantages in dealing with pathological retinal images but most of the images in the DRIVE test set are normal images from healthy subjects. Nevertheless, we show an example of vessel extraction using DRIVE in Fig. 3.5. In addition, some non-vessel structures in retinal images can be very complex and hard to be modeled by step edges. We admit that in such cases our method may fail.

To evaluate the proposed MF-FDOG with respect to higher true positives with false positives < 0.05 , we plot the ROC curves for both the DRIVE (dotted line) and STARE (solid line) database in Fig. 3.6. Each point on the curve represents a different threshold value used to segment the vessels. We can see that the proposed MF-FDOG method has good performance when $FP > 0.02$.

In Table 3.4 we list the running time of our method in comparison with state-of-the-art methods [26], [31]. We see that the MF-FDOG requires much less computational cost. Without optimization of the code, it will take about 10 seconds to process one image in the STARE database on a PC with a P-III 1.5 GHz CPU and 512MB RAM.

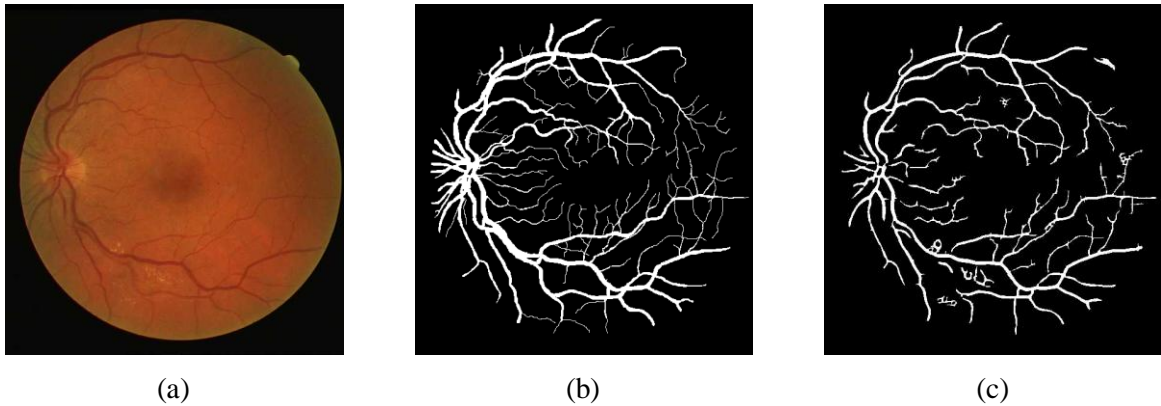


Figure 3.5: The original image 3 from the DRIVE database; (b) The ground truth vessel map; the vessel extraction result by (c) the proposed MF-FDOG.

Table 3.4: Running time per image on the STARE database.

Method	System Environment	Running Time
Soares [26]	P-III 1.5GHz, 512 Mb RAM, Matlab	3.5 minutes
Mendonça [31]	P-IV 3.2GHz, 960 Mb RAM, Matlab	3 minutes
MF-FDOG	P-III 1.5GHz, 512 Mb RAM, Matlab	10 seconds

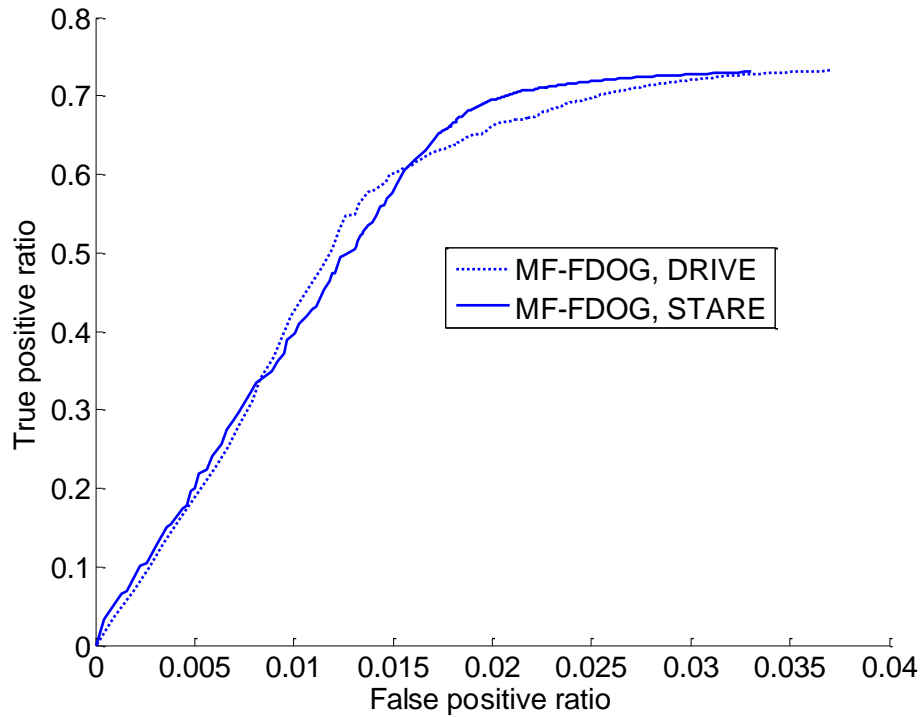


Figure 3.6: ROC curves for both STARE and DRIVE with $FP < 0.05$ by the proposed method. The solid line represents STARE while the dotted line is DRIVE.

3.5 Summary

We proposed a novel retinal blood-vessel extraction method, namely the MF-FDOG, by using both the MF and FDOG. The retinal vessels were detected by simply thresholding the retinal image's response to the MF but the threshold was adjusted by the image's response to the FDOG. Compared with the MF, the MF-FDOG can better distinguish the true vessel structures from non-vessel structures such as blobs and lesions. The experimental results demonstrated that it significantly reduces the false detections generated by the MF and detects many fine vessels that the MF will miss. In particular, the MF-FDOG can extract effectively the vessels in pathological images, leading to competitive results as compared with state-of-the-art schemes; at the same time it has much lower complexity and is easier to implement. In the next chapter we move on to the second feature to be analyzed in retinal images: microaneurysms. We propose an algorithm to detect microaneurysms based on MSCF. The algorithm is hierarchical and composed of two levels. The first level locates all

possible microaneurysms candidates, while the second prunes those candidates whose feature values fail to meet some criteria.

Chapter 4

Detection of Microaneurysms using Multi-scale Correlation Coefficients

A new approach based on MSCF is developed in this chapter to detect microaneurysms. This consists of two levels, Microaneurysm Candidate Detection (coarse level Section 4.1) which detects all possible candidates in a fundus image, and True Microaneurysm Classification (fine level Section 4.2) using feature extraction to build a discrimination table. The approach was evaluated (Section 4.3) using data from Retinopathy On-line Challenge (ROC) and we conclude with a summary in Section 4.4.

4.1 Coarse Level: Microaneurysm Candidate Detection

The task of course-level detection is to identify all possible microaneurysm candidates in a retinal image. Fig. 4.1 (a) and (b) show two microaneurysms that were found in Fig. 1.4 (b) (shown in its green channel) and Fig. 4.1 (c) and (d) show their corresponding gray-scale distributions. As can be seen, microaneurysms exhibit a Gaussian shape. This allows us to use a Gaussian function to detect microaneurysms according to the similarity between the distributions of its gray-scale. The Gaussian function can be defined as:

$$G(x, y) = \frac{1}{2 \cdot \pi \cdot \sigma^2} \exp\left(\frac{-x^2 + y^2}{2 \cdot \sigma^2}\right) \quad (4.1)$$

with its distribution shown in Fig. 4.2.

The correlation coefficient is a good way to measure the resemblance between the Gaussian function and gray-scale distribution of microaneurysms. If the two match, the correlation coefficient will be high and if they don't, the value will be low. The range of the coefficient is from 0 to 1.

The correlation function is defined as:

$$r = \frac{\sum_m \sum_n (A_{mn} - \bar{A})(B_{mn} - \bar{B})}{\sqrt{\left(\sum_m \sum_n (A_{mn} - \bar{A})^2\right) \left(\sum_m \sum_n (B_{mn} - \bar{B})^2\right)}} \quad (4.2)$$

where \bar{A} and \bar{B} are the mean.

Since microaneurysms vary in size, different sigma values for the Gaussian kernel are required. For this purpose we include the selection of multiple scales in order to match various microaneurysm

dimensions. Fig. 4.3 (a, c and b, d) shows the responses and maximum correlation coefficients to different Gaussian kernels of the same two microaneurysms depicted in Fig. 4.1. Images (a, c) on the left show the responses of Fig. 4.1 (a) to small and large kernels respectively. Images (b, d) on the right show the same thing but using Fig. 4.1 (b). From Fig. 4.3 it can be seen that applying one scale does not guarantee detection of the maximum coefficient as response Fig. 4.3 (a) has a greater coefficient using the smaller scale Gaussian kernel while response Fig. 4.3 (d) produces a higher coefficient using the larger scale kernel.

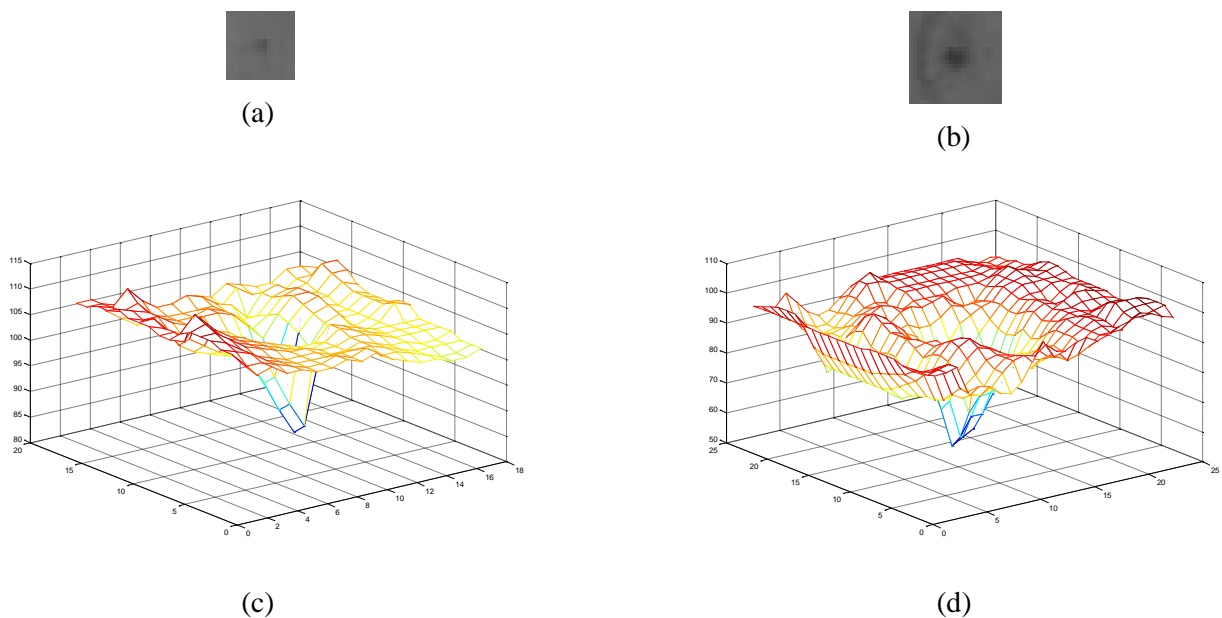


Figure 4.1: The detection of microaneurysms in a color retinal image. (a) and (b) illustrate two microaneurysms found in Fig. 1.4 (b). The corresponding mesh plots of (a) and (b) are shown in (c) and (d) respectively.

The first step in coarse level candidate detection involves applying a sliding neighborhood filter with multi-scale Gaussian kernels to the fundus image in order to calculate a correlation coefficient for each pixel. Because microaneurysms are circular, the Gaussian kernels are also circular as this will ensure that the response (a correlation coefficient) will be high. Based on extensive experimentation, we chose five scales for the kernel to represent microaneurysms of different sizes with the sigma of the Gaussian function being 1.1, 1.2, 1.3, 1.4 and 1.5. The maximum coefficients

from each of the five responses are combined to form a final response. Fig. 4.4 depicts the final response, where Fig. 4.4 (a) is an input retinal image and Fig. 4.4 (b) is the output. The brighter spots seen in Fig. 4.4 (b) have a higher coefficient and therefore are more likely to be true microaneurysms.

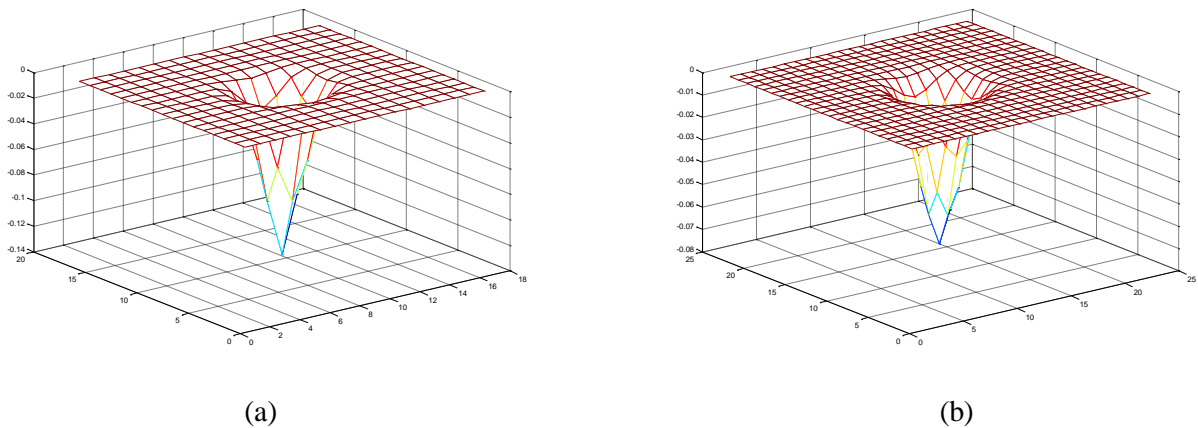


Figure 4.2: The mesh plots of the Gaussian kernel with different scale factors. (a) scale factor = 1 and (b) scale factor = 1.5.



Figure 4.3: The responses of microaneurysms to different Gaussian kernels. (a) and (b) are responses for microaneurysms in Fig. 4.1 (a) and (b) at a small scale, (c) and (d) are responses for microaneurysms in Fig. 4.1 (a) and (b) at a larger scale, where the maximum coefficient is placed below each response.

A threshold is next applied in order to determine the number of microaneurysm candidates. Application of a threshold creates a binary image as seen in Fig. 4.5. Binary images are easier to analyze than the coefficient image, but often cannot be converted directly without some preprocessing. Hence, there is a need to threshold the coefficient image to obtain its binarized version where foreground and background regions can be segmented. A threshold value T is used to accomplish this by partitioning the coefficient image pixels to two values (0 and 1), using the following algorithm:

$$\begin{aligned} &\text{if } coef(x, y) \geq T \text{ then } b(x, y) = 1 \\ &\text{else } b(x, y) = 0 \text{ since } coef(x, y) < T \end{aligned} \quad (4.3)$$

where $coef(x, y)$ denotes the coefficient image and $b(x, y)$ denotes the binarized version of $coef(x, y)$. In our case the threshold value is set to 0.4 in order to segment Fig. 4.4 (b).

Since microaneurysms cannot occur on blood vessels, adaptive thresholding [131] was used to first locate the vessels and remove any spots on them, thereby reducing the number of candidates. Fig. 4.6 shows a vascular map, where Fig. 4.6 (a) is an original image and Fig. 4.6 (b) is the output of the corresponding vascular map with all the blood vessels detected after adaptive thresholding. Any candidates on these vessels are removed from Fig. 4.5 and the result can be seen in Fig. 4.7.

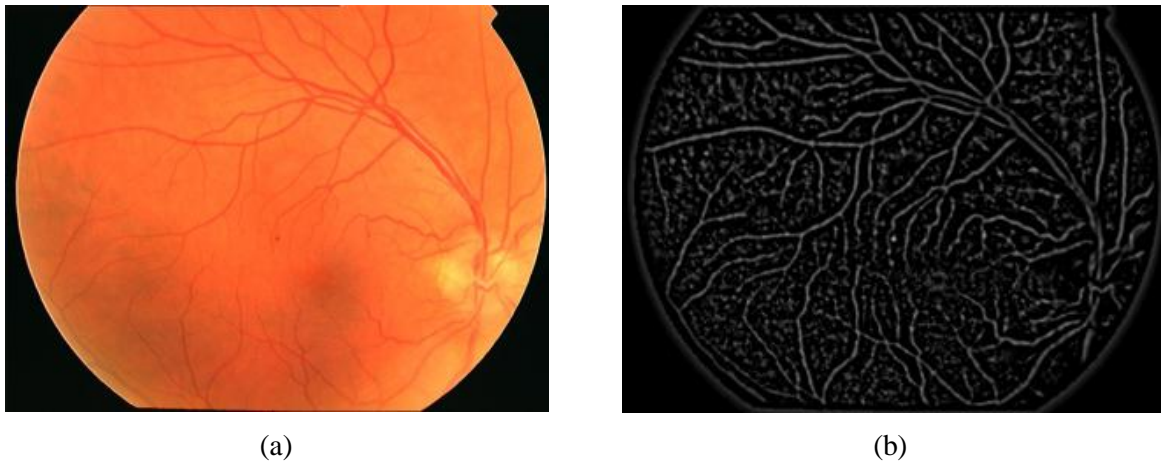


Figure 4.4: The final response of a testing image. (a) the input retinal image (b) the output.



Figure 4.5: Result after segmenting Fig. 4.4 (b) with a threshold of 0.4. The white spots marked are possible microaneurysms.

The candidate microaneurysms that remain in Fig. 4.7 at this point do not represent the true microaneurysm size; therefore, we apply region growing based on [17]. We first calculate the gray-scale intensity pixel value(s) for each candidate (i_{green} for I_{green} and i_{bg} for I_{bg}). I_{bg} is the background of I_{green} and is computed by applying a median filter of size 25×25 to I_{green} . The lowest intensity in i_{green} ($I_{darkest}$) is also required. These values are used to find a threshold t where:

$$t = I_{darkest} - x \cdot (I_{darkest} - i_{bg}) \quad (4.4)$$

In this chapter x is set to 0.5. The value t is then used to segment I_{green} into a binary image where region growing begins from the pixel having intensity $I_{darkest}$ and terminates when no more pixels are connected to it. If the resultant region is greater than 120 pixels it is discarded as no true microaneurysm can be that large. Fig. 4.8 shows the result of region growing for the candidates in Fig. 4.7.

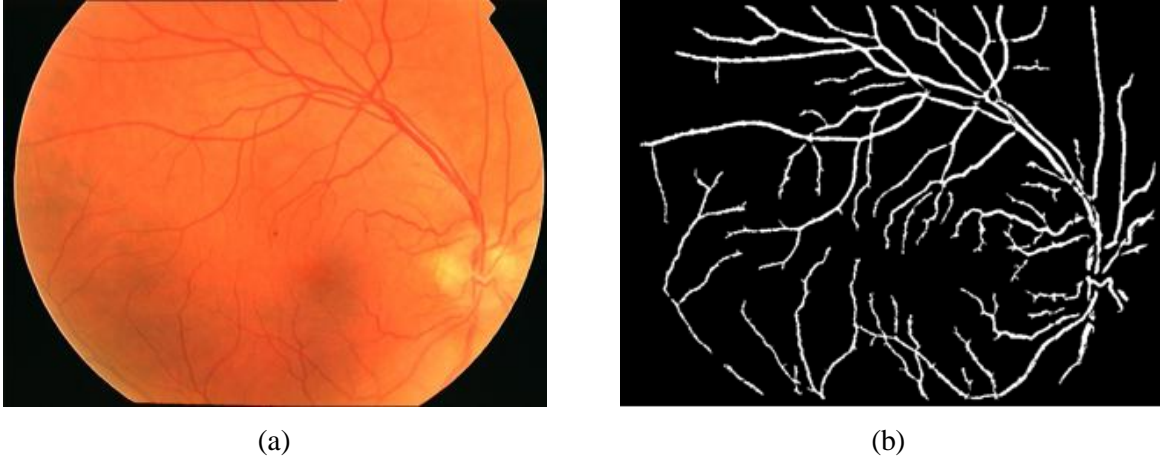


Figure 4.6: The vascular map of a retinal image. (a) the sample image given in Fig. 4.4 (a) and (b) the output of its vascular map.

Table 4.1: The list of 31 features.

Feature Number	Feature Description
1	The area a of the candidate. Microaneurysms have a small area compared to other objects in the retina.
2	The perimeter p of the candidate. Microaneurysms have a small perimeter compared to other objects in the retina.
3	The aspect ratio $r = l/w$ where l and w are the major and minor axis lengths of the candidate. For a true microaneurysm its major and minor axis should be quite similar.
4	The circularity $c = (4 \cdot \pi \cdot a)/p^2$. True microaneurysms are circular in shape.
5	The total intensity i_{green} of the candidate in I_{green} . True microaneurysms have higher intensities.
6	The total intensity i_{SC} of the candidate in I_{SC} .
7	The average intensity of i_{green} , $m_{green} = i_{green}/a$.
8	The average intensity of i_{SC} , $m_{SC} = i_{SC}/a$.
9	The normalized intensity in I_{green} , $NI_{green} = (1/\sigma) \cdot (i_{green} - x)$ where σ and x are the

	standard deviation and mean pixel value of I_{bg} .
10	The normalized intensity in I_{SC} , $NI_{SC} = (1/\sigma) \cdot (i_{SC} - x)$.
11	The normalized average intensity in I_{green} , $NM_{green} = (1/\sigma) \cdot (m_{green} - x)$.
12	The normalized average intensity in I_{SC} , $NM_{SC} = (1/\sigma) \cdot (m_{SC} - x)$.
13	The intensity of $I_{darkest}$ in I_{match} .
14	The compactness: $v = \sqrt{\sum(d_i - d)^2/n}$ where d_i is the distance of each boundary pixel of the candidate to its center, d is the mean of all these distances and n is the number of boundary pixels. True microaneurysms are compact.
15	The difference between the average pixel values of the candidate and a circular region (not including the candidate) centered on it in the red channel (RGB color space). The circular region is calculated by dilating the candidate with a disk of radius 6. Since microaneurysms have a Gaussian distribution when examining its gray-scale values, the contrast of the microaneurysm with its background should be high.
16 – 18	Repeat feature 15 but in the green channel, blue channel and hue channel from the HSI color space.
19 – 22	The average Gaussian filter response of I_{green} with $\sigma = 1, 2, 4,$ and 8 .
23 – 26	The standard deviation response of I_{green} after Gaussian filtering with $\sigma = 1, 2, 4,$ and 8 .
27 – 29	The maximum, minimum and average correlation coefficient of the candidate. Candidates with a higher coefficient are more likely to be true microaneurysms.
30	The major axis length of the candidate. Generally, microaneurysms do not have a significant major or minor axis length.
31	The minor axis length of the candidate.

4.2 Fine Level: True Microaneurysm Classification

The task of fine level microaneurysm detection is to detect true microaneurysms in the candidate set, which can be implemented through feature extraction. We used a total of 31 features for each candidate, based on shape, gray-scale pixel intensity, color intensity, responses of Gaussian filter-banks, and correlation coefficient values. Table 4.1 lists the 31 features used to discriminate

microaneurysms in our proposed approach. Features 27-29 are unique to the proposed method as it is based on the correlation coefficient of each pixel, calculated beforehand. The last two features, major and minor axis length are added to diversify the already existing shape features.



Figure 4.7: The remaining candidates from Fig. 4.5 after candidates on the blood vessels were removed.

Some of the features listed require I_{SC} and I_{match} . Below we describe how they are calculated. I_{SC} is I_{green} with the background removed computed as $I_{green} - I_{bg}$ and can be seen in Fig. 4.9. Blood vessels in I_{SC} are located with morphological open using 12 line structures of length 9 pixels rotated at 15° . The maximum pixel values after applying the 12 structures show only the blood vessels. These vessels are then subtracted from I_{SC} to form I_{lesion} , where the linear structures are removed and microaneurysms are kept. To improve the contrast of I_{lesion} in order to make microaneurysms stand out from its background, an 11×11 Gaussian filter with $\sigma = 1$ is convoluted with I_{lesion} . The result of which is I_{match} depicted in Fig. 4.10.



Figure 4.8: Result of region growing on the candidates in Fig. 4.7.

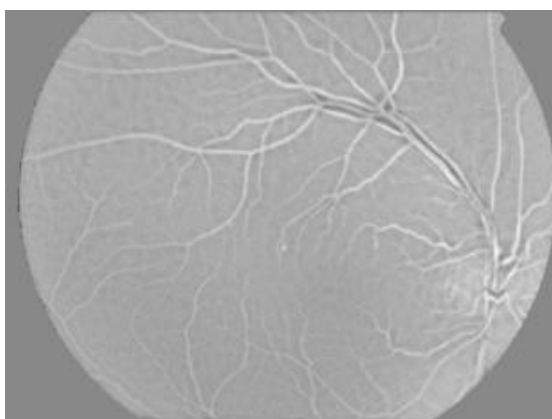


Figure 4.9: Sub-band image I_{SC} obtained by subtracting I_{bg} from I_{green} .

After features are extracted from the candidates, the feature vector is divided into two groups: true microaneurysms and false microaneurysms (The details of this process are summarized in Section 4.3). The minimum and maximum values of each feature in the true microaneurysms group are obtained and stored in a discrimination table, see Table 4.2. The 31 features are given a number in the leftmost column and the minimum and maximum values for that feature can be read off the adjacent columns. This table can be used to eliminate any candidates whose feature values are greater than maximum or less than minimum. For example, Feature 16 which computes the contrast of the candidate and its surrounding area in the green channel, the minimum value was manually set to 8. By manually setting this value to be higher than the actual minimum of Feature 16, some true and many

false microaneurysm candidates are removed. This feature was specifically chosen since the contrast between a microaneurysm and its surrounding background is known to be high (in the green channel). The remaining candidates whose feature values are between minimum and maximum are the final detected microaneurysms. We applied this table to the candidates drawn from Fig. 4.8 and obtained the result in Fig. 4.11. The true candidates are then mapped back to the original image to show the location of true microaneurysms (inside the green squares, shown in Fig. 4.11 (c)). As can be seen, a significant number of candidates have been removed (from Fig. 4.11 (b)). For the final output image given in Fig. 4.11 (c), all true microaneurysms were detected with no false positives.

Table 4.2: The discrimination table of different retinal features.

Feature Number	Min.	Max.	Feature Number	Min.	Max.
1	2	109	17	-27.1471	6.368521
2	2	113.0122	18	-0.01944	0.002723
3	1	5.618986	19	27.66061	179.0988
4	0.090521	6.283185	20	0.01962	8.292589
5	58	10676	21	30.81245	180.773
6	338	19451	22	0.044188	6.747434
7	25.17241	177.0417	23	36.00843	182.7637
8	104.8125	221.9348	24	0.003416	3.00799
9	-0.31038	203.8908	25	37.95791	183.7483
10	6.138524	448.9355	26	0.009462	1.797795
11	-1.15234	0.921628	27	0.106603	0.785072
12	0.164831	5.08576	28	0	0.547187
13	7	255	29	0.053335	0.658546
14	0	3.743681	30	2.309401	29.53404
15	-31.368	2.863946	31	1.154701	14.09998
16	8	35.37533			

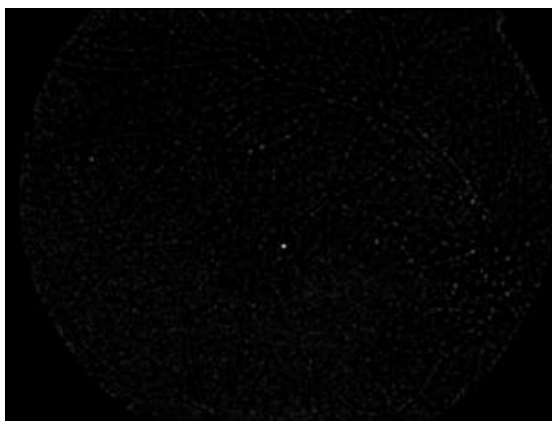


Figure 4.10: Matched image I_{match} which shows possible microaneurysms. This image was processed by removing vessels from Fig. 4.9 and enhancing its result with a Gaussian filter.

4.3 Experimental Results and Analysis

The experimental results reported in this section are mainly based on our work submitted to ROC, an international competition. The score of our submission was ranked second among all participants. Details of the ROC competition are available on their website [132]. The following summarizes our testing results and comparison with other methods for performance evaluation.

A sequence of experiments was conducted on 100 images (split into 50 training and 50 test) in the public retinal image database provided on the ROC competition website [132]. The images were all taken with Topcon NW 100, NW 200 or Canon CR5-45NM ‘non-mydrionic’ cameras at the default resolution and compression settings from patients with diabetes without known diabetic retinopathy (at the moment of photography). The images are a random sample of all patients that were noted to have ‘microaneurysms’ from a large (> 10,000 patients) diabetic retinopathy screening program, and each image is from a different patient. All images are in JPEG compressed format with sizes 768×576 , 1058×1061 , 1062×1061 , 1379×1383 , 1381×1385 , 1385×1382 , 1386×1384 , 1389×1383 , 1389×1391 and 1394×1392 pixels. Each image comes with a reference standard that marks every microaneurysm agreed upon by the consensus of 4 experts. This reference standard helps identify true microaneurysms used in building the discrimination table. Some images contained so-called ‘don’t care’ objects where a consensus could not be reached or where the objects are not microaneurysms (e.g. hemorrhages, pigment spots, etc.). We applied the proposed algorithm on all images and did not consider or use the ‘don’t care’ objects. To segment the final response after applying the kernel

functions we used threshold values ranging from 0.1 to 1.0, each time building a discrimination table according to the true microaneurysm feature values and using it to remove some candidates. We compared our algorithm with Math Morph [14], Waikato Retinal Imaging Group [108], [132], Fujita Lab [108], [132], LaTIM [108], [132], IRIA-Group [108], [132] and GIB Valladolid [108], [132]. The algorithm described in [14] was implemented by ourselves and tested with the same data as the proposed algorithm. For [108], [132] we referenced their published results (on the test dataset) since they used the ROC database as well. We were not able to compare the fusion algorithm in [24] because the reference standard provided did not label each pixel as required by this method.

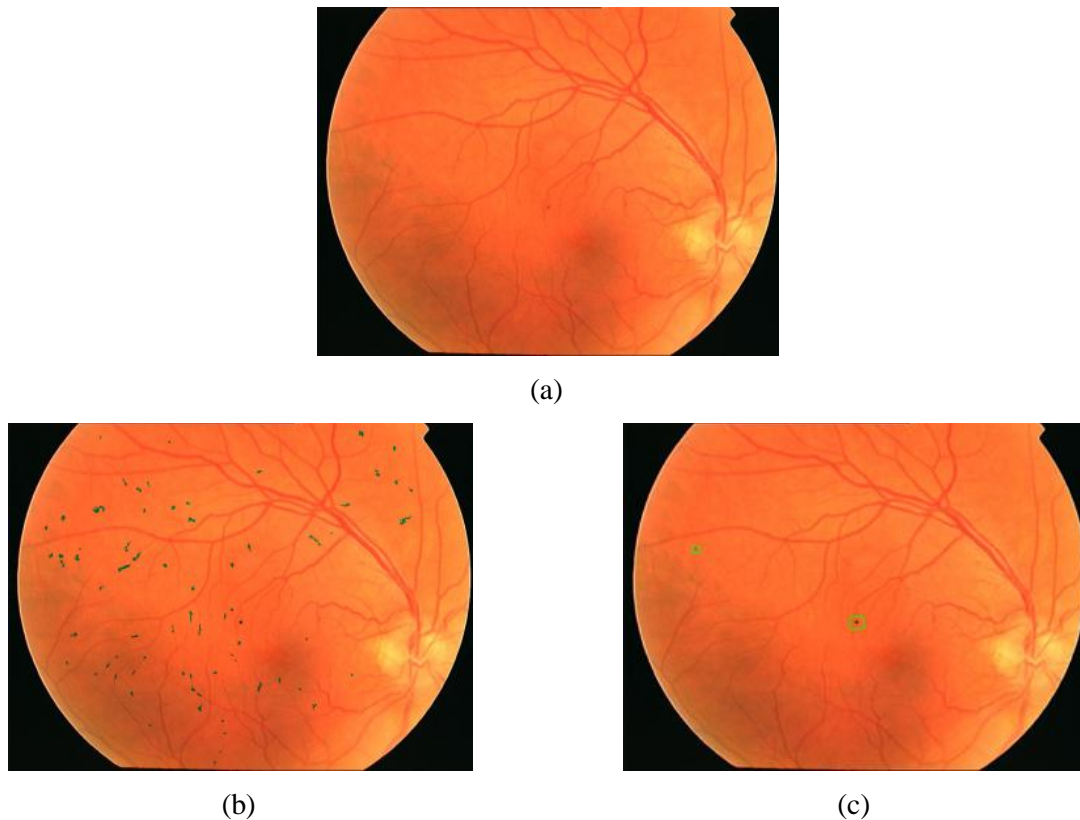


Figure 4.11: The output of microaneurysm detection. (a) the original retinal image, (b) the output of coarse-level detection and (c) the final output of fine-level classification where the green squares mark the approximate location of the detected microaneurysms using the proposed algorithm.

The performance of our hierarchical approach based on MSCF for microaneurysm detection is evaluated by plotting sensitivity against the average number of false positives per image (FROC) using the 50 training images, shown in Fig. 4.12 as a dotted curve. Sensitivity is the number of true microaneurysms correctly detected while false positive is the number of non-microaneurysms detected as true microaneurysms. Please note that the horizontal axis is in logarithmic scale. The FROC plot also contains a solid curve, which is our implementation of Math Morph. As can be seen, the majority of the dotted curve has a higher sensitivity compared with the solid curve for the same false positives per image. Table 4.3 lists the sensitivities of 1/8, 1/4, 1/2, 1, 2, 4 and 8 false positives per image of both methods derived from Fig. 4.12. In this table the proposed method has a greater sensitivity from 1/4 to 8 with the average of all seven points being 0.201 and 0.126 for Math Morph.

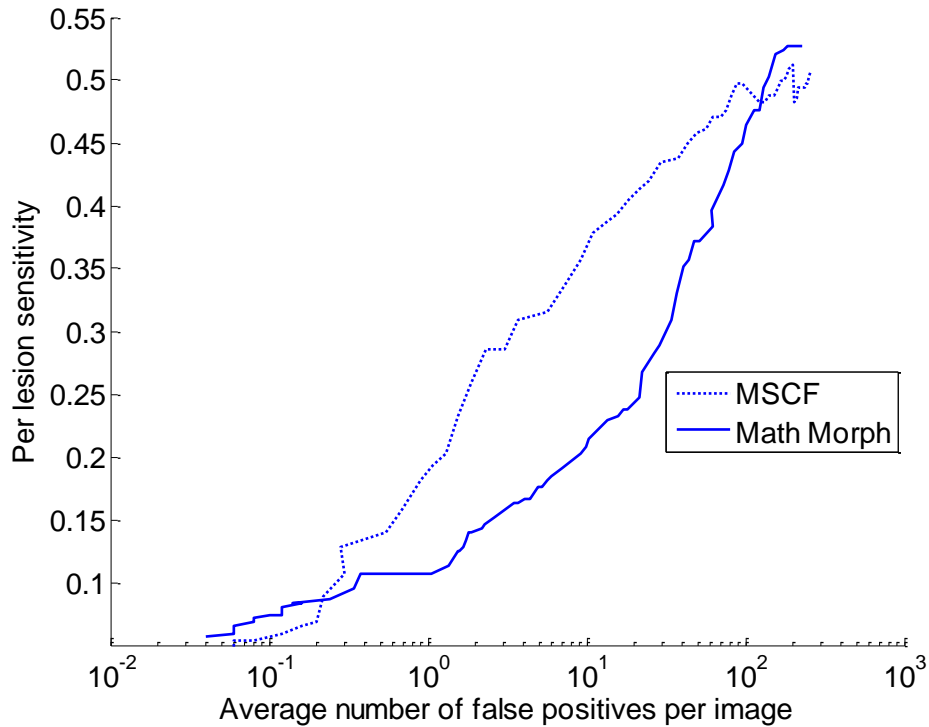


Figure 4.12: Plot of FROC comparing MSCF (dotted curve) with Math Morph (solid curve) on the training data.

Results based on the 50 test images are displayed in Fig. 4.13, also in the form of a FROC plot. Again, the dotted line represents MSCF while the solid line is Math Morph. The same trend found in

Fig. 4.12 applies to Fig. 4.13 where the majority of MSCF points are higher than Math Morph. Table 4.4 which measures the same false positives per image as Table 4.3 except for the test data with the addition of Waikato Retinal Imaging Group, Fujita Lab, LaTIM, IRIA-Group and GIB Valladolid supports the previous claim, as the sensitivity of MSCF is greater than Math Morph, Waikato Retinal Imaging Group, Fujita Lab, IRIA-Group, GIB Valladolid and is slightly worse than LaTIM. The average sensitivities being 0.206 – Waikato Retinal Imaging Group, 0.310 – Fujita Lab, 0.381 – LaTIM, 0.357 – MSCF, 0.189 – IRIA-Group, 0.322 – GIB Valladolid and 0.087 – Math Morph. The remaining true microaneurysms not detected were due to the quality of the images, the selection of sigma for the Gaussian filter, the location of the microaneurysms being too close to blood vessels and little contrast between microaneurysms and its surrounding background.

Table 4.3: The average number of false positives per image for training data.

FPs/scan	1/8	1/4	1/2	1	2	4	8	Average
MSCF	0.060	0.096	0.138	0.189	0.267	0.311	0.345	0.201
Math Morph	0.081	0.087	0.107	0.107	0.141	0.166	0.196	0.126

Table 4.4: The average number of false positives per image for test data.

FPs/scan	1/8	1/4	1/2	1	2	4	8	Average
Waikato Retinal Imaging Group	0.055	0.111	0.184	0.213	0.251	0.300	0.329	0.206
Fujita Lab	0.181	0.224	0.259	0.289	0.347	0.402	0.466	0.310
LaTIM	0.166	0.230	0.318	0.385	0.434	0.534	0.598	0.381
MSCF	0.198	0.265	0.315	0.356	0.394	0.466	0.501	0.357
IRIA-Group	0.054	0.085	0.117	0.169	0.230	0.289	0.379	0.189
GIB Valladolid	0.190	0.216	0.254	0.300	0.364	0.411	0.519	0.322
Math Morph	0.035	0.055	0.063	0.080	0.092	0.118	0.168	0.087

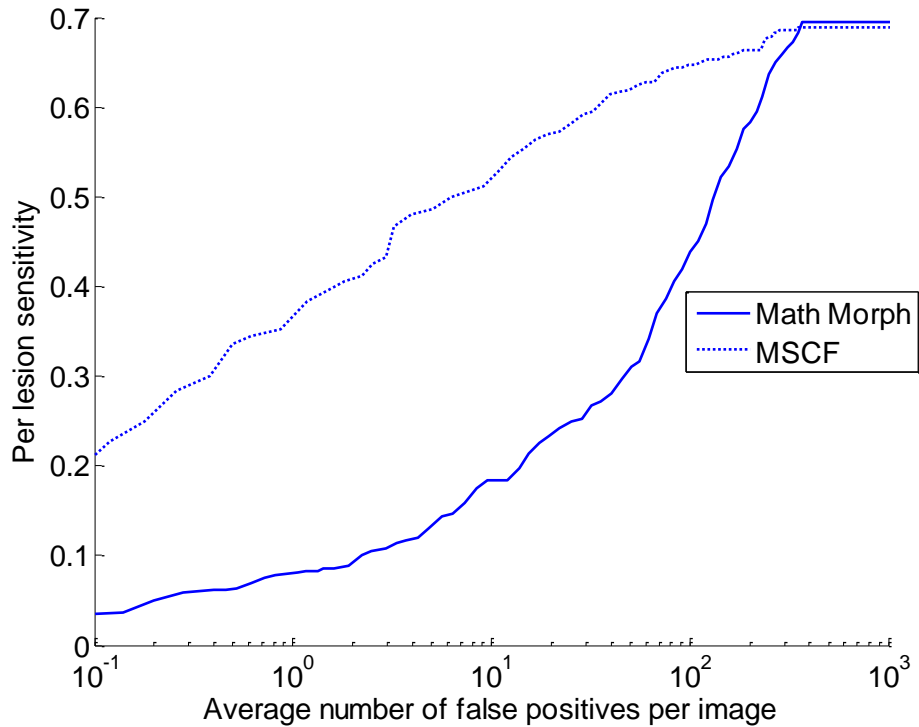


Figure 4.13: Plot of FROC comparing MSCF (dotted curve) with Math Morph (solid curve) on the test data.

The experiments raise four particular issues which require further consideration. First, there is the quality of the images, which are JPEG compressed and therefore some of the microaneurysms are too small or too blurred to be seen with the naked eye. Second, there is the choice of scales for the Gaussian kernel. The use of only small scales means that larger microaneurysms will not be extracted because the smaller kernel cannot cover/match the larger spots and thereby produces a lower correlation coefficient. The same problem arises when using a larger scale to cover/match a small microaneurysm. If such candidate microaneurysms are not detected after the coarse level they will be lost forever. Third, a few microaneurysms located next to or nearby blood vessels are removed in the coarse level. This is because these microaneurysms are recognized as part of the vascular map and therefore are removed along with real vessels. Fig. 4.14 illustrates this problem where Fig. 4.14 (a) is a cropped color retinal image with marked (green squares) microaneurysms, Fig. 4.14 (b) shows candidates detected from Fig. 4.14 (a) and Fig. 4.14 (c) is the vascular map of Fig. 4.14 (a). The central microaneurysm (enclosed in dashes) in Fig. 4.14 (a) is detected as seen in Fig. 4.14 (b) but

also appears as a vessel in Fig. 4.14 (c). This subsequently removes it as a candidate from Fig. 4.14 (b) in the next step of the coarse level. We will attempt to resolve this problem as part of the future work.

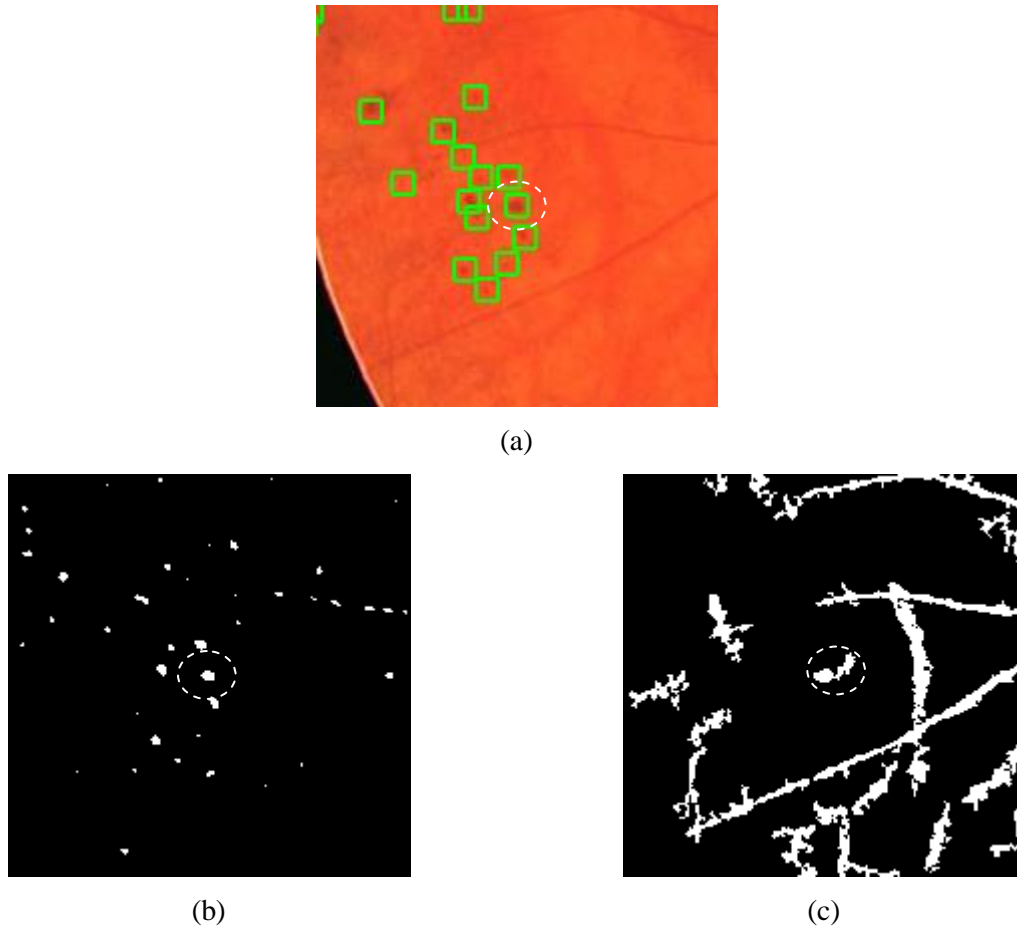


Figure 4.14: True microaneurysm being recognized as part of the blood vessel. (a) A cropped retinal image marked with true microaneurysms. (b) candidates detected in (a). (c) vascular map of (a). The central microaneurysm enclosed with dashes in (a), and (b) is detected as part of the blood vessel in (c).

A fourth issue for further consideration relates to the effect of contrast on true and false detected microaneurysms. When true microaneurysms have a low contrast with its background, as can be seen with examples in Fig. 4.15, the microaneurysm will not exhibit a Gaussian shape and it becomes

difficult for the Gaussian kernels to produce a high correlation coefficient (see Table 4.5). From our results several of the spots detected as false microaneurysms are circular in shape and have significant contrast with its background which explains its high correlation coefficient. Of these, some are possibly microaneurysms (where a consensus was not reached by the 4 experts). Fig. 4.16 shows four examples of these contentious spots with Table 4.6 displaying their correlation coefficients. We deem these objects reasonable to be detected as they resemble true microaneurysms.

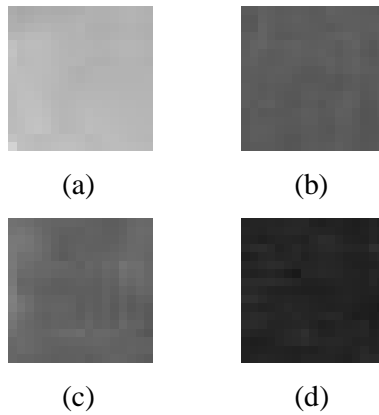


Figure 4.15: True microaneurysms with low contrast.

Table 4.5: True microaneurysms with low intensity contrast.

True Microaneurysm	Max. response
Fig. 4.15 (a)	0.1696
Fig. 4.15 (b)	0.1624
Fig. 4.15 (c)	0.1934
Fig. 4.15 (d)	0.1715

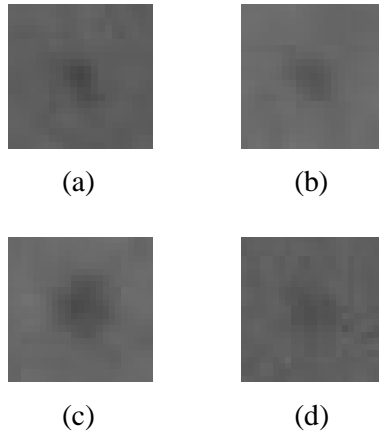


Figure 4.16: False positive microaneurysm candidates with high contrast.

Table 4.6: Examples of false positive candidates that resemble true microaneurysms.

False Microaneurysm	Max. response
Fig. 4.16 (a)	0.7527
Fig. 4.16 (b)	0.7235
Fig. 4.16 (c)	0.6564
Fig. 4.16 (d)	0.6269

4.4 Summary

We proposed a hierarchical approach based on Multi-scale Correlation Filtering to detect all microaneurysms from color retinal images. This consisted of Coarse Level: Microaneurysm Candidate Detection using MSCF and Fine Level: True Microaneurysm Classification. The approach was evaluated extensively using the public retinal image database provided on the ROC competition website [132] as part of our participation in this event. We conclude that the proposed approach is effective and efficient for intensity-based microaneurysm detection and localization for DR diagnosis. In the following chapter we propose another microaneurysm detection method using Dictionary and Centralized Dictionary Learning with Sparse Representation Classifier. Instead of extracting features from each microaneurysm, their whole structure becomes part of the training set, and combines to form a dictionary in which to classify microaneurysm candidates.

Chapter 5

Microaneurysm Detection via Dictionary and Centralized Dictionary Learning with Sparse Representation Classifier

Microaneurysm (MA) detection via Dictionary and Centralized Dictionary Learning with Sparse Representation Classifier (SRC) is given in this chapter. An introduction is first provided in Section 5.1. Sparse Representation Classifier is then explained in Section 5.2. This is followed by a description of the Dictionary Learning (DL) model for both Dictionary and Centralized Dictionary Learning (CDL) with Sparse Representation Classifier in Section 5.3. In Section 5.4 we describe how this method is applied to microaneurysm detection. Experimental results and a summary are provided in Sections 5.5 and 5.6.

5.1 Introduction

In this chapter we propose a two step method to detect and classify microaneurysm. In the first step, MSCF is applied to retinal images to locate all possible MA candidates. Two dictionaries are then learnt from example MA and non-MA objects to characterize the MA and non-MA structures. With the learnt MA and non-MA dictionaries, Sparse Representation Classifier is applied to the candidates to distinguish MA objects from non-MA objects. Although Dictionary Learning with SRC achieves good MA detection results, this method can be further improved by introducing a class discrimination term into the Dictionary Learning model. For the new DL process, we not only minimize the reconstruction error of the training samples, but also minimize the variance of the sparse coding coefficients of MA and non-MA objects. In this way the learnt MA and non-MA dictionaries aim to represent the candidate (in question) from the same class to be as close to its class center as possible.

5.2 Sparse Representation Classifier

Given a test sample and a set of training samples, the idea of SRC is to represent the test sample as a linear combination of the training samples, while requiring the representation coefficients are as sparse as possible. If the test sample is from class i , then among its representation coefficients over all the training samples, only those from the samples in class i will be significant while others will be insignificant, and hence the class label of the test sample can be determined. In practice, the l_1 -norm minimization is used to solve the sparsest linear representation of the test sample over the training samples. As an example Fig. 5.1 illustrates the idea of SRC applied to face recognition [133]. Given a

testing input to the left of (a), the purpose of [133] is to identify the face. This is accomplished by plotting (a) the representation coefficients (calculated via l_1 -norm minimization) vs. training samples/dictionary (1207 faces from 38 individuals). From this plot it can be clearly seen that the highest/significant coefficients are found in the beginning of the x -axis. This means the face belongs to an individual whose samples occupy that area. To determine the testing input's identity its Residual is computed. Residual is given as the testing sample subtracted by the training samples multiplied by the representation coefficients. The smallest residual signifies class membership. In plot (b), Residual vs. Subject the identity of the testing input is made clear as the smallest Residual is found in Subject 1, which means the testing input belongs to Subject 1. More information about SRC can be found in [133].

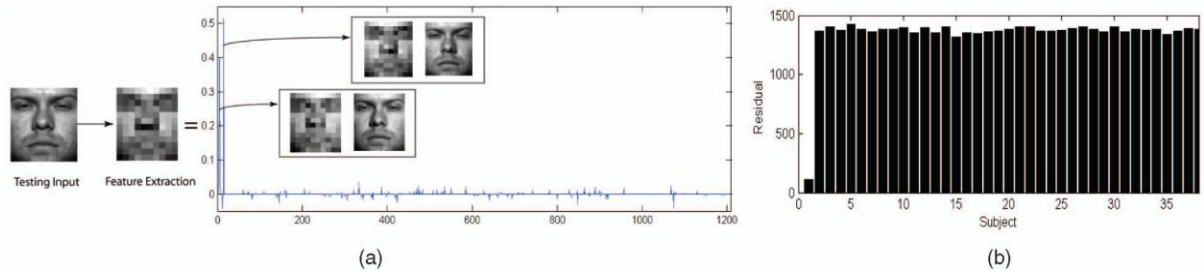


Figure 5.1: Demonstration of the idea of SRC applied to face recognition. (a) plot of the representation coefficients vs. training samples/dictionary and (b) plot of Residual vs. Subject.

Denote by $\mathbf{A}_i = [\mathbf{s}_{i,1}, \mathbf{s}_{i,2}, \dots, \mathbf{s}_{i,n_i}] \in \mathbb{R}^{m \times n_i}$ the set of training samples of the i -th object class, where m is the dimensionality of the object, and n_i is the number of training samples of the i -th class. For a test sample $\mathbf{y} \in \mathbb{R}^m$ from the same class, \mathbf{y} could be approximated by a linear combination of the samples within \mathbf{A}_i , i.e. $\mathbf{y} = \sum_{j=1}^{n_i} \alpha_{i,j} \mathbf{s}_{i,j} = \mathbf{A}_i \boldsymbol{\alpha}_i$, where $\boldsymbol{\alpha}_i = [\alpha_{i,1}, \alpha_{i,2}, \dots, \alpha_{i,n_i}]^T \in \mathbb{R}^{n_i}$ are the representation coefficients. Suppose that we have C object classes, and let $\mathbf{A} = [\mathbf{A}_1, \mathbf{A}_2, \dots, \mathbf{A}_C]$ be the concatenation of the n training samples from all the C classes, where $n = n_1 + n_2 + \dots + n_C$. In the ideal case, the linear representation of \mathbf{y} in terms of \mathbf{A} can be written as $\mathbf{y} = \mathbf{A}\boldsymbol{\alpha}$, where $\boldsymbol{\alpha} = [\boldsymbol{\alpha}_1, \boldsymbol{\alpha}_2, \dots, \boldsymbol{\alpha}_C] = [0, \dots, 0, \alpha_{i,1}, \alpha_{i,2}, \dots, \alpha_{i,n_i}, 0, \dots, 0]^T$ is a vector of coefficients whose entries are all zeros except those associated with the i -th class. To solve this, ideally we want to use l_0 -norm

minimization. However, in practice l_0 -norm non-convex optimization is difficult. Therefore, we use l_1 -norm minimization:

$$\hat{\boldsymbol{\alpha}} = \arg \min_{\boldsymbol{\alpha}} \{\|\mathbf{y} - \mathbf{A}\boldsymbol{\alpha}\|_2^2 + \lambda\|\boldsymbol{\alpha}\|_1\} \quad (5.1)$$

where λ is a positive scalar, we can obtain the real sparse coding vector $\hat{\boldsymbol{\alpha}}$ of \mathbf{y} over \mathbf{A} .

Denote by $\delta_i(\cdot) : \mathbb{R}^n \rightarrow \mathbb{R}^n$ the characteristic function which selects only the sparse coding coefficients associated with the class i . By reconstructing the object as $\mathbf{A}\delta_i(\hat{\boldsymbol{\alpha}})$, we can compute the reconstruction error associated with each class as:

$$r_i(\mathbf{y}) = \|\mathbf{y} - \mathbf{A}\delta_i(\hat{\boldsymbol{\alpha}})\|_2^2 \quad (5.2)$$

If \mathbf{y} belongs to the i -th class, we can expect that $r_i(\mathbf{y})$ should be minimum among all $r_i(\mathbf{y})$, $i = 1, 2, \dots, C$. Therefore, the classification is achieved by letting:

$$\text{identity}(\mathbf{y}) = \arg \min_i r_i(\mathbf{y}) \quad (5.3)$$

5.3 Dictionary and Centralized Dictionary Learning with SRC

In SRC the original training samples were used as the dictionary for sparse coding. However, the size of such a dictionary can be quite large, increasing the coding complexity. To solve this problem we propose to learn a more compact dictionary \mathbf{D} , from the training sample set \mathbf{A} , by solving the following minimization problem:

$$J_{\{\mathbf{D}, \mathbf{X}\}} = \arg \min_{\{\mathbf{D}, \mathbf{X}\}} \{\|\mathbf{A} - \mathbf{D}\mathbf{X}\|_F^2 + \lambda\|\mathbf{X}\|_1\} \quad (5.4)$$

where $\|\cdot\|_F$ and $\|\cdot\|_1$ are the Frobenius norm and l_1 -norm, \mathbf{X} is the representation coefficient matrix of \mathbf{A} over \mathbf{D} , and λ is a scalar to balance the F -norm and l_1 -norm terms. We require that each column of \mathbf{D} to be a unit vector.

(5.4) is a joint optimization problem of \mathbf{D} and \mathbf{X} , and it can be solved by alternatively optimizing \mathbf{D} and \mathbf{X} . From some initialization of \mathbf{D} , we can calculate \mathbf{X} by solving $\arg \min_{\{\mathbf{X}\}} \{\|\mathbf{A} - \mathbf{D}\mathbf{X}\|_F^2 + \lambda\|\mathbf{X}\|_1\}$ with some standard convex optimization algorithm [134]; then by fixing \mathbf{X} , \mathbf{D} can be easily updated by solving a l_2 -norm minimization problem $\arg \min_{\{\mathbf{D}\}} \{\|\mathbf{A} - \mathbf{D}\mathbf{X}\|_F^2\}$. With the updated dictionary \mathbf{D} , \mathbf{X} can then be renewed; the above procedures can be iteratively implemented until J in (5.4) converges. The convergence of such an alternative optimization is straightforward because in each iteration J can only decrease.

Combining this with SRC denote \mathbf{y} as a test sample. We can use \mathbf{D} to represent \mathbf{y} by solving the l_1 -norm minimization problem:

$$J_{\alpha} = \arg \min_{\alpha} \{\|\mathbf{y} - \mathbf{D}\alpha\|_2^2 + \lambda\|\alpha\|_1\} \quad (5.5)$$

where α is the sparse representation coefficient vector of \mathbf{y} over \mathbf{D} , and λ is a constant. Once α is solved using convex optimization like in [133], we can calculate the reconstruction error (5.2), and subsequently classify \mathbf{y} (5.3).

Dictionary Learning with SRC solved the problem of using large dictionaries. However, this method can be further improved by introducing a class discrimination term into the DL model. For the new DL process, we not only minimize the reconstruction error but also minimize the variance of the sparse coding coefficients. In this way the learnt dictionary aims to represent the test sample (in question) from the same class (to its training samples) to be as close to its class center as possible. This is Centralized Dictionary Learning and is accomplished by adding a class discrimination term to the DL model. The discrimination term is based on the Fisher discriminate criterion [135] and is imposed on \mathbf{X} , in the case of the training dataset \mathbf{A} . Based on the Fisher criterion, a good classifier or dimensionality reduction method should make the samples have small within-class scatter and large between-class scatter. From a statistical sense, the samples should be close to its corresponding class center. The CDL model of the learnt dictionary \mathbf{D} is as follows:

$$J_{\{\mathbf{D}, \mathbf{X}\}} = \arg \min_{\{\mathbf{D}, \mathbf{X}\}} \{\|\mathbf{A} - \mathbf{D}\mathbf{X}\|_F^2 + \lambda_1\|\mathbf{X}\|_1 + \lambda_2 F(\mathbf{X})\} \quad (5.6)$$

where λ_1 and λ_2 are positive scalars and $F(\mathbf{X})$ is the Fisher discriminate term. By removing the between-class scatter term to make the minimization convex, (5.6) becomes:

$$J_{\{\mathbf{D}, \mathbf{X}\}} = \arg \min_{\{\mathbf{D}, \mathbf{X}\}} \{\|\mathbf{A} - \mathbf{D}\mathbf{X}\|_F^2 + \lambda_1\|\mathbf{X}\|_1 + \lambda_2\|\boldsymbol{\chi} - \boldsymbol{\mu}_{\mathbf{X}}\|_2^2\} \quad (5.7)$$

where $\boldsymbol{\mu}_{\mathbf{X}}$ is the mean coding coefficients of $\boldsymbol{\chi}$, the elements of \mathbf{X} . This last term, $\|\boldsymbol{\chi} - \boldsymbol{\mu}_{\mathbf{X}}\|_2^2$ makes the coding coefficients $\boldsymbol{\chi}$ be as close to its center $\boldsymbol{\mu}_{\mathbf{X}}$ as possible.

Procedures for SRC after learning \mathbf{D} with CDL remain unchanged to what was described above for the DL model. In addition to the reconstruction error (5.2), it is expected that if the test sample \mathbf{y} is from class i , its sparse coding coefficients over \mathbf{D}_i should be close to $\boldsymbol{\mu}_i$. This is measured by the distance from $\delta_i(\hat{\alpha})$ to $\boldsymbol{\mu}_i$, denoted by:

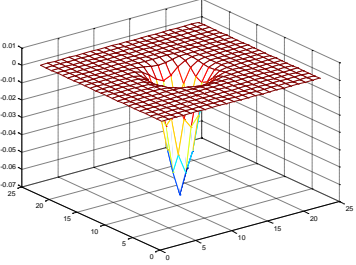

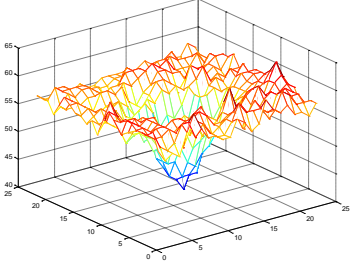

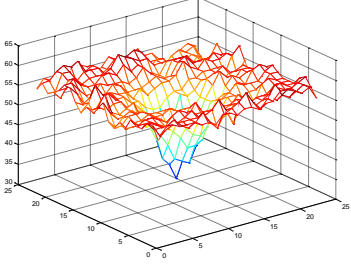
$$d_i(\mathbf{y}) = \|\delta_i(\hat{\alpha}) - \boldsymbol{\mu}_i\|_2^2 \quad (5.8)$$

Then with the fusing of $r_i(\mathbf{y})$ and $d_i(\mathbf{y})$, the class label of \mathbf{y} can be determined as:

$$\text{identity}(\mathbf{y}) = \arg \min_i f(r_i(\mathbf{y}) + d_i(\mathbf{y})) \quad (5.9)$$

where $f(\cdot)$ is a fusion function.

Table 5.1: Gaussian function with sigma equal to 1.5 compared with two MAs. Using (4.2) the maximum coefficient values of the two MAs are 0.7342 and 0.8132.

Sigma of 1.5	MA	Mesh plot of MA	Max. coefficient
			0.7342
			0.8132

5.4 DL and CDL with SRC at MA Detection

As mentioned in the Introduction, this is a two step method. The first step is to extract all possible MA candidates from a fundus image using MSCF (coarse level). Details of MSCF are provided in Chapter 4 but a brief summary with figures using another database are presented below. In the second step, MA and non-MA dictionaries are learnt and used to classify candidates determined in step one.

The idea of MSCF is to detect MAs of different dimensions. As an example, the first column of Table 5.1 depicts a Gaussian function with sigma value 1.5 applied to two MAs extracted from the DIARETDB1 dataset (explained further in the next section). Using the correlation coefficient function (4.2) the maximum coefficient of each MA is displayed in the last column. Since both

coefficients are relatively high it means the correct sigma was chosen. Applying MSCF to an entire retinal image, we first compute the MSCF responses at each scale value and then combine them to form the final response. Fig. 5.2 (b) shows the final response of (a). This response is then thresholded to remove low coefficient pixels before the vessels are also removed (see Fig. 5.3 (a)). The final step is to perform region growing on the remaining objects shown in Fig. 5.3 (b).

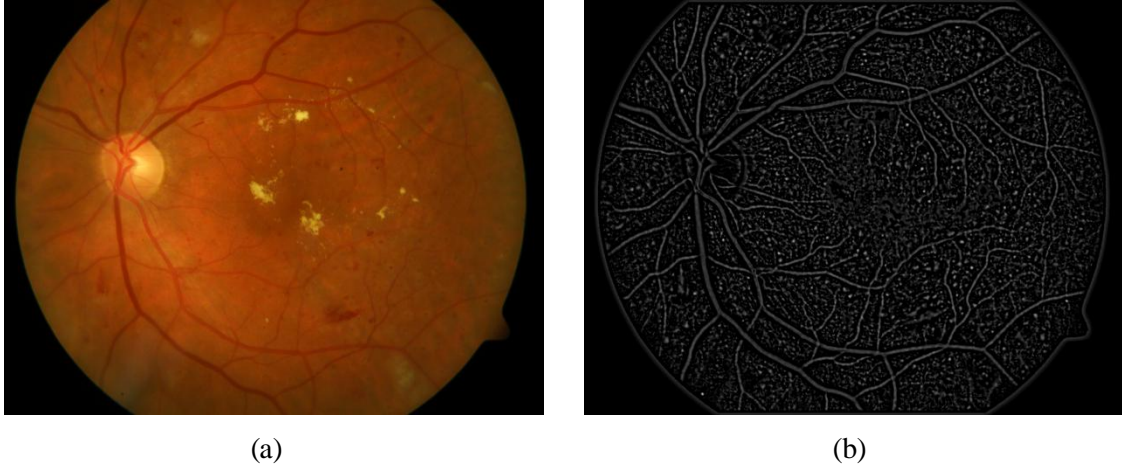


Figure 5.2: (a) A fundus image from the DIARETDB1 dataset and (b) its final response after Multi-scale Correlation Filtering.

MA detection can be thought of as a two-class classification problem: MA and non-MA. Therefore, we find two sub-dictionaries for SRC: the MA dictionary and the non-MA dictionary. In the ROC training dataset [132], there are $n = 336$ manually marked MA. We can take the detected candidates not marked as MA as the non-MA structures, whose amount is $m = 7794$. For DIARETDB1 n and m are 284 and 16739 respectively. Let $\mathbf{A} = [\mathbf{a}_1, \mathbf{a}_2, \dots, \mathbf{a}_n]$ and $\mathbf{B} = [\mathbf{b}_1, \mathbf{b}_2, \dots, \mathbf{b}_m]$, where \mathbf{a}_i , $i = 1, 2, \dots, n$, and \mathbf{b}_j , $j = 1, 2, \dots, m$, are 121×1 column vectors containing the pixel values from an 11×11 window that covers a MA or a non-MA object at its center. The columns of \mathbf{A} and \mathbf{B} are normalized to have unit l_2 -norm. The left column of Fig. 5.4 shows a MA and a non-MA object in its 11×11 window from ROC training. In the middle column the object's pixel intensity is given followed by its 121×1 column vector shown in the last column. An example of a MA and a non-MA object from DIARETDB1 to illustrate this procedure is given in Fig. 5.5. Tables 5.2 and 5.3 show

samples from the unlearned MA (\mathbf{A}) and non-MA (\mathbf{B}) dictionaries of the ROC training dataset. Corresponding samples from the DIARETDB1 unlearned dictionaries are found in Table 5.4 and 5.5.

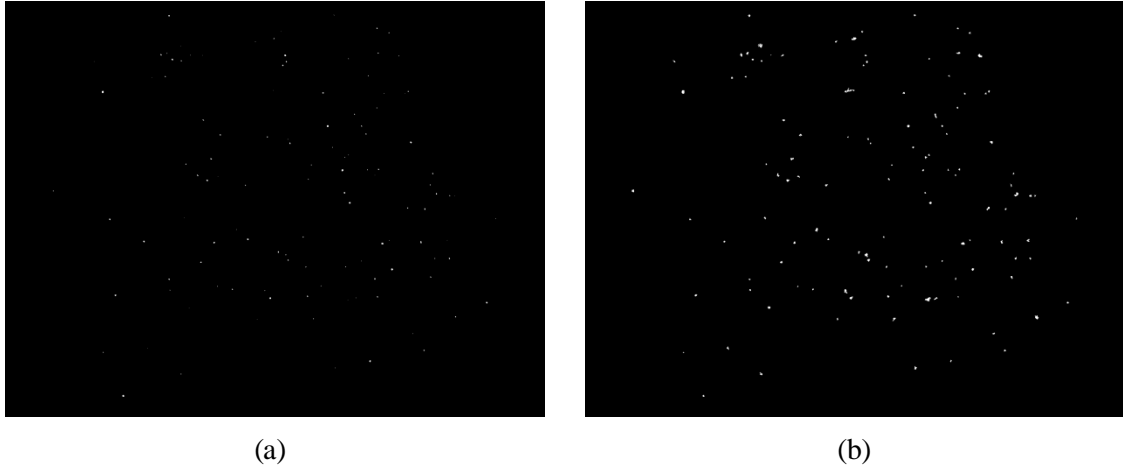


Figure 5.3: (a) Result after thresholding and vessel removal; (b) region growing applied to (a).

From the initial step we learn two much more compact dictionaries from \mathbf{A} and \mathbf{B} . By taking \mathbf{A} as the training dataset, we learn a compact MA dictionary Φ using (5.4) shown in Tables 5.6 and 5.8. Similarly, for the non-MA training dataset \mathbf{B} , we can train a compact dictionary Ψ illustrated in Tables 5.7 and 5.9. In our experiment, the size of both Φ and Ψ are 121×20 , and we let $\mathbf{D} = [\Phi, \Psi]$. As an example for visual illustration we show the learnt dictionaries of Φ and Ψ in its 11×11 windows in Figs. 5.6 and 5.7 respectively. For each MA candidate vector denoted by \mathbf{y} , we use \mathbf{D} to represent it by solving the l_1 -norm minimization problem with (5.5). Since $\mathbf{D} = [\Phi, \Psi]$, we let $\alpha = [\alpha_\phi, \alpha_\psi]$ (from the result of (5.5)), where α_ϕ is the representation of \mathbf{y} over Φ and α_ψ is the representation of \mathbf{y} over Ψ .

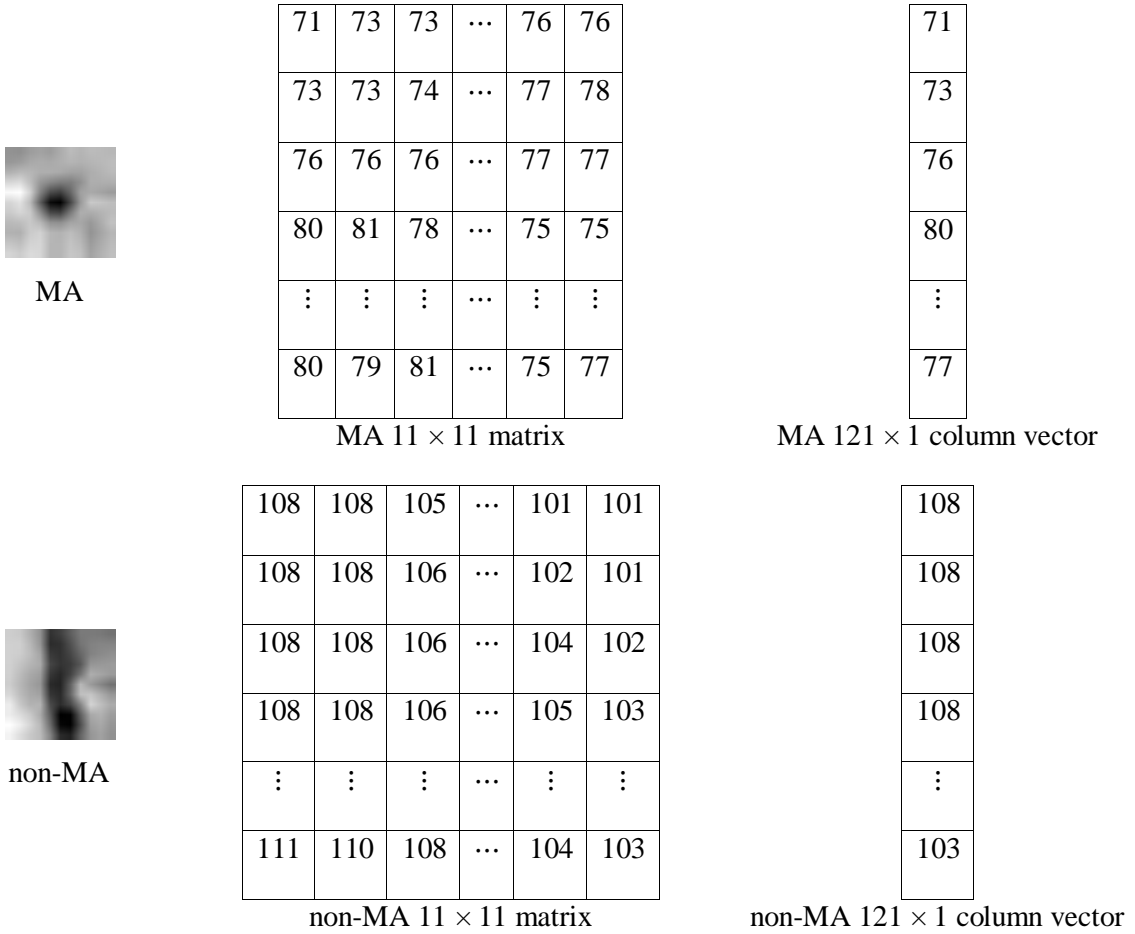


Figure 5.4: Using an example of a MA (top) and a non-MA (bottom) from ROC training, the procedure of extracting the object and converting it into a 121×1 column vector is shown.

Table 5.2: ROC training unlearned MA dictionary (**A**), dimensions of 121×336 .

	1	2	3	4	...	334	335	336
1	0.8315	0.3915	0.7885	-1.0312	...	0.9131	-0.1302	0.9473
2	1.1012	-0.2885	0.7885	-0.8076	...	1.6123	-0.3803	-0.2176
3	1.3709	-0.9685	0.7885	-0.3593	...	0.9131	-0.1302	0.7143
4	1.3709	-1.1952	0.5666	0.0889	...	0.2138	-0.1302	1.6462
⋮	⋮	⋮	⋮	⋮	...	⋮	⋮	⋮
119	0.0223	1.5249	-1.2084	1.2095	...	0.2138	0.3700	0.2484
120	1.1012	2.3182	-1.4303	1.2095	...	0.4469	0.3700	-0.2176
121	1.3709	2.2049	-1.2084	0.9854	...	0.6800	1.3705	-0.4505

Table 5.3: ROC training unlearned non-MA dictionary (**B**), dimensions of 121×7794 .

	1	2	3	4	...	7792	7793	7794
1	1.0961	0.0135	-0.1424	-0.3407	...	0.9840	0.0562	0.4997
2	1.0961	0.0135	0.2241	0.0933	...	0.4453	0.9424	1.1606
3	1.0961	0.0135	-0.8754	2.2632	...	1.5228	1.2378	1.1606
4	1.0961	0.0135	0.2241	2.2632	...	0.7146	1.2378	0.1693
⋮	⋮	⋮	⋮	⋮	...	⋮	⋮	⋮
119	0.1107	-0.5318	0.2241	0.5273	...	0.1759	2.124	1.8214
120	0.1107	-0.5318	-0.5089	0.0933	...	0.4453	1.829	-0.1611
121	0.1107	-0.5318	-0.1424	-0.3407	...	0.7146	1.238	0.4997

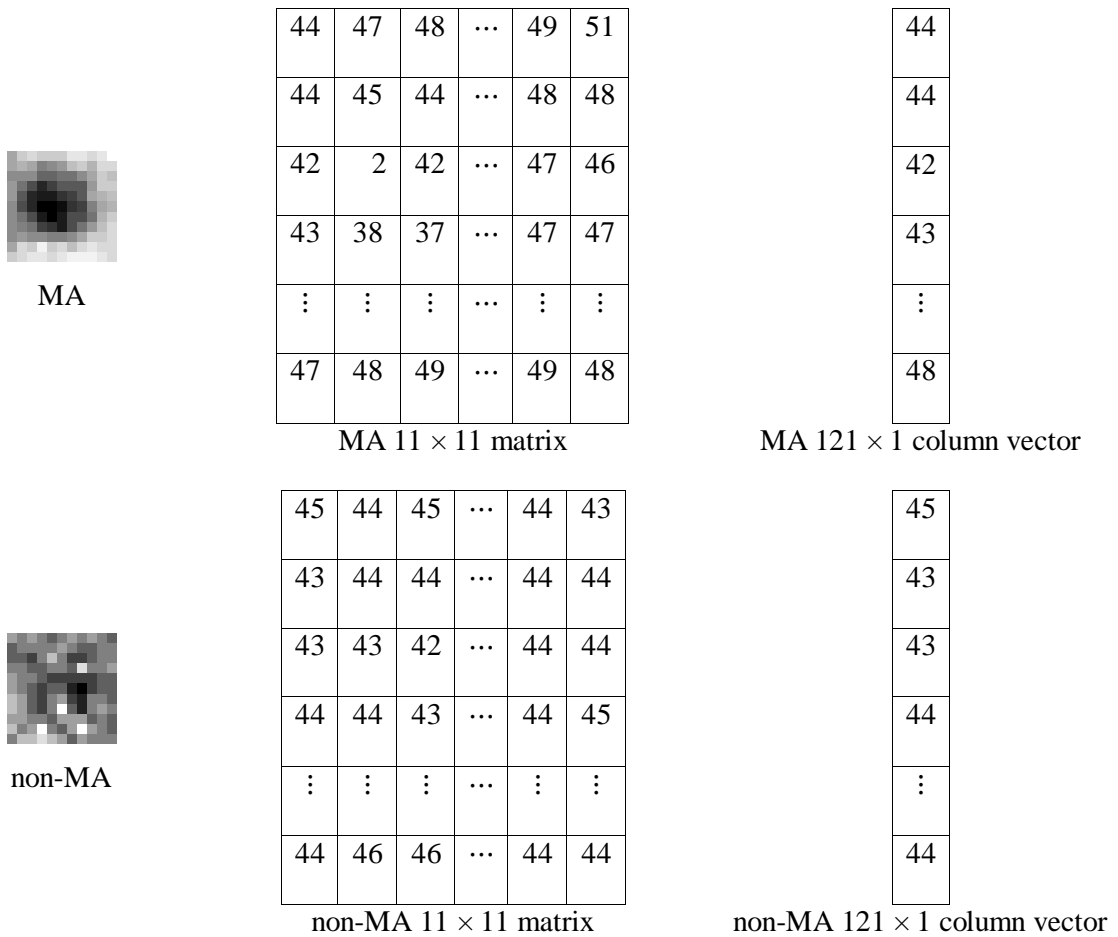


Figure 5.5: Using an example of a MA (top) and a non-MA (bottom) from DIARETDB1, the procedure of extracting the object and converting it into a 121×1 column vector is demonstrated.

Table 5.4: DIARETDB1 unlearned MA dictionary (\mathbf{A}), dimensions of 121×284 .

	1	2	3	4	...	282	283	284
1	0.0980	0.0964	0.1087	0.0937	...	0.0975	0.0906	0.0988
2	0.0928	0.0947	0.0994	0.0937	...	0.1015	0.0853	0.1108
3	0.0911	0.0895	0.0899	0.0937	...	0.1015	0.0853	0.1138
4	0.0928	0.0878	0.0876	0.0898	...	0.0812	0.0746	0.1048
⋮	⋮	⋮	⋮	⋮	...	⋮	⋮	⋮
119	0.0894	0.1033	0.1041	0.1016	...	0.0893	0.0959	0.1018
120	0.0946	0.1016	0.1089	0.0996	...	0.0975	0.0959	0.0928
121	0.0911	0.0981	0.1041	0.0976	...	0.1218	0.0959	0.0899

Table 5.5: DIARETDB1 unlearned MA dictionary (\mathbf{B}), dimensions of 121×16739 .

	1	2	3	4	...	16737	16738	16739
1	0.0954	0.0839	0.0917	0.0937	...	0.0972	0.0832	0.1096
2	0.0904	0.0867	0.0917	0.0888	...	0.0972	0.0884	0.0939
3	0.0879	0.0867	0.0917	0.0913	...	0.1023	0.0936	0.0835
4	0.0904	0.0951	0.0917	0.0938	...	0.0921	0.0936	0.0991
⋮	⋮	⋮	⋮	⋮	...	⋮	⋮	⋮
119	0.0929	0.0951	0.0917	0.0913	...	0.0921	0.1040	0.0887
120	0.0929	0.0923	0.0895	0.0937	...	0.0921	0.0988	0.0991
121	0.0854	0.0867	0.0895	0.0888	...	0.0921	0.0936	0.0887

Table 5.6: ROC training learnt MA dictionary (Φ), dimensions 121×20 .

	1	2	3	4	...	18	19	20
1	0.0745	0.0636	0.0351	0.0990	...	-0.0763	-0.1383	-0.0900
2	0.0745	0.0846	0.0596	0.0224	...	-0.0336	-0.1708	-0.1004
3	0.0745	0.1316	0.0705	0.1372	...	-0.0576	-0.1724	-0.1062
4	0.0745	0.1045	0.0301	0.1372	...	-0.1718	-0.1124	-0.0977
⋮	⋮	⋮	⋮	⋮	...	⋮	⋮	⋮
119	0.0745	-0.1461	0.0104	0.0224	...	0.0634	0.0986	0.0392
120	0.0745	-0.1249	-0.0547	-0.0541	...	0.0677	0.1005	0.0394
121	0.0745	-0.0959	-0.1231	-0.0541	...	0.0650	0.0993	-0.0072

Table 5.7: ROC training learnt non-MA dictionary (Ψ), dimensions 121×20 .

	1	2	3	4	...	18	19	20
1	-0.0675	0.0731	-0.0552	0.0321	...	-0.0356	-0.0126	0.1039
2	-0.0645	0.0790	-0.0997	0.0186	...	0.0023	-0.0173	0.0956
3	-0.0656	0.0803	-0.1323	-0.0062	...	0.0553	-0.0056	0.0890
4	-0.0711	0.0814	-0.1254	-0.0443	...	0.0709	0.0196	0.0415
⋮	⋮	⋮	⋮	⋮	...	⋮	⋮	⋮
119	-0.0824	0.0884	0.0603	-0.0117	...	0.0344	0.0630	0.0390
120	-0.0736	0.0380	0.0033	0.0037	...	0.0437	0.0944	0.0585
121	-0.0590	-0.01837	-0.0271	0.0007	...	0.0167	0.1021	0.0675

Table 5.8: DIARETDB1 learnt MA dictionary (Φ), dimensions 121×20 .

	1	2	3	4	...	18	19	20
1	-0.0578	-0.1371	0.0519	-0.0073	...	0.1226	0.0512	-0.0492
2	-0.0664	-0.1381	0.0494	-0.0032	...	0.0977	-0.0261	-0.0483
3	-0.0786	-0.0937	0.0595	-0.0162	...	0.01513	-0.0441	-0.0199
4	-0.0830	-0.0455	0.0180	0.0207	...	-0.0678	-0.1056	-0.0292
⋮	⋮	⋮	⋮	⋮	...	⋮	⋮	⋮
119	0.1452	-0.0237	0.1401	0.0992	...	0.0656	0.0868	0.0536
120	0.1258	-0.0183	0.1168	0.1252	...	0.1469	0.0220	0.0262
121	0.1316	-0.0220	0.0926	0.1459	...	0.1331	0.0624	-0.0705

Table 5.9: DIARETDB1 learnt non-MA dictionary (Ψ), dimensions 121×20 .

	1	2	3	4	...	18	19	20
1	0.2195	0.1082	-0.1688	-0.0415	...	0.0534	-0.0487	-0.0291
2	0.2162	0.0778	-0.1484	-0.0508	...	0.0468	-0.0693	-0.0415
3	0.1899	0.0472	-0.1242	-0.0573	...	0.0445	-0.0926	-0.0371
4	0.1508	0.0024	-0.1071	-0.0466	...	0.0361	-0.1107	-0.0289
⋮	⋮	⋮	⋮	⋮	...	⋮	⋮	⋮
119	0.0679	-0.0332	-0.0181	-0.0115	...	-0.0095	-0.1294	0.1039
120	0.0872	0.0238	-0.0409	-0.0175	...	-0.0133	-0.1133	0.1352
121	0.1081	0.0753	-0.0543	-0.0370	...	-0.0186	-0.0952	0.1396

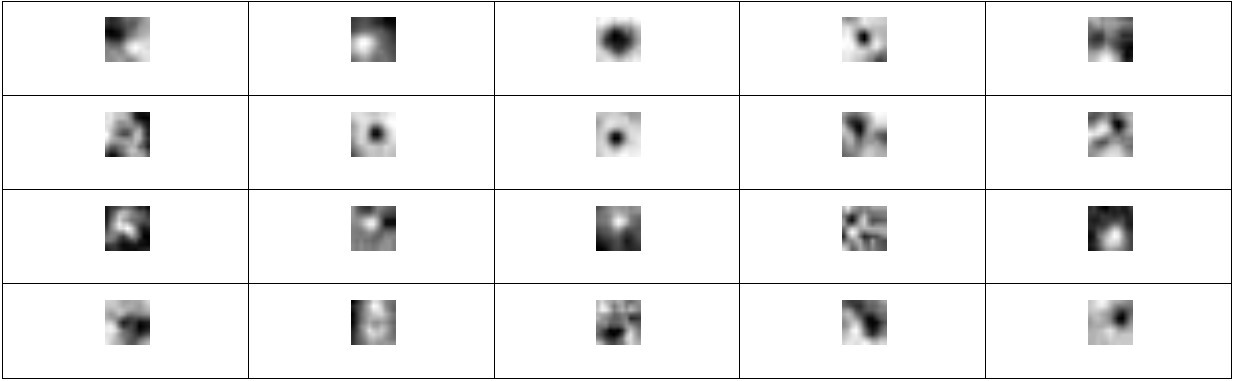


Figure 5.6: Example of a learnt MA dictionary with 20 samples.

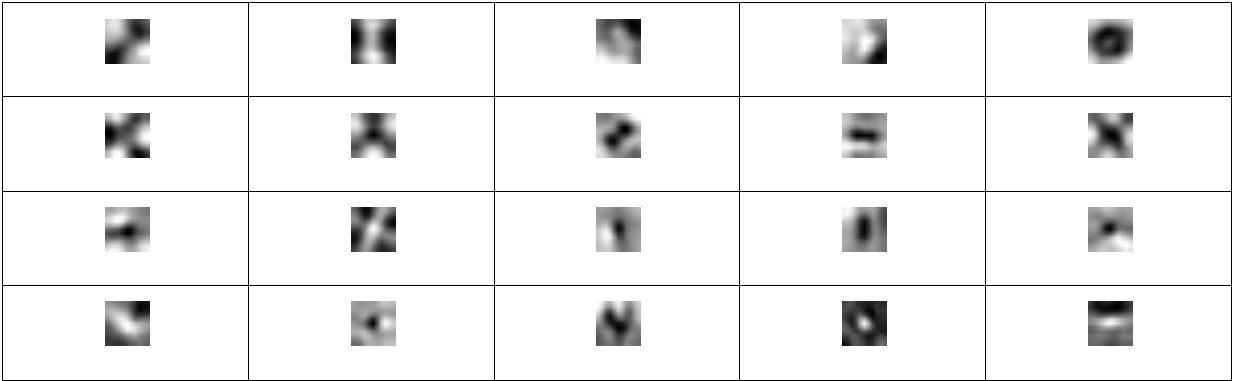


Figure 5.7: Example of a learnt non-MA dictionary with 20 samples.

Using the learnt MA dictionary Φ and the associated coefficients α_ϕ to reconstruct \mathbf{y} , the reconstruction error will be $r_{MA}(\mathbf{y}) = \|\mathbf{y} - \Phi\alpha_\phi\|_2^2$, and if we use Ψ and α_ψ to reconstruct \mathbf{y} , the reconstruction error will be $r_{NMA}(\mathbf{y}) = \|\mathbf{y} - \Psi\alpha_\psi\|_2^2$. Intuitively, if the candidate object \mathbf{y} is a MA, it could be well represented by Φ so that the error r_{MA} will be small. If \mathbf{y} is not a MA object, r_{MA} will be large, while the reconstruction error r_{NMA} will be small. Therefore, the magnitude of r_{MA} and r_{NMA} can reflect the membership of \mathbf{y} . We use the following rule to classify \mathbf{y} :

$$\begin{cases} \mathbf{y} \text{ is a MA} & \text{if } r_{MA} \leq r_{NMA} \\ \mathbf{y} \text{ is not a MA} & \text{if } r_{MA} > r_{NMA} \end{cases} \quad (5.10)$$

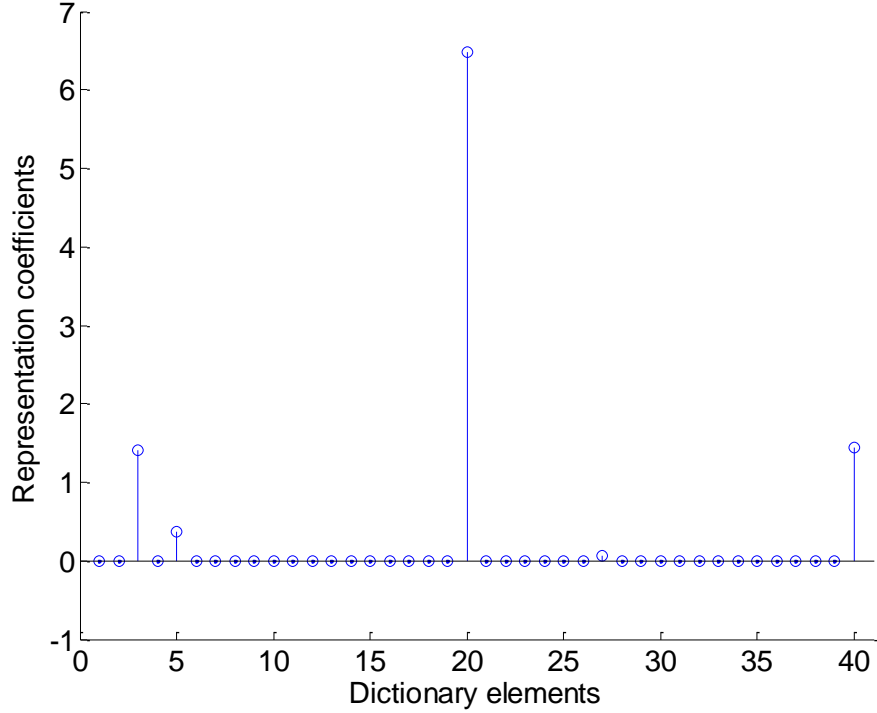


Figure 5.8: Plot of the representation coefficients vs. dictionary elements where 1-20 are MA elements and 21-40 are non-MA elements. Since the most significant coefficient is between 1-20, the candidate is most likely a MA object.

In CDL with SRC we also use \mathbf{A} and \mathbf{B} to learn compact dictionaries Φ and Ψ , this time using (5.6). Along with Φ and Ψ whose size are 121×20 , we have μ_ϕ and μ_ψ (from 5.7) representing the mean coding coefficients of Φ and Ψ in that order. Similar to what was described above, we let $\mathbf{D} = [\Phi, \Psi]$. The following steps to find $\alpha = [\alpha_\phi, \alpha_\psi]$ are the same to what was depicted before. The only addition is calculating $d_\phi(\mathbf{y}) = \|\alpha_\phi - \mu_\phi\|_2^2$ and $d_\psi(\mathbf{y}) = \|\alpha_\psi - \mu_\psi\|_2^2$, the distance from α_ϕ and α_ψ to their respective centers (i.e. μ_ϕ or μ_ψ). Fusing this with the reconstruction errors of r_{MA} and r_{NMA} , we have the following rule to determine the class of \mathbf{y} for CDL:

$$\begin{cases} \mathbf{y} \text{ is a MA} & \text{if } r_{MA} + d_\phi \leq r_{NMA} + d_\psi \\ \mathbf{y} \text{ is not a MA} & \text{if } r_{MA} + d_\phi > r_{NMA} + d_\psi \end{cases} \quad (5.11)$$

Fig. 5.8 plots the representation coefficients vs. dictionary samples for a MA candidate. Dictionary samples from 1-20 are MA while 21-40 are non-MA. Since the most significant coefficient is in 1-20,

the likelihood of the candidate is a MA. The representation coefficients of both α_ϕ and α_ψ along with its μ_ϕ and μ_ψ from Fig. 5.8 are shown in Table 5.10. If we were to calculate $d_\phi(\mathbf{y})$ and $d_\psi(\mathbf{y})$ its results would be 1.957 and 3.9599 respectively, more evidence that is \mathbf{y} a MA. Fig. 5.9 and Table 5.11 illustrate another example, this time with a non-MA candidate. The highest peak in Fig. 5.9 occurs in the dictionary elements 21-40. $d_\phi(\mathbf{y})$ and $d_\psi(\mathbf{y})$ can be calculated from Table 5.11 to be 5.6908 and 3.0874. Because $d_\psi(\mathbf{y})$ is lower, \mathbf{y} is closer to the mean coefficients of Ψ , the non-MA class. Fig. 5.10 depicts putting everything together using (5.11) to detect a MA.

Table 5.10: MA and non-MA representation coefficients from Fig. 5.8 compared with its corresponding class mean coefficients.

MA rep. coeff. (α_ϕ)	non-MA rep. coeff. (α_ψ)	MA mean coeff. (μ_ϕ)	non-MA mean coeff. (μ_ψ)
8.6482e-16	-9.2582e-16	0.2360	0.1492
-7.7020e-16	1.1068e-14	0.0123	0.1081
1.4140	-2.8226e-16	1.3653	-0.5505
-2.2407e-14	-4.5172e-15	-1.2119	-0.0583
⋮	⋮	⋮	⋮
-4.4482e-16	2.6677e-17	-0.1109	-0.4850
-3.6651e-16	-6.1872e-17	0.0664	-0.0337
6.4733	1.4407	5.3143	5.1653

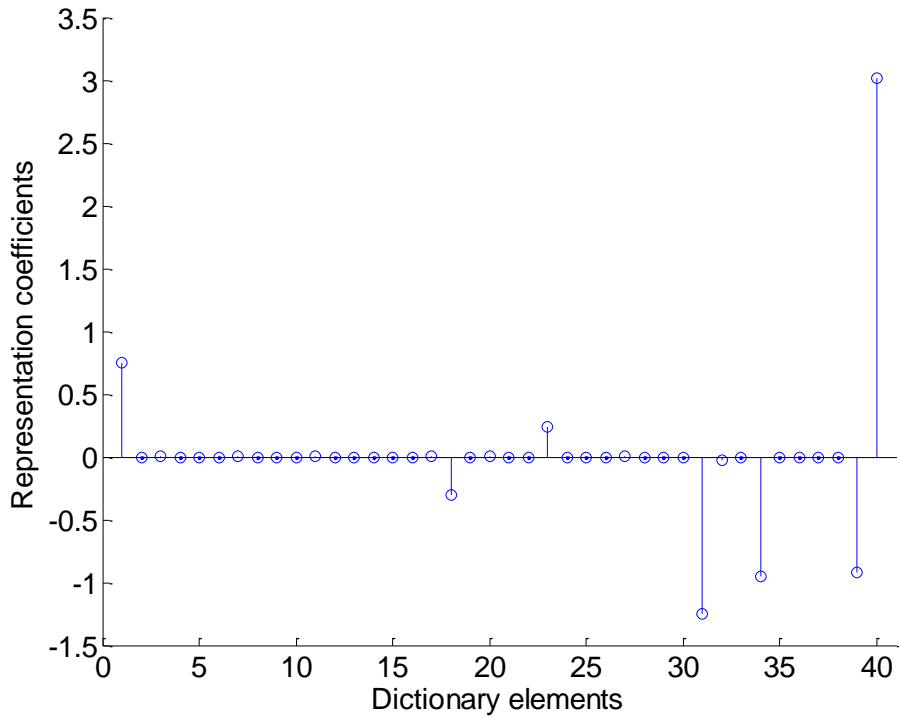


Figure 5.9: Plot of the representation coefficients vs. dictionary elements where 1-20 are MA elements and 21-40 are non-MA elements. Since the most significant coefficient is between 21-40, the candidate is most likely a non-MA object.

5.5 Experimental Results

A series of experiments were conducted on two public databases, ROC competition website [132] and DIARETDB1 (Standard Diabetic Retinopathy Database) [136], [137]. The dictionary learning parameters λ_1 and λ_2 in (5.6) were set as 0.001 and 0.01 respectively for ROC, while for DIARETDB1 $\lambda_1 = 0.1$ and $\lambda_2 = 0.001$. In the case of λ (5.5), the value of 3 was applied uniformly throughout all experiments.

For the ROC training database 50 images were used with 20 in learning the MA and non-MA dictionaries, and 30 for testing. More information about ROC can be found in Chapter 4. In total there were 163 MAs in the 30 test images.

Table 5.11: MA and non-MA representation coefficients from Fig. 5.9 compared with its corresponding class mean coefficients.

MA rep. coeff. (α_ϕ)	non-MA rep. coeff. (α_ψ)	MA mean coeff. (μ_ϕ)	non-MA mean coeff. (μ_ψ)
0.7460	-9.3671e-16	0.2360	0.1492
-7.8905e-17	-1.6544e-16	0.0123	0.1081
8.3397e-16	0.2393	1.3653	-0.5505
-5.2631e-15	3.9624e-16	-1.2119	-0.0583
⋮	⋮	⋮	⋮
-0.3049	-2.6908e-16	-0.1109	-0.4850
-5.7576e-16	-0.9196	0.0664	-0.0337
1.5245e-15	3.0212	5.3143	5.1653

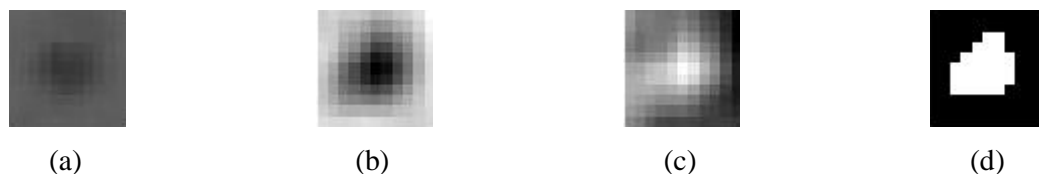


Figure 5.10: Example of CDL with SRC based MA detection. (a) is a cropped MA object; (b) is its fusion $r_{MA} + d_\phi$ and (c) is $r_{NMA} + d_\psi$; (d) is the detected result by applying the rule in (5.11). We see that the MA object is well detected.

Evaluation of the performance was based on plotting sensitivity against the average number of false positives per image (FROC), shown in Fig. 5.11. To refresh, sensitivity is the number of MA correctly detected while false positive is the number of non-MA detected as MA. The proposed methods are compared to Math Morph [17], [24] and the Candidate Detection method [17], [24], [138], [139], which consists of shade correction, morphological top hat transform and region growing operations. Shade correction normalizes the image with the help of a median filter. Retinal blood vessels are eliminated with top hat transform and region growing is applied to the remaining

candidates after the previous operations. Math Morph [17], [24] was implemented by us. We were not able to compare the fusion algorithm in [24] because the pixels in ROC were not marked, a prerequisite of this method.

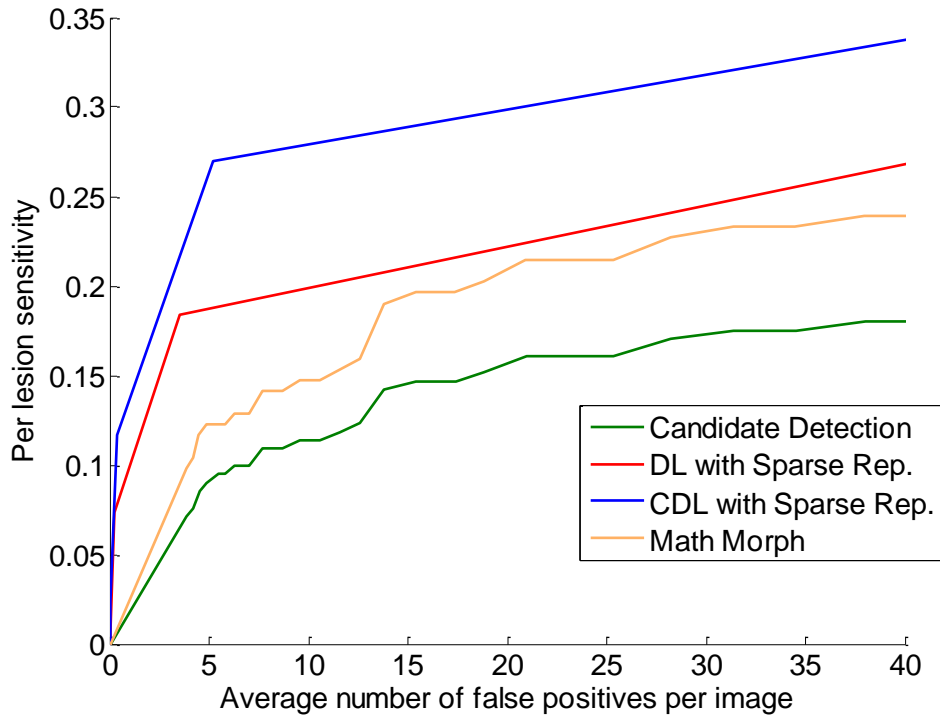


Figure 5.11: FROC curves of the proposed methods in comparison with Candidate Detection and Math Morph using 30 test images from ROC.

As can be seen from Fig. 5.11, for the same false positive value CDL with SRC has a higher sensitivity compared to the other algorithms. This is made clear in Table 5.12 which lists the sensitivities of 1, 1.5, 2, 4, 8 and 16 false positives per image of all methods derived from Fig. 5.11. In this table CDL with SRC has a greater sensitivity from 1 to 16 with the average being 0.2085, followed by DL with SRC – 0.1565 and Math Morph – 0.0922. Candidate Detection gives the worst perform of 0.0686 as shown in Fig. 5.11 and Table 5.12.

The performance evaluation of our proposed methods was further conducted on another well established public database DIARETDB1 [136], [137]. DIARETDB1 offers a general platform and a powerful testing toolkit with 89 images taken under a common imaging protocol to benchmark

diabetic retinopathy features. Collected at Kuopio University Hospital with the same 50° FOV digital camera, the images are all 1500×1152 pixels in size. Ground truth images of MA were marked by medical experts at a confidence level of 75% in accordance with guidelines set by DIARETDB1. Of the 89 images 76 were used, split into 28 for training and 48 for testing. From those 48 test images 169 MAs exist.

Table 5.12: Average sensitivity of different algorithms at various false positive points for the 30 ROC test dataset.

FPS/scan	1	1.5	2	4	8	16	Avg.
Candidate Detection	0.0184	0.0274	0.0369	0.0726	0.1088	0.1476	0.0686
Math Morph	0.0256	0.0384	0.0505	0.1009	0.1412	0.1963	0.0922
DL with SRC	0.0992	0.1157	0.1327	0.1846	0.1941	0.2125	0.1565
CDL with SRC	0.1356	0.1516	0.1673	0.2312	0.2748	0.2906	0.2085

Table 5.13: Average sensitivity of different algorithms at various false positive points for the DIARETDB1 test dataset.

FPS/scan	1	1.5	2	4	8	16	Avg.
Candidate Detection	0.0203	0.0405	0.0608	0.1829	0.3610	0.4867	0.1920
DL with SRC	0.0203	0.0405	0.0608	0.1876	0.3644	0.4929	0.1944
CDL with SRC	0.0203	0.0405	0.0608	0.1913	0.3677	0.5019	0.1971

Fig. 5.12 depicts the performance of the proposed methods, DL and CDL with SRC, and Candidate Detection at DIARETDB1 using FROC plots. Similar to Fig. 5.11 the proposed methods have a steeper gradient which lead to higher sensitivities for the same false positive values. Table 5.13 shows the sensitivities of 1, 1.5, 2, 4, 8 and 16 false positives per image from Fig. 5.12. From 1 to 2 the results of all three methods are the same. Afterwards, CDL with SRC begins to increase faster than DL with SRC, and Candidate Detection. The average of all algorithms listed in the last column of Table 5.13 are 0.1971 – CDL with SRC, 0.1944 – DL with SRC, and 0.1920 – Candidate Detection.

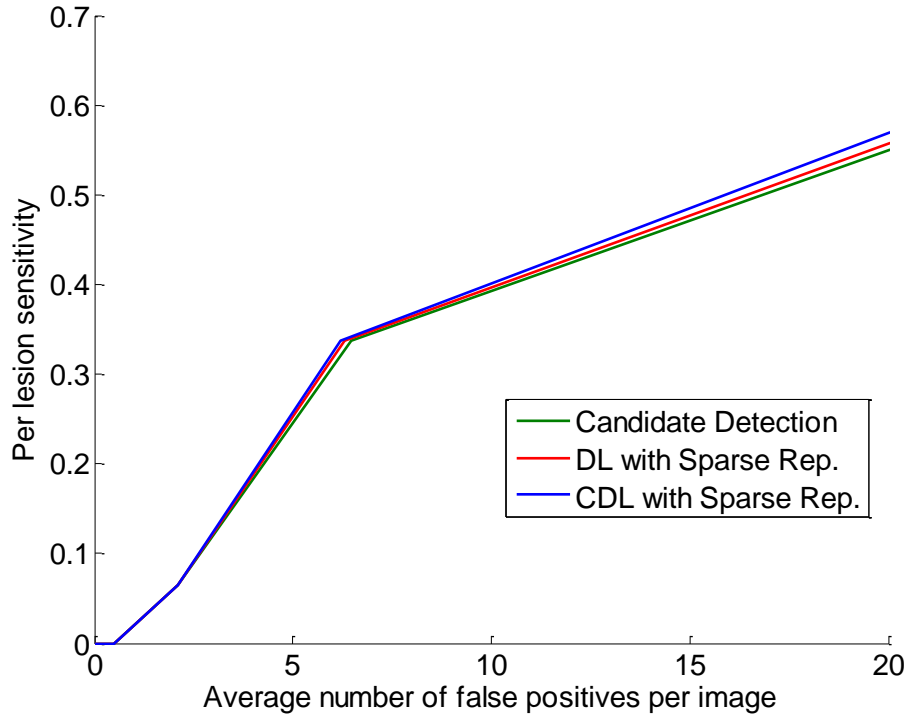


Figure 5.12: FROC curves of the proposed methods in comparison with Candidate Detection using DIARETDB1 test images.

Justification for selecting λ_1 and λ_2 in (5.6) to be 0.001 and 0.01 for ROC training; $\lambda_1 = 0.1$ and $\lambda_2 = 0.001$ for DIARETDB1 is given in Figs. 5.13 and 5.14. In each case the red FROC curve represents the selected lambda parameters which outperform other values. As for λ (5.5) equal to 3, Fig. 5.15 illustrates its red FROC curve achieving a better sensitivity than the other lambda curves.

The experimental results demonstrate in general that CDL with SRC outperforms DL with SRC at MA detection. The ROC dataset consisted of images captured with varying devices under different conditions. DIARETDB1 on the other hand contained images captured using a single device and unified image format. Since images in DIARETDB1 are uncompressed compared to ROC, the MAs are more visible. This means the detection result in DIARETDB1 is higher than ROC when comparing their sensitivities from 8 false positives onwards. We did not customize or tune any parameters due to this difference since our proposed methods are based on matching Multi-scale Gaussian kernels defined beforehand irrespective of image quality and resolution. The result of ROC

using CDL with SRC demonstrates the robustness of our proposed method in dealing with images of lower quality as we obtained a higher sensitivity compared to the rest.

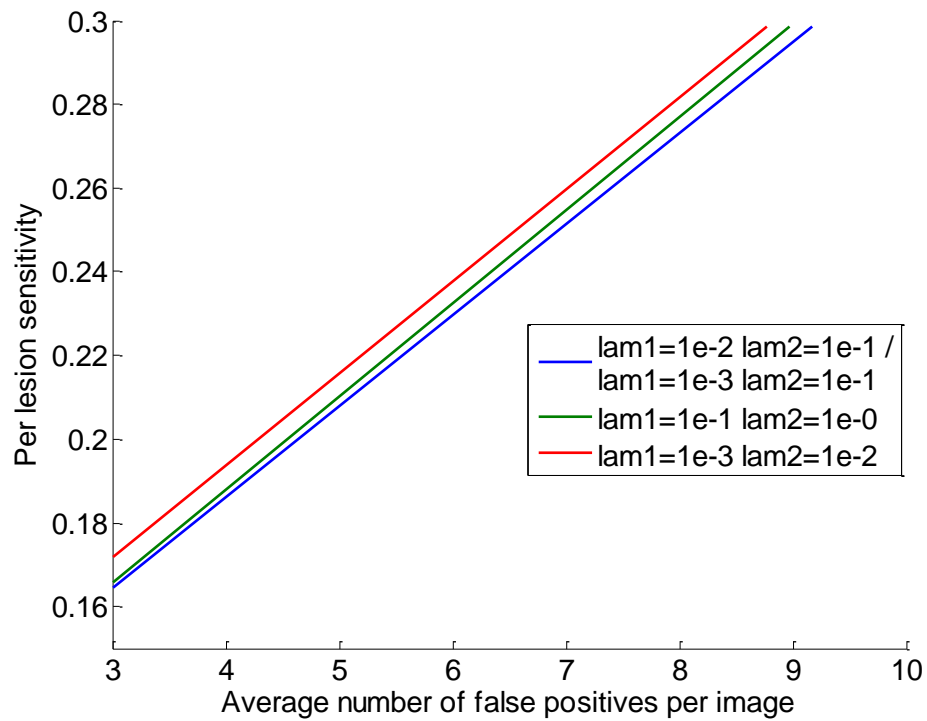


Figure 5.13: ROC training FROC curves of CDL with SRC comparing the use of various λ_1 and λ_2 values.

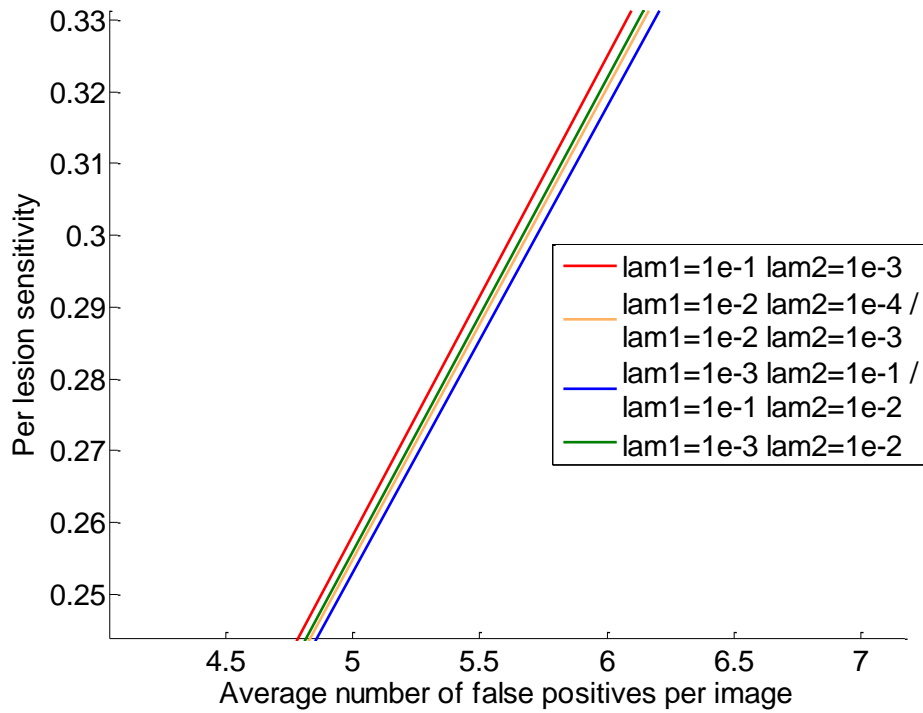


Figure 5.14: DIARETDB1 FROC curves of CDL with SRC evaluating the use of various λ_1 and λ_2 values.

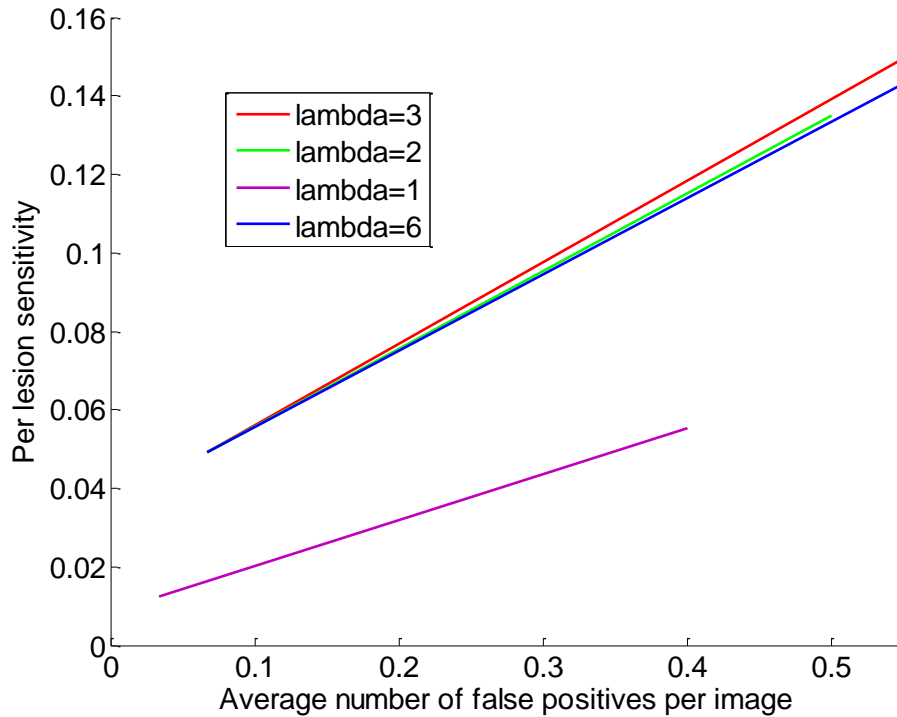


Figure 5.15: FROC curves comparing different λ (5.5) values.

5.6 Summary

In this chapter we proposed methods to detect MA using a two step process. First, we apply MSCF to locate all possible MA candidates. These candidates are then classified with the help of DL and CDL with SRC. The CDL model builds upon DL by minimizing the distance from the sparse coding coefficients of a class to its class center. This along with the reconstruction error can be used to classify MA candidates. Experimental results on both the ROC and DIARETDB1 datasets clearly demonstrate the superiority of the CDL scheme over DL and others, leading to a higher sensitivity for the same false positive. In the next chapter an automatic OD detection method on Asian OD is described. The method is composed of OD Vessel Candidate Detection and OD Vessel Candidate Matching. OD Vessel Candidate Detection uses Multi-scale Gaussian Filtering, while the latter is accomplished with a Vessels' Directional Matched Filter.

Chapter 6

Detecting Optic Disc on Asians by Multi-scale Gaussian Filtering and a Vessels' Directional Matched Filter

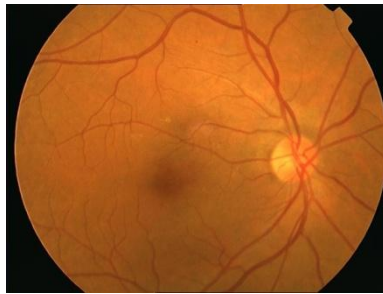
In this chapter a method to automatically detect the optic disc (OD) of Asians is presented. In Section 6.1 an Introduction is given. Section 6.2 describes the material used and Section 6.3 presents the proposed method, consisting of two steps, OD Vessel Candidate Detection and OD Vessel Candidate Matching. Experimental results are relayed in Section 6.4 followed by a discussion in Section 6.5. We conclude with a summary in Section 6.6.

6.1 Introduction

Ethnicity affects the optic disc shape. A study conducted by [140], [141], [142] measuring disc area, cup volume, maximal cup depth, and vertical cup-disc ratio showed Asians have higher values in these properties compared to Caucasians. This can be clearly seen in Fig. 6.1 where the top image [132] is Caucasian while the bottom is Asian, taken from our database (explained in the proceeding Section). Further studies [143], [144], [145], [146], demonstrated that with an increase in size of the OD, blood vessels (both arteries and veins) increase in thickness. Where venular widening is linked with progression of DR [146] and narrowing of the arteriolar is associated with the risk of diabetes [146]. The increase in vessel thickness caused by an enlarged OD can be seen in Fig. 6.2, which shows the cross-sections of both thick (a-b) and thin (c-d) vessels, taken from two individuals. The dotted line is Caucasian while the solid line is Asian. Generally speaking for thick vessels the cross-section of Asians is about 3-4 pixels wider than Caucasians. On the other hand, for thin vessels the difference is around 1-2 pixels. In order to achieve a fair assessment we examined vessels only in the OD, comparing with the same orientation and grade of DR.

Most of the current algorithms working on automatic OD detection are from Western countries, therefore, we can safely assume that the fundus images collected in their database are of Caucasians. Hence, there is a need to accurately detect the OD from Asians as state-of-the-art algorithms do not take into account the increased OD size and its subsequent consequences. A distinction needs to be made between automatic OD detection and automatic OD boundary detection. The former refers to the location of the disc center while the latter aims to segment the OD by detecting the boundary between the retina and the nerve head. Our work is detecting the OD center.

This chapter attempts to solve the problem of automatic OD detection on Asians by proposing a method that uses both vessel and intensity information to complement existing algorithms. In the first step, a vessels' directional map representing the OD vessel candidates is calculated using Multi-scale Gaussian Filtering with scale production, and double thresholding. This accounts for the thicker vessels of Asians. A Vessels' Directional Matched Filter (VDMF) template (with bilinear interpolation) is matched to each OD vessel candidate as part of the second step, based on Youssif [117]. The pixel candidate having the least difference with the template is assigned the OD center.

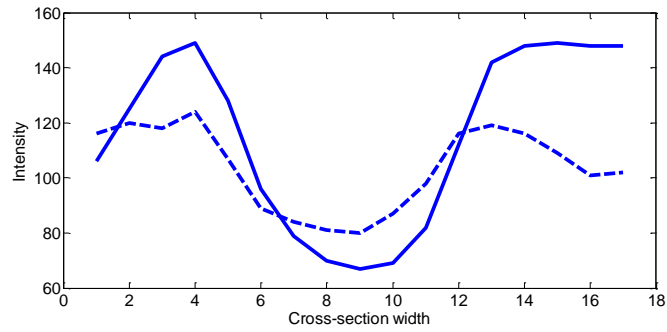


(a)

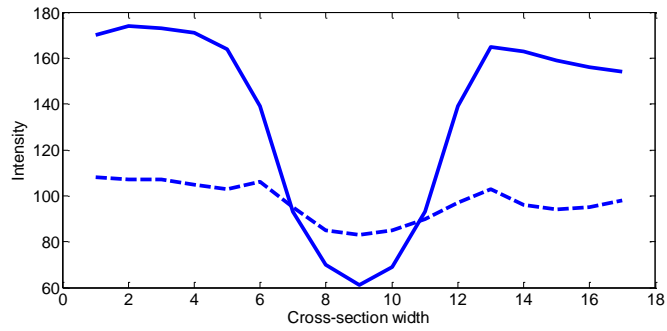


(b)

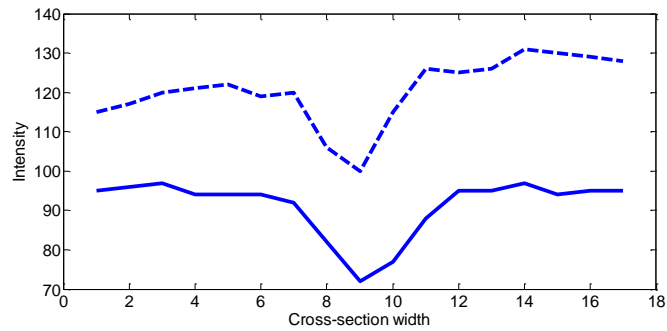
Figure 6.1: Comparison of Caucasian retina (a) to Asian (b). Disc area, cup volume, maximal cup depth, and vertical cup-disc ratio are larger in (b) compared to (a).



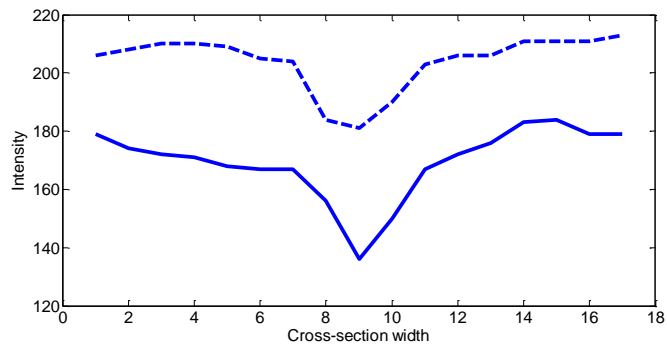
(a)



(b)



(c)



(d)

Figure 6.2: Thick (a) and (b); thin (c) and (d) vessel cross-sections. The solid line is Asian while the dotted comes from Caucasian, taken from two individuals.

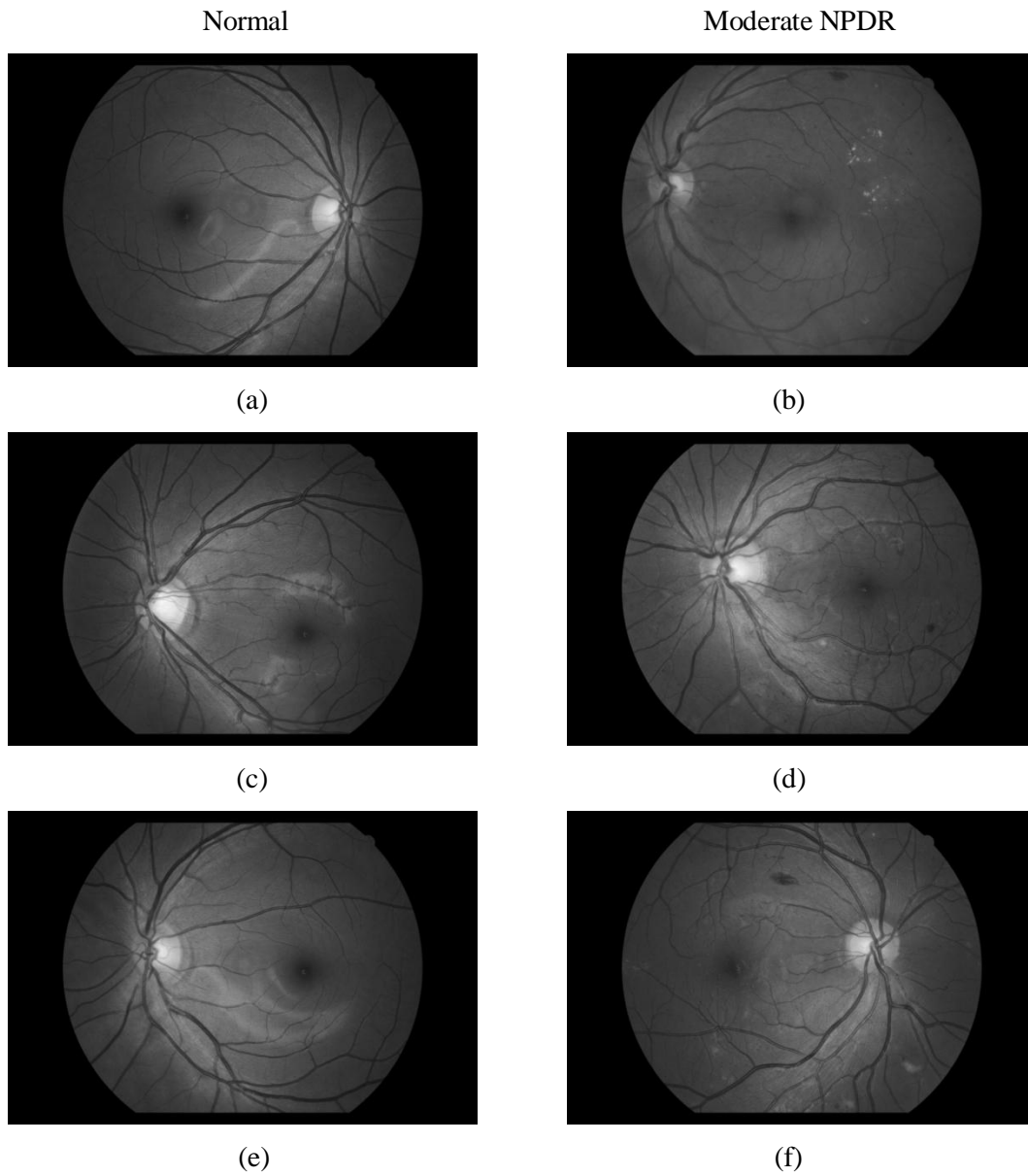


Figure 6.3: (a), (c), and (e) Normal fundus image from HIT. (b), (d), and (f) fundus diagnosed with moderate NPDR from HIT.

6.2 Material

We constructed a new database obtained from a DR screening programme in Harbin, China. The patients' consent was obtained according to the Declaration of Helsinki and the Ethical Committee of

the Institution in which the work was performed has approved it. This database will be referred to as the HIT database. HIT consists of 402 images, broken down into 46 normal and 356 pathological (all with DR). The 356 DR images can be further divided into 181 mild NPDR, and 175 moderate NPDR, classified based on [147]. The images were captured in digital form using a Canon CR-DGi Non-Mydriatic Retinal Camera at 45° field of view (FOV). The size of each image is 1936 × 1288 pixels with 24 bits and in compressed JPEG-format. We decided to use a non-mydriatic camera to reduce the stress for the patient and enable examinations without the use of pupil dilating eye drops. Fig. 6.3 shows examples of images from HIT, the ones on the left are healthy retinas while the others have moderate NPDR. The OD center in each image of the database was manually segmented by me.

6.3 Proposed Asian OD Detection Method

6.3.1 OD Vessel Candidate Detection

Multi-scale Gaussian Filtering is based on Matched Filters first proposed in [34] to detect vessels. Due to the cross-section of vessels being Gaussian shaped, Gaussian functions can be used to match vessels. The idea of multi-scale allows more than one scale to be used which can match vessels of various widths. As an example, Fig. 6.4 shows a Gaussian filter at three scales and eight orientations. The Multi-scale Gaussian Filter is defined as:

$$f_i(x, y) = \frac{1}{\sqrt{2 \cdot \pi} \cdot s_i} \exp\left(-\frac{x^2}{2 \cdot s_i^2}\right) - m, \quad \text{for } |x| \leq t \cdot s_i, \quad |y| \leq L_i/2 \quad (6.1)$$

where s_i represents the scale of the filter;

$$m = \left(\int_{-t \cdot s_i}^{t \cdot s_i} \frac{1}{\sqrt{2 \cdot \pi} \cdot s_i} \exp\left(-\frac{x^2}{2 \cdot s_i^2}\right) dx \right) / (2 \cdot t \cdot s_i)$$

is used to normalize the mean value of the filter to 0 so that the smooth background can be removed after filtering; and L_i is the length of the neighborhood along the y -axis to smooth noise; t is a constant and is usually set as 3 because more than 99% of the area under the Gaussian curve lies within the range of $[-3s_i, 3s_i]$. The parameter L_i is also chosen based on s_i . When s_i is small, L_i is set relatively small, and vice versa. In the actual implementation $f_i(x, y)$ will be rotated to detect the vessels of different orientations. Normally, we choose three (large, medium and small) s_i based on the cross-section of vessels analyzed. The widest cross-section is assigned the largest s_i , the thinnest the smallest and the third s_i (medium) is calculated by taking the average of the other two (largest and

smallest). Eight or twelve directions are usually chosen to cover all possible orientations of the vessel including horizontal, vertical and diagonal.

The response of Multi-scale Gaussian Filtering can be expressed by:

$$R_i(x, y) = f_i(x, y) * im(x, y) \quad (6.2)$$

where $im(x, y)$ is a normalized green channel image and $*$ denotes convolution. The scale production is defined as the product of filter responses at two scales i and j :

$$P_{i,j}(x, y) = R_i(x, y) \cdot R_j(x, y) \quad (6.3)$$

Fig. 6.5 illustrates the advantage of Multi-scale Gaussian Filtering and scale production. s represents the noise free cross-sections of vessels. f is s with noise added. R_1 is the response (6.2) of using a small scale, R_2 using a medium scale and R_3 a large scale all on f . With R_1 the thin cross-sections are detected in f but the thick ones are missed. R_3 can detect the thick vessels but not the thin ones, while R_2 can detect almost all but with a lot of noise in its result. By combining the responses the detection result can be significantly improved. One way of merging the responses is to use *Max*, this takes the maximum intensity at each pixel value from the three responses. Even though *Max* is able to detect the four peaks in s , its result contains too much noise. To filter out this noise scale production (6.3) can be applied. $P_{1,2}$ is the scale production of R_1 and R_2 , $P_{2,3}$ is the scale production of R_2 and R_3 . The best result is $P_{2,3}$ found on the last row of Fig. 6.5 which removes most of the noise and clearly shows the four peaks with variable thicknesses.

Double thresholding is then applied to $P_{i,j}(x, y)$ to generate a binary image where a one pixel wide center-line of the vessel is detected using morphological thinning. The morphological thinning algorithm uses the hit-and-miss transform and can be expressed in terms of it:

$$\text{thin}(A, B) = A - \text{hit-and-miss}(A, B) \quad (6.4)$$

where A is the original image, B is the structure element applied to A and $-$ is logical subtraction. The thinning operation functions by applying the origin of the structure element to every pixel in the original image while at the same time comparing it with its surrounding image pixels. If the background (zero) and foreground (one) pixels in the structure element matches exactly with the background and foreground pixels in the original image, then the pixel under the origin (of the structure element) is set to one (foreground) otherwise, the pixel is set to the background. This process is applied many times until no further changes in the image are made. For double thresholding a low threshold t_l and a high threshold $t_h = 2 \cdot t_l$ are imposed on a production where

two maps V_l and V_h are obtained. The values in the production below t_l are removed as noise (set to the value of 0 in the binary image) and the remaining (set to the value 1 in the binary image) are extracted as vessel features to V_l . The same procedure is applied for t_h , however, this time values above t_h are removed as noise while values below t_h are placed in V_h . The final map is formed as the intersection of V_l and V_h . This process is repeated for each production using the same thresholds. The final binary image is attained by fusing every production's final map with logical OR.

The vessels' directional map is calculated by finding the corresponding orientation that produced the maximum response with $f_i(x, y)$ (use of the vessel feature). This map is thinned by multiplying with the center-line vessel. Using the notation that the OD has higher intensity (use of the intensity feature) than its surrounding retinal background, any pixels less than 0.9 in $im(x, y)$ are removed. A 51×51 neighborhood of each remaining pixel is extracted in order to better represent the OD vessels. This results in the OD vessel candidates. In some situations hard exudates may also be part of the OD vessel candidates since their pixel intensity is also high. However, these objects are not made of vessels and will be removed in the following step.

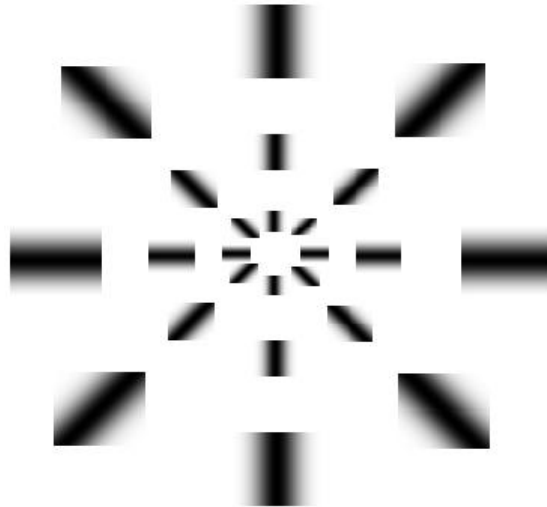


Figure 6.4: Gaussian filter design at three different scales and eight directions.

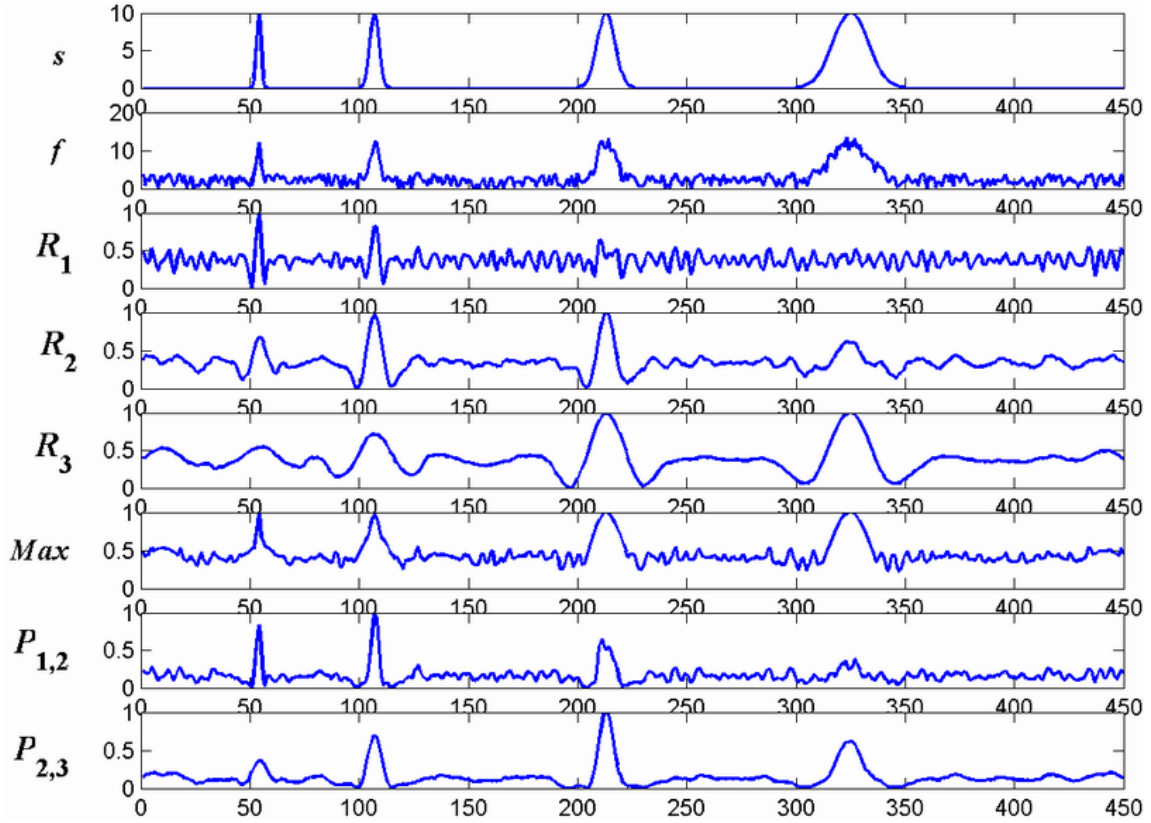


Figure 6.5: Multi-scale filters and scale production: s is the original signal; f is the noisy measurement of s ; R_1 , R_2 and R_3 are the filter responses to f at different scales; Max is the maximum values among R_1 , R_2 and R_3 ; $P_{1,3}$ is the scale production of R_1 and R_2 , and $P_{2,3}$ is the scale production of R_2 and R_3 .

6.3.2 OD Vessel Candidate Matching

We define a 9×9 template as the VDMF shown in Table 6.1, where 8 orientations are used instead of 12 [117]. In order to account for the various sizes of vessel maps in the OD, bilinear interpolation was employed to restructure the template into 61×21 and 121×41 . This maintains the elongated shape of the OD where the values and sizes are specifically tuned for HIT. [117] employed different template dimensions suited for their database. Each of the two templates is matched to the candidates with an absolute difference calculated. This is accomplished by sliding the template across each candidate pixel, everytime calculating the absolute difference with the candidate it covers. The resultant difference from the two templates is then summed, and the candidate pixel with the least

accumulated difference assigned the OD center. This makes sense intuitively because the smaller the accumulated difference the more the templates matched the candidate.

Fig. 6.6 illustrates the steps of the proposed method using an example. In (a) we have a retinal image shown in its green channel. After applying Multi-scale Gaussian Filtering and scale production the result in (b) is obtained. Double thresholding is then applied to (b) to get (c) where its vessels are thinned in (d). The OD Vessel Candidates of (a) are found and displayed in (e). Finally, using the two templates in OD Vessel Candidate Matching, the pixel with the smallest accumulated difference is designated the OD center.

Table 6.1: A vessels' directional matched filter designed for HIT.

7	6	6	6	1	4	4	4	3
8	7	6	6	1	4	4	3	2
8	8	7	6	1	4	3	2	2
8	8	8	7	1	3	2	2	2
5	5	5	5	1	5	5	5	5
2	2	2	3	1	7	8	8	8
2	2	3	4	1	7	8	8	8
2	3	4	4	1	6	7	8	8
2	3	4	4	1	6	6	7	8

6.4 Experimental Results

The key parameters in our experiments were set as follows: $s_1 = 1.5$, $s_2 = 1.8$, $s_3 = 2.0$, $s_4 = 2.4$, with corresponding $L_1 = 9$, $L_2 = 9$, $L_3 = 13$, $L_4 = 13$, and 8 orientations (refer to (6.1)). The scale production of s_1 and s_2 were combined along with the result of s_3 and s_4 . These parameters were chosen based on our experimental experience. It took 29 secs to process each image using a 2.40GHz Intel Centrino Pro with 2GB RAM. In order to improve the computation time of the proposed method every image in HIT was resized by 0.5 to 968×644 pixels. In literature the detected OD center is considered correct if it is positioned within 60 pixels of the manually identified center [29], [117], [127]. However, the images [29], [117], [127] used were 605×700 pixels.

In order to compensate for the larger images in HIT, the distance from the manually identified center to the detected OD center was increased to 80 pixels. For completeness we have included results using both 80 and 60 pixels, and compared the proposed method to Youssif [117] as well as single-scale. Single-scale [34], as the name suggests uses one s_i in (6.1) instead of many (as is the case with multi-scale). This is combined with VDMF to detect the OD and evaluated against the proposed method. These can be found in Tables 6.2 and 6.3 respectively. Columns 2-5 in Tables 6.2 and 6.3 represent the number of normal, mild NPDR, moderate NPDR and the total number of images. With 80 pixels the OD center in all of normal were detected using the proposed method. Only 1 and 2 were missed in mild and moderate NPDR which lead to an overall success rate of 99.25% (399/402). As for Youssif [117], 2 were not detected in normal, 4 in mild NPDR and 4 again in moderate NPDR. The result of single-scale can be found in the last row, where 44, 178 and 170 were detected respectively for each of the three DR classes. Using 60 pixels (see Table 6.3), the proposed method missed 1 in all of normal, 4 from mild NPDR and 4 in moderate NPDR. The success rate was 97.76% (393/402). Obviously, by raising the standard from 80 to 60 pixels the success rate is bound to drop which is the situation here. In cases where the OD center failed to be detected, one of the main reasons was low contrast exhibited by the image. We admit in such cases our method may fail. Youssif [117] on the other hand failed to detect 9, 13 and 16 from the three classes, while single-scale missed 8 from normal, 12 from mild NPDR and 18 in moderate NPDR.

Table 6.2: OD detection result on HIT using 80 pixels as standard.

Number of Images in Each Group				Total
	46	181	175	402
Method	Number Correctly Detected			
Proposed Method	46	180	173	399
Youssif [117]	44	177	171	392
Single-scale	44	178	170	392

Table 6.3: OD detection result on HIT using 60 pixels as standard.

Method	Number of Images in Each Group			Total
	46	181	175	402
Method	Number Correctly Detected			
Proposed Method	45	177	171	393
Youssif [117]	37	168	159	364
Single-scale	38	169	157	364

Table 6.4: Average distance (in pixels) of detected and actual OD.

Method	Number of Images in Each Group			Total
	46	181	175	402
Method	Average Distance Between Estimated and Actual OD Center (pixels)			
Proposed Method	27.867	28.799	31.127	29.264
Youssif [117]	33.5163	36.0915	37.5733	35.7270
Single-scale	39.9901	36.1220	44.2674	40.1265

Table 6.4 which has the same format as the previous two illustrates the average distance between the estimated and manually identified OD centers. In this table the proposed method’s average distance of normal is 27.847 pixels, 28.799 for mild NPDR, 31.127 in the case of moderate NPDR, and 29.264 for the average of all three. This compares to averages of 35.7270 using Youssif [117] and 40.1265 with single-scale. Fig. 6.7 shows the OD detection results of the proposed method on images from HIT. A white cross in each image marks the location of the detected OD center.

6.5 Discussion

The variables in (6.1) were chosen based on extensive experiments. Because there is no ground truth for the vessel maps, our criteria is judged on the visual result (binary image of segmented vessel map) of several images. We tested $s_i = 0.5 \cdots 3$ and found the current parameters in Section 6.4 to give the best result. As for the two template sizes in Section 6.2, 61×21 corresponds to covering a smaller

vessel map in the OD while 121×41 is for maps of medium to large dimensions. These are shown in Fig. 6.8 (a) and (b) correspondingly.

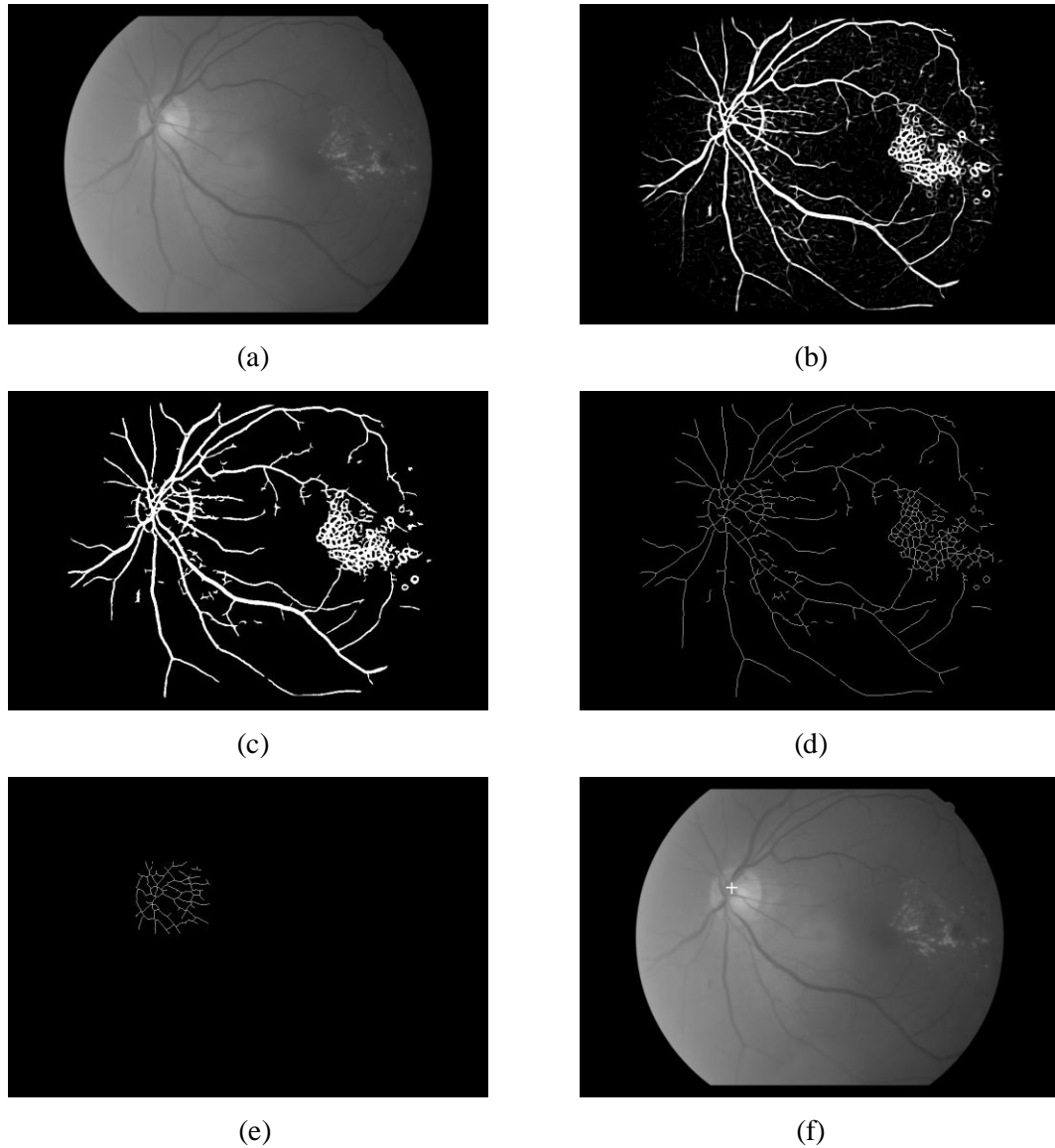


Figure 6.6: Steps of the proposed method applied to a fundus image (a). (b) is the scale production of (a). The result of double thresholding on (b) is (c). The thinned vessels of (c) is (d). (e) is the OD vessel candidates after removing pixels with low intensities. The detected OD center is illustrated in (f) by a cross.

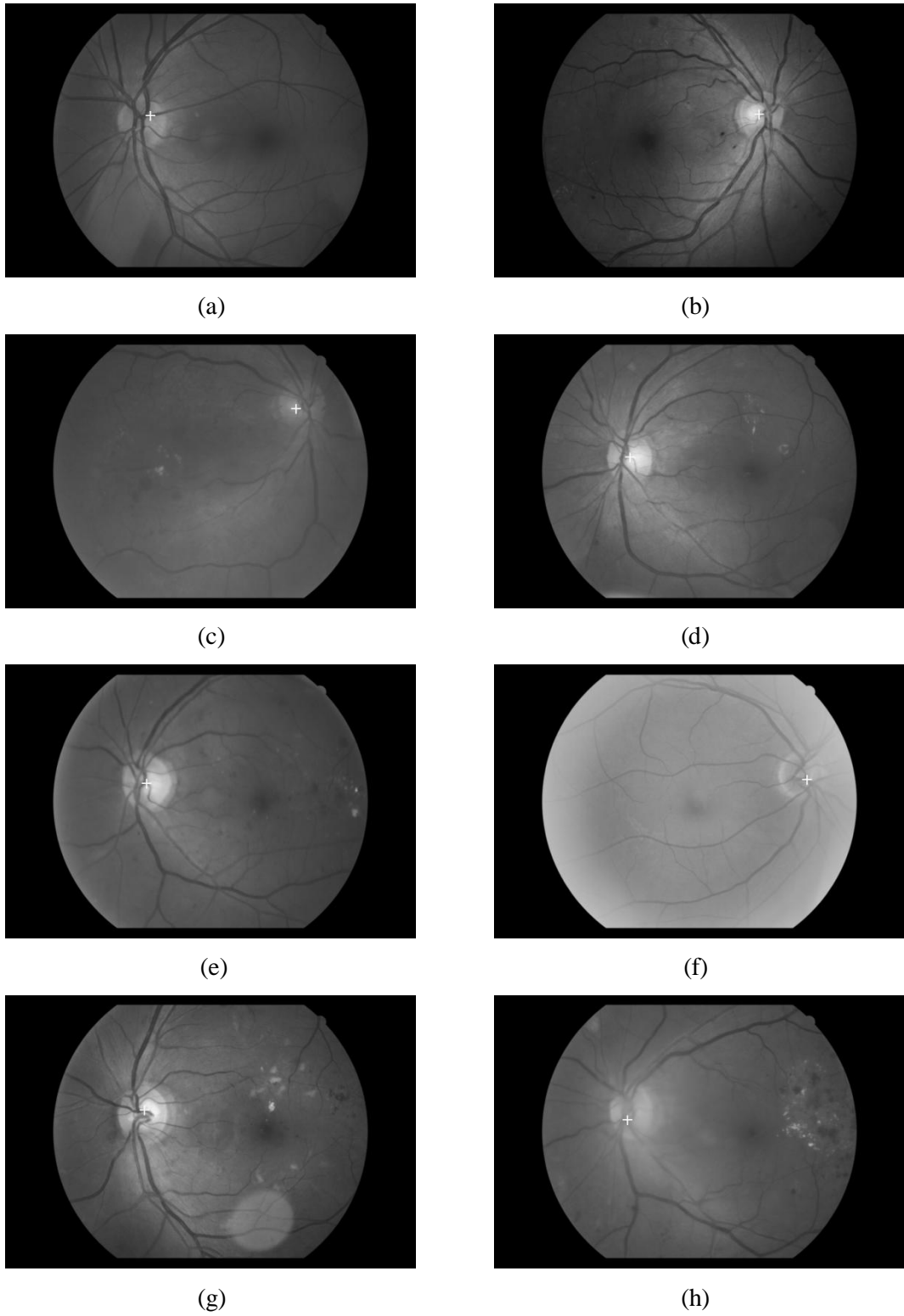


Figure 6.7: Results of the proposed method where a white cross represents the detected OD center.

Fig. 6.9 depicts the result of increasing/decreasing the template size by a factor of ± 1.5 with respect to detected and actual OD distance. With $+1.5$ the dimension of the largest template becomes 151×51 . Using such templates the average distance of detected and actual OD is 37.6886 pixels (furthest right point in Fig. 6.9). On the other hand, -1.5 leads to an average distance of 31.7621 shown as the furthest left point in Fig. 6.9. The smallest distance is achieved with the current templates discussed above, and shown in Fig. 6.9 as the central point.

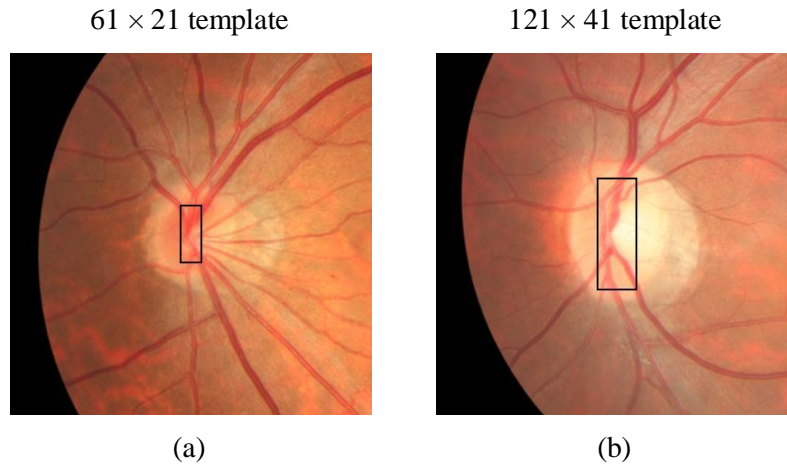


Figure 6.8: A small vessel map is covered with the 61×21 template (a). Medium to large maps are covered using the 121×41 template (b).

The results from Table 6.2 demonstrate that even if the proposed method, Youssif [117] and single-scale achieve similar accuracy using 80 pixels (with 7 image difference to the proposed method), their gap is much wider with 60 pixels (29 image variation). Subsequently, the average distance between actual and estimated OD centers of the proposed method and single-scale is close to 11 pixels while for Youssif [117] it is slightly less than 6 pixels. This shows the proposed method is more accurate at OD detection compared to the others. Note in Table 6.2 and 6.3 Youssif [117] and single-scale detected the same number of OD. We believe this to be the case because both methods incorporate single-scale vessel extraction in order to locate OD vessel candidates.

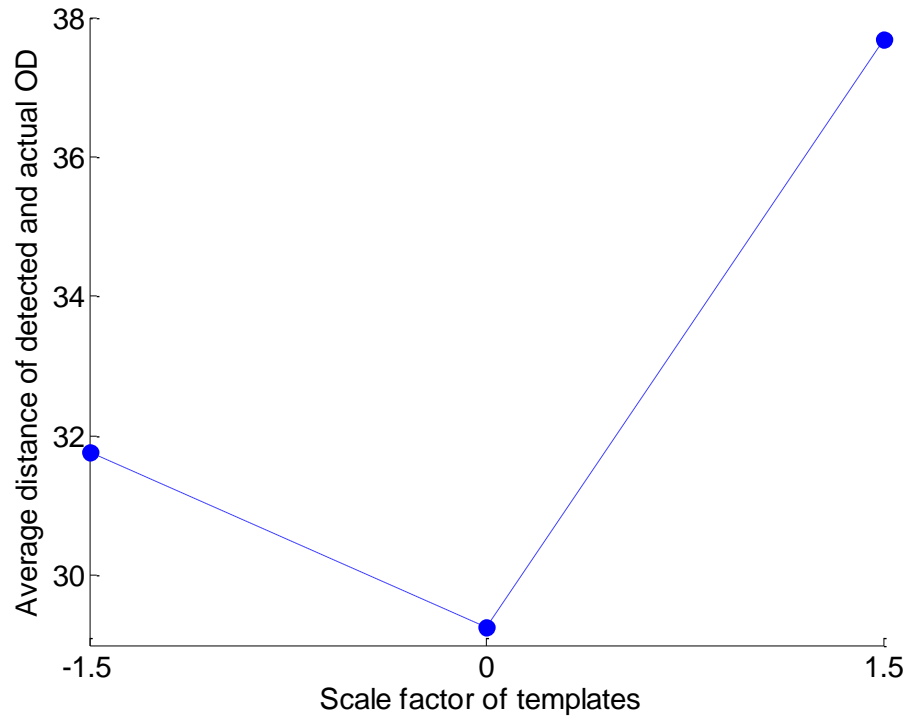


Figure 6.9: The result of average distance compared with various scale factors applied to the templates. From right to left, the first point is +1.5, next is the current template size, and the left point is -1.5.

Fig. 6.10 illustrates a sample of the OD detection results of the proposed method, single-scale and Youssif [117]. In total three images were used, one from each DR group. The columns in Fig. 6.10 represent the different OD detection methods. In this figure you can clearly see that the proposed method was able to detect the OD (all marked with a white cross except (a) which used a black cross), while the other two methods failed. Each of the retinal images in this figure is composed of a vascular map that consists of both thick and thin vessels. Hence, multi-scale with VDMF was able to triumph while single-scale and Youssif [117] were unsuccessful, due to its inability to match both thick and thin vessels found in Asians as well as account for a larger OD. This underlines the necessity of the proposed method at OD detection on Asians.

Other advantages of the proposed method include its capacity to calculate a vessels' directional map (in OD Vessel Candidate Detection) implicitly, while extracting the vessels without any

additional algorithms as needed in [148], [149]. Also, our proposed method does not make any assumptions about the location of the OD in the image. In computer aided diagnosis of HIT, vessel extraction is a first step. Hence, the time needed to extract the vessels can be discounted.

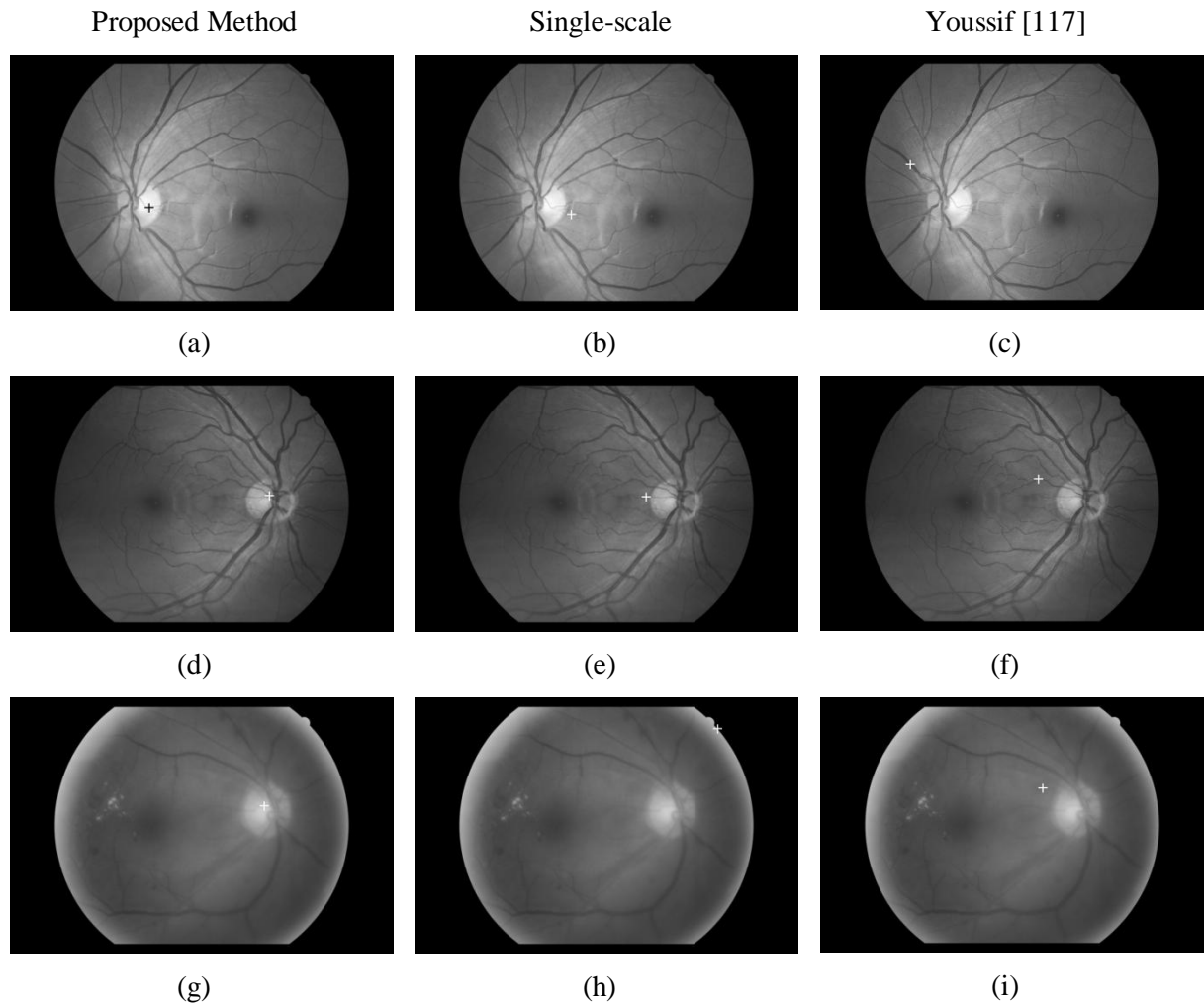


Figure 6.10: Visual comparison of the OD detection results (proposed method with others).

6.6 Summary

This chapter presented a method for automatic detection of the Asian OD to complement existing algorithms using two steps, OD vessel candidate detection, and OD vessel candidate matching. The study was deemed necessary since an Asian OD is typically larger than Caucasians, and has thicker

vessels. The proposed method makes use of the OD intensity information by removing low pixel values, and incorporates the vessel information in the form of a vessel's directional map. The use of Multi-scale Gaussian Filtering at extracting both thin/thick vessels and the VDMF can be attributed to the high OD detection results seen in Tables 6.2-6.4. These tables along with Fig. 6.10 show that algorithms developed in the West cannot adequately deal with the added properties of an Asian OD. Also, the use of single-scale and Youssif [117] are insufficient to match the various widths of the vessel. The succeeding chapter discusses improvements to current methods as well as describing future work in this research.

Chapter 7

Future Work

This chapter discusses work on the continuation of retinal image analysis and its use in medical applications. Section 7.1 talks about improving the proposed methods described above. Section 7.2 touches on future work including extracting additional features, developing a generalized OD detection method, conducting further experiments on HIT, and applying DL and CDL with SRC to vessel extraction. A list of publications this thesis produced is in Section 7.3.

7.1 Improvements to Current Methods

7.1.1 MF-FDOG at Vessel Detection

The use of multiple scales to extract both thick and thin vessels followed by logical OR to combine the results is effective in general. However, our logical OR operation is not strong enough to remove unwanted structures. Some noisy patterns that exist in either scale can be preserved in the resultant vessel map. This is the weakness of the proposed work. One way to remove the noisy patterns is to employ some post-processing procedures based on their geometric features. Another aspect to be improved for MF-FDOG is the handling of branching points and the connectivity of vessels. If isolated vessels can be connected to the correct object(s), sensitivity and accuracy will be further improved.

7.1.2 Enhancing Low Contrast Microaneurysms

In order to combat the problem of low contrast exhibited by true microaneurysms (Section 4.3), a special filter known as the iris filter [150] can be used. This filter is designed to detect and enhance rounded shapes with a weak contrast against its surrounding neighborhood. Blood vessels and other elongated objects are insensitive to the iris filter which makes it ideal for microaneurysm detection. The iris filter has successfully been applied to locate malignant tumors found in mammogram [151].

7.1.3 Dictionary and Centralized Dictionary Learning with Sparse Representation Classifier

Recall from (5.9) that the fusion function $f(\cdot)$ is simply $f(r_i(\mathbf{y}) + d_i(\mathbf{y}))$. By adopting a more sophisticated fusion function, e.g. adding weights $w_r \cdot r_i(\mathbf{y})$ and $w_d \cdot d_i(\mathbf{y})$, where $w_r + w_d = 1$, better classification performance can be achieved. We will also examine how to involve more class

discrimination information into the dictionary learning process, to make the sparse representation based MA detection method more powerful and efficient.

7.1.4 OD Detection of Asians

We have carefully examined the cases in which the proposed method failed to correctly detect the OD center. In the majority of failed detections, poor contrast, imaging artifacts and the presence of pathology, or a combination of these factors have attributed to the problem. When contrast over the OD is low, this affects the result of OD vessel candidate detection. As part of the future work, the aspect of contrast enhancement will be integrated to deal with such cases.

7.1.5 Better Scale Selection

Vessel extraction in Chapters 3 and 6 along with microaneurysm detection in Chapters 4 and 5 can be improved by flexible scale selection. The initial experimental results show that scales cannot be randomly selected as this would affect the outcome of the responses. If the scale is too small a lot of noise will persist and if too large, finite details will be lost. Currently there is no definite way of choosing scales. As part of improving the proposed methods, an investigation into automatic scale selection will be conducted.

7.2 Future Work

7.2.1 Extraction of other Retinal Features

Bright lesions, hemorrhages and the fovea/macula are the main features in the retina that remain to be extracted [152]. Bright lesions include hard (yellow) and soft (white) exudates which are fluids that leaks from blood vessels. Hemorrhages are abnormal bleeding of the retinal blood vessels in the retina. The size of each hemorrhage can vary widely, from as small as a microaneurysm, to as large as a few times the size of the OD. Fovea/macula are located in the center of retina. Not only do they play a pivotal role in vision, but their position is vital in establishing a point of reference in the retina. Therefore, to better analyze retinal images and its use in medical applications, these additional features require extraction.

7.2.2 Developing a General Purpose Automatic OD Detection Method

An automatic OD detection method for Asians was presented in Chapter 6. Based on principles of OD Vessel Candidate Detection and OD Vessel Candidate Matching, using both intensity and vessel

features of the OD, we would like to develop a generalized OD detection method. This means the method is not specifically designed for the OD of any ethnicity or disease, and should achieve good results regardless of these factors. Once completed the results can be validated on several public databases.

7.2.3 Conducting Further Experiments on HIT

Full potential of the HIT database has not been realized, as only the OD was detected. In light of the fact that ethnicity affects the OD, the question remains if other features also differ by race, specifically Asians compared to others. At the same time with an Asian database available more work can be done in examining retinopathy specific to this race [153], [154], [155], [156], [157], [158], [159], [160], [161], [162]. To investigate both matters further we need to study the anatomy of the retina in detail.

7.2.4 Vessel Extraction via Dictionary and Centralized Dictionary Learning with SRC

With the success of DL and CDL with SRC applied to microaneurysm detection, the same technique can also be used in vessel extraction. The problem of vessel extraction in this case becomes a two class classification problem. The candidate object is either a vessel or non-vessel. This means we would use two dictionaries, one to represent the vessels and another to represent the non-vessels. Both dictionaries can be constructed in two ways. One is based on using the ground truth and taking the cross-section of vessels at different orientations. The other method involves generating artificial cross-sections of vessels and step edges (non-vessels).

Vessel extraction then becomes a two step process. In the first step, the vessel candidates are located using some form of filtering with multi-scale to match vessels of various thicknesses and directions. In the next step, two dictionaries are learnt from vessel and non-vessel samples. With the learnt dictionaries SRC is applied to classify each candidate.

7.3 Publication List

The work in this thesis has generated a number of publications listed below.

7.3.1 Journal Publications

- B. Zhang, X.Q. Wu, J. You, Q. Li, and F. Karray, "Detection of Microaneurysms using Multi-scale Correlation Coefficients," *Pattern Recognition*, vol. 43, no. 6, pp. 2237-2248, 2010.
- B. Zhang, L. Zhang, L. Zhang, and F. Karray, "Retinal Vessel Extraction by Matched Filter with First-Order Derivative of Gaussian," *Computers in Biology and Medicine*, vol. 40, no. 4, pp. 438-445, 2010.
- M. Niemeijer, B. van Ginneken, M.J. Cree, A. Mizutani, G. Quellec, C.I. Sanchez, B. Zhang, R. Hornero, M. Lamard, C. Muramatsu, X. Wu, G. Cazuguel, J. You, A. Mayo, Q. Li, Y. Hatanaka, B. Cochener, C. Roux, F. Karray, M. Garcia, H. Fujita, and M.D. Abramoff, "Retinopathy Online Challenge: Automatic Detection of Microaneurysms in Digital Color Fundus Photographs," *IEEE Transactions on Medical Imaging*, vol. 29, no. 1, pp. 185-195, 2010.
- B. Zhang, F. Karray, and L. Zhang, "Sparse Representation Classifier for Microaneurysm Detection and Retinal Blood Vessel Extraction," *Information Sciences*, under revision.
- B. Zhang, and F. Karray, "Detecting Optic Disc on Asians by Multi-scale Gaussian Filtering," *Computers in Biology and Medicine*, submitted to.
- B. Zhang, F. Karray, and L. Zhang, "Microaneurysm Detection Based on Centralized Dictionary Learning for Sparse Representation," *Medical Image Analysis*, will be submitted to.

7.3.2 Conference Publications

- B. Zhang, L. Zhang, J. You, and F. Karray, "Microaneurysm (MA) Detection via Sparse Representation Classifier with MA and Non-MA Dictionary Learning," Proceedings: International Conference on Pattern Recognition, Istanbul, Turkey, Aug. 23-26, 2010.
- B. Zhang, Q. Li, L. Zhang, J. You, and F. Karray, "Retinal Vessel Centerline Extraction Using Multiscale Matched Filter and Sparse Representation-based Classifier," Proceedings: International Conference on Medical Biometrics, pp. 181-190, Hong Kong, China, Jun. 28-30, 2010.

- B. Zhang and F. Karray, "Optic Disc Detection by Multi-scale Gaussian Filtering with Scale Production and a Vessels' Directional Matched Filter," Proceedings: International Conference on Medical Biometrics, pp. 173-180, Hong Kong, China, Jun. 28-30, 2010.
- B. Zhang and F. Karray, "Optic Disc and Fovea Detection via Multi-scale Matched Filters and a Vessels' Directional Matched Filter," Proceedings: International Conference on Autonomous and Intelligent Systems, pp. 1-5, Povo de Varzim, Portugal, Jun. 21-23, 2010.
- B. Zhang, X.Q. Wu, J. You, Q. Li, and F. Karray, "Hierarchical detection of red lesions in retinal images by multiscale correlation filtering," Proceedings: SPIE Medical Imaging 2009: Computer-Aided Diagnosis, vol. 7260, 72601L, Orlando, Florida, USA, Feb. 7-12, 2009.

Bibliography

- [1] Human Eye, http://en.wikipedia.org/wiki/Human_eye
- [2] How the Eye Works, <http://www.lighthouse.org/eye-health/the-basics-of-the-eye/how-the-eye-works/>
- [3] B. Zhang, J. You, F. Karray, C. Kee, and Q. Li, "Astigmatism and Eye Shape," Proc. in *2009 International Conference on Image Processing, Computer Vision, and Pattern Recognition*, Las Vegas, USA, July 13–16, pp.72–77, 2009.
- [4] J. Daugman, "High confidence visual recognition of persons by a test of statistical independence," *IEEE Trans. Pattern Analysis and Machine Intelligence*, vol. 15, no. 11, pp. 1148–1161, 1993.
- [5] D. Zhang, *Automated Biometrics: Technologies & Systems*, Kluwer Academic Publishers, 2000.
- [6] W. Boles and B. Boashash, "A Human Identification Technique Using Images of the Iris and Wavelet Transform," *IEEE Trans. Signal Processing*, vol. 46, no. 4, pp. 1185–1188, 1998.
- [7] S. Lim, K. Lee, O. Byeon, and T. Kim, "Efficient Iris Recognition through Improvement of Feature Vector and Classifier," *ETRI Journal*, vol. 23, no. 2, pp. 61–70, 2001.
- [8] C. Sanchez-Avila and R. Sanchez-Reillo, "Iris-Based Biometric Recognition Using Dyadic Wavelet Transform," *IEEE Aerospace and Electronic Systems Magazine*, vol. 10, pp. 3–6, 2002.
- [9] C. Tisse, L. Martin, L. Torres, and M. Robert, "Person Identification Technique Using Human Iris Recognition," Proc. in *Vision Interface*, Calgary, Canada, May 27–29, pp. 294–299, 2002.
- [10] Y. Zhu, T. Tan, and Y. Wang, "Biometric Personal Identification Based on Iris Patterns," Proc. in *International Conference on Pattern Recognition*, Barcelona, Spain, September 3–7, vol. 2, pp. 805–808, 2000.
- [11] L. Ma, and N. Li, "Texture Feature Extraction and Classification for Iris Diagnosis," Proc. in *International Conference on Medical Biometrics*, Hong Kong, China, January 4–5, pp. 168–175, 2008.

- [12] T.Y. Wong, and R. McIntosh, “Systemic associations of retinal microvascular signs: a review of recent population-based studies,” *Ophthalmic Physiol Opt.*, vol. 25, no. 3, pp. 195–204, 2005.
- [13] T.Y. Wong, W. Rosamond, P.P. Chang, D.J. Couper, A.R. Sharrett, L.D. Hubbard, A.R. Folsom, and R. Klein, “Retinopathy and risk of congestive heart failure,” *J Am Med Assoc.*, vol. 293, no. 1, pp. 63–69, 2005.
- [14] A.J. Frame, P.E. Undill, M.J. Cree, J.A. Olson, K.C. McHardy, P.F. Sharp, and J.V. Forrester, “A comparison of computer based classification methods applied to the detection of microaneurysms in ophthalmic fluorescein angiograms,” *Computers in Biology and Medicine*, vol. 28, no. 3, pp. 225–238, 1998.
- [15] A.M. Mendonca, A.J. Campilho, and J.M. Nunes, “Automatic segmentation of microaneurysms in retinal angiograms of diabetic patients,” Proc. in *International Conference of Image Analysis and Processing*, Venice, Italy, September 27–29, pp. 728–733, 1999.
- [16] T. Spencer, R.P. Phillips, P.F. Sharp, and J.V. Forrester, “Automated detection and quantification of microaneurysms in fluorescein angiograms,” *Graefe’s Archive for Clinical and Experimental Ophthalmology*, vol. 230, no. 1, pp. 36–41, 1992.
- [17] T. Spencer, J.A. Olson, K.C. McHardy, P.F. Sharp, and J.V. Forrester, “An image-processing strategy for the segmentation of microaneurysms in fluorescein angiograms of the ocular fundus,” *Computers and Biomedical Research*, vol. 29, no. 4, pp. 284–302, 1996.
- [18] J. Domingo, G. Ayala, A. Sim, E. de Ves, L. Martinez-Costa, and P. Marco, “Irregular motion recovery in fluorescein angiograms,” *Pattern Recognition Letters*, vol. 18, no. 8, pp. 805–821, 1997.
- [19] R. Sivakumar, “Staging of Diabetic Retinopathy using TVEP Phase Spectral Periodicity Analysis,” *International Journal of Medical Engineering and Informatics*, vol. 1, no. 2, pp. 174–186, 2008.
- [20] J.H. Hipwell, F. Strachant, J.A. Olson, K.C. McHardy, P.F. Sharp, and J.V. Forrester, “Automated detection of microaneurysms in digital red-free photographs: a diabetic retinopathy screening tool,” *Diabetic Medicine*, vol. 17, no. 8, pp. 588–594, 2000.

- [21] M. Larsen, J. Godt, N. Larsen, H. Lund-Andersen, A.K. Sjølie, E. Agardh, H. Kalm, M. Grunkin, and D.R. Owens, “Automated detection of fundus photographic red lesions in diabetic retinopathy,” *Investigat Ophthalmol Vis Sci.*, vol. 44, no. 2, pp. 761–766, 2003.
- [22] T. Walter, J.C. Klein, P. Massin, and A. Erginay, “A contribution of image processing to the diagnosis of diabetic retinopathy – detection of exudates in color fundus images of the human retina,” *IEEE Trans. Medical Imaging*, vol. 21, no. 10, pp. 1236–1243, 2002.
- [23] C. Sinthanayothin, J.F. Boyce, T.H. Williamson, H.L. Cook, E. Mensah, S. Lal, and D. Usher, “Automated detection of diabetic retinopathy on digital fundus images,” *Diabetic Medicine*, vol. 19, no. 2, pp. 105–112, 2002.
- [24] M. Niemeijer, B. van Ginneken, J. Staal, M.S. Suttorp-Schulten, and M.D. Abramoff, “Automatic detection of red lesions in digital color fundus photographs,” *IEEE Trans. Medical Imaging*, vol. 24, no. 5, pp. 584–592, 2005.
- [25] J. Staal, M.D. Abramoff, M. Niemeijer, M.A. Viergever, and B. van Ginneken, “Ridge based vessel segmentation in color images of the retina,” *IEEE Trans. Medical Imaging*, vol. 23, no. 4, pp. 501–509, 2004.
- [26] J.V.B. Soares, J.J.G. Leandro, R.M. Cesar Jr., H.F. Jelinek, and M.J. Cree, “Retinal vessel segmentation using the 2-D gabor wavelet and supervised classification,” *IEEE Trans. Medical Imaging*, vol. 25, no. 9, pp. 1214–1222, 2006.
- [27] M. Niemeijer, J. Staal, B. van Ginneken, M. Loog, and M.D. Abramoff, “Comparative study of retinal vessel segmentation methods on a new publicly available database,” Proc. in *SPIE Medical Imaging*, San Diego, USA, February 19, vol. 5370, pp. 648–656, 2004.
- [28] M. Martínez-Pérez, A. Hughes, A. Stanton, S. Thom, A. Bharath, and K. Parker, “Scale-space analysis for the characterisation of retinal blood vessels,” Proc. in *Medical Image Computing and Computer-Assisted Intervention*, Cambridge, UK, September 19–22, pp. 90–97, 1999.
- [29] A. Hoover, V. Kouznetsova, and M. Goldbaum, “Locating blood vessels in retinal images by piecewise threshold probing of a matched filter response,” *IEEE Trans. Medical Imaging*, vol. 19, no. 3, pp. 203–210, 2000.
- [30] X. Jiang, and D. Mojon, “Adaptive local thresholding by verification based multithreshold probing with application to vessel detection in retinal images,” *IEEE Trans. Pattern Analysis*

- Machine Intelligence*, vol. 25, no. 1, pp. 131–137, 2003.
- [31] A.M. Mendonca, and A. Campilho, “Segmentation of retinal blood vessels by combining the detection of centerlines and morphological reconstruction,” *IEEE Trans. Medical Imaging*, vol. 25, no. 9, pp.1200–1213, 2006.
- [32] M.E. Martínez-Pérez, A.D. Hughes, S.A. Thom, A.A. Bharath, and K.H. Parker, “Segmentation of blood vessels from red-free and fluorescein retinal images,” *Medical Image Analysis*, vol. 11, no. 1, pp. 47–61, 2007.
- [33] G.G. Gardner, D. Keating, T.H. Williamson, and A.T. Elliott, “Automatic detection of diabetic retinopathy using an artificial neural network: a screening tool,” *Br J Ophthalmol.*, vol. 80, no. 11, pp. 940–944, 1996.
- [34] S. Chaudhuri, S. Chatterjee, N. Katz, M. Nelson, and M. Goldbaum, “Detection of blood vessels in retinal images using two-dimensional matched filters,” *IEEE Trans. Medical Imaging*, vol. 8, no. 3, pp. 263–269, 1989.
- [35] C. Sinthanayothin, J. Boyce, H. Cook, and C.T. Williamson, “Automated localisation of the optic disk, fovea, and retinal blood vessels from digital colour fundus images,” *Br J Ophthalmol.*, vol. 83, no. 8, pp. 902–910, 1999.
- [36] CR-DGi Non-Mydriatic Reinal Camera, <http://www.canon.co.id/p/EN/230-Ophthalmic-Equipment/536-Ophthalmic/324-CR-DGi-Non-Mydriatic-Reinal-Camera/>
- [37] G.W. Awcock and R. Thomas, *Applied Image Processing*, McGraw Hill, 1996.
- [38] J.A. Kylstra, T. Wierzbicki, M.L. Wolbarsht, M.B. Landers, and E. Stefansson, “The relationship between retinal vessel tortuosity, diameter, and transmural pressure,” *Graefes Arch Clin Exp Ophthalmol.*, vol. 224, no. 5, pp. 477–480, 1986.
- [39] P. Henkind, and G. Morgan, “Peripheral retinal angioma with exudative retinopathy in adults (Coats’ lesion),” *Br J Ophthalmol.*, vol. 50, pp. 2–11, 1966.
- [40] Y. Wang, A. Lu, J. Gil-Flamer, O. Tan, J.A. Izatt, and D. Huang, “Measurement of total blood flow in the normal human retina using Doppler Fourier-domain optical coherence tomography,” *Br J Ophthalmol.*, vol. 93, no. 5, pp. 634–637, 2009.
- [41] H. Kolb, E. Fernandez, and R. Nelson, editors, *Webvision: The Organization of the Retina and Visual System [Internet]*, Salt Lake City (UT): University of Utah Health Sciences

- Center, 1995.
- [42] D. Purves, G.J. Augustine, D. Fitzpatrick, L.C. Katz, A.S. LaMantia, J.O. McNamara, and S.M. Williams, editors, *Neuroscience*, 2nd edition, Sunderland (MA): Sinauer Associates, 2001.
- [43] P. Ganesan, S. He, and H. Xu, “Development of an image-based network model of retinal vasculature,” *Ann Biomed Eng.*, vol. 38, no. 4, pp. 1566–1585, 2010.
- [44] G.K. Asdourian, and M.F. Goldberg, “The angiographic pattern of the peripheral retinal vasculature,” *Arch Ophthalmol.*, vol. 97, pp. 2316–2318, 1979.
- [45] M.J. Hogan, and L. Feeney, “The ultrastructure of retinal blood vessel, I. The large vessels,” *J Ultrastr Res.*, vol. 9, pp. 10–28, 1963.
- [46] M.J. Hogan, and L. Feeney, “The ultrastructure of retinal blood vessel, 2. The small vessels,” *J Ultrastr Res.*, vol. 9, pp. 29–46, 1963.
- [47] T. Kuwabara, and D.G. Cogan, “Studies of retinal vascular patterns, Part I. Normal architecture,” *Arch Ophthalmol.*, vol. 64, no. 6, pp. 904–911, 1960.
- [48] C.J. Pournaras, E.R. Brandle, C.E. Riva, S.H. Hardarson, and E. Stefansson, “Regulation of retinal blood flow in health and disease,” *Prog Ret Eye Res.*, vol. 27, no. 3, pp. 284–330, 2006.
- [49] S. Schroder, M. Brab, G.W. Schmid-Schonbein, M. Reim, and H. Schmid-Schnbein, “Microvascular network topology of the human retinal vessels,” *Fortschr Ophthalmol.*, vol. 87, pp. 52–58, 1990.
- [50] A.K. Sjølie, R. Klein, M. Porta, T. Orchard, J. Fuller, H.H. Parving, R. Bilous, S. Aldington, and N. Chaturvedi, “Retinal microaneurysm count predicts progression and regression of diabetic retinopathy. Post-hoc results from the DIRECT Programme,” *Diabet Med.*, vol. 28, no. 3, pp. 345–351, 2011.
- [51] G.H. Bresnick, D.B. Mukamel, J.C. Dickinson, and D.R. Cole, “A screening approach to the surveillance of patients with diabetes for the presence of vision-threatening retinopathy,” *Ophthalmology*, vol. 107, no. 1, pp. 19–24, 2000.
- [52] S.C. Lee, E.T. Lee, R.M. Kingsley, Y. Wang, D. Russell, R. Klein, and A. Warn, “Comparison of diagnosis of early retinal lesions of diabetic retinopathy between a computer

- system and human experts,” *Arch Ophthalmol.*, vol. 119, no. 4, pp. 509–515, 2001.
- [53] E.M. Kohner, I.M. Stratton, S.J. Aldington, R.C. Turner, and D.R. Matthews, “Microaneurysms in the development of diabetic retinopathy (UKPDS 42). UK Prospective Diabetes Study Group,” *Diabetologia*, vol. 42, pp. 1107–1112, 1999.
- [54] R. Klein, S.M. Meuer, S.E. Moss, and B.E. Klein, “The relationship of retinal microaneurysm counts to the 4-year progression of diabetic retinopathy,” *Arch Ophthalmol.*, vol. 107, pp. 1780–1785, 1989.
- [55] M. Lamard, G. Quelled, P.M. Josselin, G. Cazuguel, B. Cochener, and C. Roux, “Detection of lesions in retina photographs based on the wavelet transform,” Proc. in *International Conference of the IEEE Engineering in Medicine and Biology Society*, New York, USA, August 30–September 3, pp. 2435–2438, 2006.
- [56] A.D. Fleming, S. Philip, K.A. Goatman, J.A. Olson, and P.F. Sharp, “Automated microaneurysm detection using local contrast normalization and local vessel detection,” *IEEE Trans. Medical Imaging*, vol. 25, no. 9, pp. 1223–1232, 2006.
- [57] K.A. Goatman, M.J. Cree, J.A. Olson, J.V. Forrester, and P.F. Sharp, “Automated measurement of microaneurysm turnover,” *Invest Ophthalmol Vis Sci.*, vol. 44, no. 12, pp. 5335–5341, 2003.
- [58] T. Walter, P. Massin, A. Erginay, R. Ordonez, C. Jeulin, and J.C. Klein, “Automatic detection of microaneurysms in color fundus images,” *Medical Image Analysis*, vol. 11, no. 6, pp. 555–566, 2007.
- [59] T. Hellstedt, E. Vesti, and I. Immonen, “Identification of individual microaneurysms: a comparison between fluorescein angiograms and red-free and colour photographs,” *Graefes Arch Clin Exp Ophthalmol.*, vol. 234, Suppl. 1, S13–S17, 1996.
- [60] J. Moore, S. Bagley, G. Ireland, D. McLeod, and M.E. Boulton, “Three dimensional analysis of microaneurysms in the human diabetic retina,” *J Anat.*, vol. 194, no. 1, pp. 89–100, 1999.
- [61] S.S. Feman, “The natural history of the first clinically visible features of diabetic retinopathy,” *Trans Am Ophthalmol Soc.*, vol. 92, pp. 745–773, 1994.
- [62] T.R. Friberg, J. Lace, J. Rosenstock, and P. Raskin, “Retinal microaneurysm counts in diabetic retinopathy: colour photography versus fluorescein angiography,” *Can J*

- Ophthalmol.*, vol. 22, no. 4, pp. 226–269, 1987.
- [63] E.M. Kohner, and M. Sleightholm, “Does microaneurysm count reflect severity of early diabetic retinopathy?” *Ophthalmology*, vol. 93, no. 5, pp. 586–589, 1986.
- [64] C. Baudoin, F. Maneschi, G. Quentel, G. Soubrane, T. Hayes, G. Jones, and G. Coscas, E.M. Kohner, “Quantitative evaluation of fluorescein angiograms: microaneurysm counts,” *Diabetes*, vol. 32, Suppl. 2, pp. 8–13, 1983.
- [65] A.L. Coleman, J.A. Haller, and H.A. Quigley, “Determination of the real size of fundus objects from fundus photographs,” *J Glaucoma.*, vol. 5, no. 6, pp. 433–435, 1996.
- [66] R.L. Radius, “Anatomy of the optic nerve head and glaucomatous optic neuropathy,” *Surv Ophthalmol.*, vol. 32, no. 1, pp. 35–44, 1987.
- [67] A. Mistlberger, J.M. Liebmann, D.S. Greenfield, S.T. Hoh, H. Ishikawa, M. Marmor, and R. Ritch, “Assessment of optic disc anatomy and nerve fiber layer thickness in ocular hypertensive subjects with normal short-wavelength automated perimetry,” *Ophthalmology*, vol. 109, no. 7, pp. 1362-1366, 2002.
- [68] N.M. Sing, S.F. Anderson, and J.C. Townsend, “The normal optic nerve head,” *Optom Vis Sci.*, vol. 77, no. 6, pp. 293–301 2000.
- [69] A. Laterza, and A. Nappo, “Optic nerve: a concise review of the anatomy, pathophysiology and principal acquired disorders,” *Ital J Neurol Sci.*, vol. 8, no. 6, pp. 529–535, 1987.
- [70] R.S. Snell, and M.A. Lemp, *Clinical Anatomy of the Eye*, 2nd Edition, Wiley-Blackwell, 1997.
- [71] S. Ryan, M. McNicholas, and S.J. Eustace, *Anatomy for Diagnostic Imaging*, Saunders, 2004
- [72] E.A. Kelts, “The basic anatomy of the optic nerve and visual system (or, why Thoreau was wrong),” *NeuroRehabilitation*, vol. 27, no. 3, pp. 217–222, 2010.
- [73] D.F. Garway-Heath, and R.A. Hitchings, “Quantitative evaluation of the optic nerve head in early glaucoma,” *Br J Ophthalmol.*, vol. 82, pp. 352–361, 1998.
- [74] C. Reeves, and D. Taylor, “A history of the optic nerve and its diseases,” *Eye*, vol. 18, no. 11, pp. 1096–1109, 2004.
- [75] Optic disc, http://en.wikipedia.org/wiki/Optic_disc
- [76] S. Liu, and M. Silverman, “A practical guide to biometric security technology,” *IT*

- Professional*, vol. 3, no. 1, pp. 27–32, 2001.
- [77] B.L. Golden, B.E. Rollin, R.V. Switzer, and C.R. Comstock, “Retinal vasculature image acquisition apparatus and method,” U.S. Patent No. 6,766,041, 2004.
- [78] H. Farzin, H. Abrishami-Moghaddam, and M. Moin, “A novel retinal identification system,” *EURASIP Journal on Advances in Signal Processing*, vol. 2008, 10 pages, 2008.
- [79] M.D. Amiri, F.A. Tab, and W. Barkhoda, “Retina Identification Based on the Pattern of Blood Vessels Using Angular and Radial Partitioning,” Proc. in *Advanced Concepts for Intelligent Vision Systems*, Bordeaux, France, September 28–October 2, pp. 732–739, 2009.
- [80] Retinal scan, http://en.wikipedia.org/wiki/Retinal_scan
- [81] World Health Organization, “Prevention of blindness from diabetes mellitus,” 2006.
- [82] S Wild, R Sicree, G Roglic, A. Green, R. Sicree, and H. King, “Global prevalence of diabetes,” *Diabetes Care*, vol. 27, pp. 1047–1053, 2004.
- [83] P.J. Kertes, and T.M. Johnson, *Evidence Based Eye Care*, Lippincott Williams & Wilkins, 2007.
- [84] J.B. Saaddine, A.A. Honeycutt, K.M. Narayan, X. Zhang, R. Klein, and J.P. Boyle, “Projection of diabetic retinopathy and other major eye diseases among people with diabetes mellitus: United States, 2005–2050,” *Arch Ophthalmol.*, vol. 126, vol. 12, pp. 1740–1747, 2008.
- [85] Facts About Diabetic Retinopathy, <http://www.nei.nih.gov/health/diabetic/retinopathy.asp>
- [86] P. Zimmet, K.G.M.M. Alberti, and J. Shaw, “Global and societal implications of the diabetes epidemic,” *Nature*, vol. 414, pp. 782–787, 2001.
- [87] D.C. Klonoff, and D.M. Schwartz, “An economic analysis of interventions for diabetes,” *Diabetes Care.*, vol. 23, no. 3, pp. 390–404, 2000.
- [88] L.P. Aiello, T.W. Gardner, G.L. King, G. Blankenship, J.D. Cavallerano, F.L. Ferris, and R. Klein, “Diabetic retinopathy,” *Diabetes Care*, vol. 21, no. 1, pp. 143–156, 1998.
- [89] H. Leung, J.J. Wang, E. Rochtchina, T.Y. Wong, R. Klein, and P. Mitchell, “Impact of current and past blood pressure on retinal arteriolar diameter in an older population,” *J. Hypertens.*, vol. 22, no. 8, pp. 1543–1549, 2004.

- [90] P. Mitchell, H. Leung, J.J. Wang, E. Rochtchina, A.J. Lee, T.Y. Wong, and R. Klein, "Retinal vessel diameter and open-angle glaucoma: the Blue Mountains eye study," *Ophthalmology*, vol. 112, no. 2, pp. 245–250, 2005.
- [91] J.J. Wang, B. Taylor, T.Y. Wong, B. Chua, E. Rochtchina, R. Klein, and P. Mitchell, "Retinal vessel diameters and obesity: a population-based study in older persons," *Obesity*, vol. 14, no. 2, pp.206–214, 2006.
- [92] F. Badalà, K. Nouri-Mahdavi, D.A. Raoof, N. Leeprechanon, S.K. Law, and J. Caprioli, "Optic disc and nerve fiber layer imaging to detect glaucoma," *Am J Ophthalmol.*, vol. 144, no. 5, pp. 724–732, 2007.
- [93] F.A. Medeiros, L.M. Zangwill, C. Bowd, R.M. Vessani, R. Susanna, and R.N. Weinreb, "Evaluation of retinal nerve fiber layer, optic nerve head, and macular thickness measurements for glaucoma detection using optical coherence tomography," *Am J Ophthalmol.*, vol. 139, pp. 44–55, 2005.
- [94] H.A. Quigley, J. Katz, R.J. Derick, D. Gilbert, and A. Sommer, "An evaluation of optic disc and nerve fiber layer examinations in monitoring progression of early glaucoma damage," *Ophthalmology*, vol. 99, no. 1, pp. 19–28, 1992.
- [95] S. Ryu, S.L. Brown, A. Kolozsvary, J.R. Ewing, and J.H. Kim. "Noninvasive detection of radiation-induced optic neuropathy by manganese-enhanced MRI," *Radiat Res.*, vol. 157, no. 5, pp. 500–505, 2002.
- [96] D.H. Miller, D.G. Mac Manus, P.A. Bartlett, R. Kapoor, S.P. Morrissey, and I.F. Moseley, "Detection of optic nerve lesions in optic neuritis using frequency-selective fat-saturation sequences," *Neuroradiology*, vol. 35, no. 2, pp. 156–158 , 2003.
- [97] S.S. Hayreh, and R.M. Zahoruk, "Anterior ischemic optic neuropathy. VI. In juvenile diabetics," *Ophthalmologica*, vol. 182, no. 1, pp. 13–28, 1981.
- [98] L.N. Johnson, R.S. Hepler, and M.J. Bartholomew, "Accuracy of papilledema and pseudopapilledema detection: a multispecialty study," *J Fam Pract.*, vol. 33, no. 4, pp. 381–386, 1991.
- [99] R.W. Morris, J.M. Ellerbrock, A.M. Hamp, J.T. Joy, P. Roels, and C.N. Davis, "Advanced visual field loss secondary to optic nerve head drusen: Case report and literature review,"

- Optometry*, vol. 80, no. 2, pp. 83–100, 2009.
- [100] M. Niemeijer, M.D. Abramoff, and B. van Ginneken, “Automated localization of the optic disc and the fovea,” Proc. in *International Conference of the IEEE Engineering in Medicine and Biology Society*, Vancouver, Canada, August 20–24, pp. 3538–3541, 2008.
- [101] M. Niemeijer, M.D. Abramoff, and B. van Ginneken, “Segmentation of the optic disc, macula and vascular arch in fundus photographs,” *IEEE Trans. on Medical Imaging*, vol. 26, no. 1, pp. 116–127, 2007.
- [102] K.W. Tobin, E. Chaum, V.P. Govindasamy, and T.P. Karnowski, “Detection of anatomic structures in human retinal imagery,” *IEEE Trans. on Medical Imaging*, vol. 26, no. 12, pp. 1729–1739, 2007.
- [103] H.R. Taylor, and J.E. Keeffe, “World blindness: A 21st century perspective,” *Br J Ophthalmol.*, vol. 85, no. 3, pp. 261–266, 2001.
- [104] R. Klein, S.M. Meuer, S.E. Moss, and B.E. Klein, “Retinal microaneurysm counts and 10-year progression of diabetic retinopathy,” *Arch Ophthalmol.*, vol. 113, no. 11, pp. 1386–1391, 1995.
- [105] B. Zhang, L. Zhang, L. Zhang, and F. Karray, “Retinal vessel extraction by matched filter with first-order derivative of gaussian,” *Computers in Biology and Medicine*, vol. 40, no.4, pp. 438–445, 2010.
- [106] B. Zhang, X.Q. Wu, J. You, Q. Li, and F. Karray, “Detection of microaneurysms using multi-scale correlation coefficients,” *Pattern Recognition*, vol. 43, no. 6, pp. 2237–2248, 2010.
- [107] B. Zhang, X.Q. Wu, J. You, Q. Li, and F. Karray, “Hierarchical detection of red lesions in retinal images by multiscale correlation filtering,” Proc. in *SPIE Medical Imaging*, Orlando, USA, February 7–12, vol. 7260, 72601L, 2009.
- [108] M. Niemeijer, B. van Ginneken, M.J. Cree, A. Mizutani, G. Quellec, C.I. Sanchez, B. Zhang, R. Hornero, M. Lamard, C. Muramatsu, X. Wu, G. Cazuguel, J. You, A. Mayo, Q. Li, Y. Hatanaka, B. Cochener, C. Roux, F. Karray, M. Garcia, H. Fujita, and M.D. Abramoff, “Retinopathy online challenge: automatic detection of microaneurysms in digital color fundus photographs,” *IEEE Trans. on Medical Imaging*, vol. 29, no. 1, pp. 185–195, 2010.
- [109] B. Zhang, L. Zhang, J. You, and F. Karray, “Microaneurysm (MA) detection via sparse

- representation classifier with MA and non-MA dictionary learning,” Proc. in *International Conference on Pattern Recognition*, Istanbul, Turkey, August 23–26, pp. 277–280, 2010.
- [110] B. Zhang, F. Karray, and L. Zhang, “Sparse representation classifier for microaneurysm detection and retinal blood vessel extraction,” *Information Sciences*, under revision.
- [111] B. Zhang, F. Karray, and L. Zhang, “Microaneurysm detection based on centralized dictionary learning for sparse representation,” *Medical Image Analysis*, to be submitted.
- [112] B. Zhang, and F. Karray, “Detecting optic disc on asians by multi-scale gaussian filtering,” *Computers in Biology and Medicine*, submitted to.
- [113] B. Zhang, and F. Karray, “Optic disc detection by multi-scale gaussian filtering with scale production and a vessels’ directional matched filter,” Proc. in *International Conference on Medical Biometrics*, Hong Kong, China, June 28–30, pp. 173–180, 2010.
- [114] B. Zhang, and F. Karray, “Optic disc and fovea detection via multi-scale matched filters and a vessels’ directional matched filter,” Proc. in *International Conference on Autonomous and Intelligent Systems*, Povo de Varzim, Portugal, June 21–23, pp. 1–5, 2010.
- [115] F. Zana, and J.C. Klein, “Segmentation of vessel-like patterns using mathematical morphology and curvature evaluation,” *IEEE Trans. Image Processing*, vol. 10, no. 7, pp. 1010–1019, 2001.
- [116] S. Garg, J. Sivaswamy, and S. Chandra, “Unsupervised curvature-based retinal vessel segmentation,” Proc. in *IEEE International Symposium on Bio-Medical Imaging*, Washington D.C., USA, April 12–15, pp. 344–347, 2007.
- [117] A. Youssif, A. Ghalwash, and A. Ghoneim, “Optic disc detection from normalized digital fundus images by means of a vessels’ direction matched filter,” *IEEE Trans. on Medical Imaging*, vol. 27, no. 1, pp. 11–18, 2008.
- [118] H. Li, and O. Chutatape, “Automatic location of optic disc in retinal images,” Proc. in *International Conference on Image Processing*, Thessaloniki, Greece, October 7–10, vol. 2, pp. 837–840, 2001.
- [119] H. Li, and O. Chutatape, “A model-based approach for automated feature extraction in fundus images,” Proc. in *International Conference on Computer Vision*, Nice France, October 13–16, vol. 1, pp. 394–399, 2003.

- [120] R. Chrástek, M. Wolf, K. Donath, G. Michelson, and H. Niemann, "Optic disc segmentation in retinal images," Proc. in *Bildverarbeitung für die Medizin*, Leipzig, Germany, March 10–12, pp. 263–266, 2002.
- [121] M. Park, J.S. Jin, and S. Luo, "Locating the optic disc in retinal images," Proc. in *International Conference on Computer Graphics, Imaging and Visualization*, Sydney, Australia, July 26–28, pp. 141–145, 2006.
- [122] R.A. Abdel-Ghafar, and T. Morris, "Progress towards automated detection and characterization of the optic disc in glaucoma and diabetic retinopathy," *Med Inform Internet Med.*, vol. 32, no. 1, pp. 19–25, 2007.
- [123] S.F. Barrett, E. Naess, and T. Molvik, "Employing the hough transform to locate the optic disk," *Biomed. Sci. Instrum.*, vol. 37, pp. 81–86, 2001.
- [124] X. Zhu, and R.M. Rangayyan, "Detection of the optic disc in images of the retina using the hough transform," Proc. in *International Conference of the IEEE Engineering in Medicine and Biology Society*, Vancouver, Canada, August 20–24, pp. 3546–3549, 2008.
- [125] T. Walter, and J.C. Klein, "Segmentation of color fundus images of the human retina: detection of the optic disc and the vascular tree using morphological techniques," Proc. in *International Symposium on Medical Data Analysis*, Madrid, Spain, October 8–9, pp. 282–287, 2001.
- [126] J. Hajer, H. Kamel, and E. Nouredine, "Localization of the optic disk in retinal image using the "watersnake"," Proc. in *International Conference on Computer and Communication Engineering*, Kuala Lumpur, Malaysia, May 13–15, pp. 947–951, 2008.
- [127] M. Foracchia, E. Grisan, and A. Ruggeri, "Detection of optic disc in retinal images by means of a geometrical model of vessel structure," *IEEE Trans. on Medical Imaging*, vol. 23, no. 10, pp. 1189–1195, 2004.
- [128] R. Perfetti, E. Ricci, D. Casali, and G. Costantini, "Cellular neural networks with virtual template expansion for retinal vessel segmentation," *IEEE Transactions on Circuits and Systems II*, vol. 54, no. 2, pp. 141–145, 2007.
- [129] M. Cinsdikici, and D. Aydin, "Detection of blood vessels in ophthalmoscope images using MF/ant (matched filter/ant colony) algorithm," *Comput Methods Programs Biomed.*, vol. 96

- no. 2, pp. 85–95, 2009.
- [130] M. Al-Rawi, M. Qutaishat, and M. Arrar, “An improvement matched filter for blood vessel detection of digital retinal images,” *Computers in Biology and Medicine*, vol. 37, pp. 262–267, 2007.
- [131] L. Zhang, Q. Li, J. You, and D. Zhang, “A modified matched filter with double-sided thresholding for screening proliferative diabetic retinopathy,” *IEEE Trans. on Information Technology in Biomedicine*, vol. 13, no. 4, pp. 528–534, 2009.
- [132] Retinopathy Online Challenge, <http://roc.healthcare.uiowa.edu/>
- [133] J. Wright, A. Yang, A. Ganesh, S. Sastry, and Y. Ma, “Robust Face Recognition via Sparse Representation,” *IEEE Trans. on Pattern Analysis and Machine Intelligence*, vol. 31, no. 2, pp. 210–227, 2009.
- [134] C. Boyd, and L. Vandenberghe, *Convex Optimization*, Cambridge University Press, 2004.
- [135] R. Duda, P. Hart, and D. Stork, *Pattern Classification (2nd ed.)*, Wiley-Interscience, 2000.
- [136] T. Kauppi, V. Kalesnykiene, J.K. Kamaraniene, L. Lensu, I. Sorri, A. Raninen, R. Voutilainen, H. Uusitalo, H. Kalviainen, and J. Pietil, “The DIARETDB1 diabetic retinopathy database and evaluation protocol,” Proc. in *British Machine Vision Conference*, Warwick, UK, September 10–13, pp. 252–261, 2007.
- [137] DIARETDB1—Standard Diabetic Retinopathy Database, <http://www2.it.lut.fi/project/imageret/diaretdb1/>
- [138] S. Pradhan, S. Balasubramanian, and V. Chandrasekaran, “An Integrated Approach Using Automatic Seed Generation and Hybrid Classification for the Detection of Red Lesions in Digital Fundus Images,” Proc. in *International Conference on Computer and Information Technology Workshops*, Sydney, Australia, July 8–11, pp. 462–467, 2008.
- [139] G.B. Kande, T.S. Savithri, P.V. Subbaiah, and M.R.N. Tagore, “Detection of red lesions in digital fundus images,” Proc. in *International Symposium on Biomedical Imaging: From Nano to Macro*, Boston, USA, June 28–July 1, pp. 558–561, 2009.
- [140] C.S. Tsai, L. Zangwill, C. Gonzalez, I. Irak, V. Garden, R. Hoffman, and R.N. Weinreb, “Ethnic differences in optic nerve head topography,” *J. Glaucoma*, vol. 4, no. 4, pp. 248–257, 1995.

- [141] A.M. Mansour, “Racial variation of optic disc size,” *Ophthalmic Res.*, vol. 23, no. 2, pp. 67–72, 1991.
- [142] Y. Wang, L. Xu, L. Zhang, H. Yang, Y. Ma, and J.B. Jonas, “Optic disc size in a population based study in northern China: the Beijing Eye Study,” *Br J Ophthalmol.*, vol. 90, no. 3, pp. 353–356, 2006.
- [143] N. Cheung, S. Huynh, J.J. Wang, B. Taylor, F.M. Islam, S.M. Saw, T.Y. Wong, and P. Mitchell, “Relationships of retinal vessel diameters with optic disc, macular and retinal nerve fiber layer parameters in 6-year-old children,” *Invest Ophthalmol Vis Sci.*, vol. 49, no. 6, pp. 2403–2408, 2008.
- [144] N. Cheung, L. Tong, G. Tikellis, S.M. Saw, P. Mitchell, J.J. Wang, and T.Y. Wong, “Relationship of retinal vascular caliber with optic disc diameter in children,” *Invest Ophthalmol Vis Sci.*, vol. 48, no. 11, pp. 4945–4948, 2007.
- [145] C. Samarawickrama, S.C. Huynh, J.J. Wang, A. Pai, N. Joachim, G. Burlutsky, T.Y. Wong, and P. Mitchell, “Relationship between Retinal Structures and Retinal Vessel Caliber in Normal Adolescents,” *Invest Ophthalmol Vis Sci.*, vol. 50, no. 12, pp. 5619–5624, 2009.
- [146] T.T. Nguyen and T.Y. Wong, “Retinal vascular changes and diabetic retinopathy,” *Curr Diab Rep.*, vol. 9, no. 4, pp. 277–283, 2009.
- [147] C.P. Wilkinson, F.L. Ferris, R.E. Klein, P.P. Lee, C.D. Agardh, M. Davis, D. Dills, A. Kampik, R. Pararajasegaram, and J.T. Verdaguer, “Proposed international clinical diabetic retinopathy and diabetic macular edema disease severity scales,” *Ophthalmology*, vol. 110, no. 9, pp. 1677–1682, 2003.
- [148] K.W. Tobin, E. Chaum, V.P. Govindasamy, T.P. Karnowski, and O. Sezer, “Characterization of the optic disc in retinal imagery using a probabilistic approach,” Proc. in *SPIE’s International Symposium on Medical Imaging*, San Diego, USA, February 11–16, pp. 1088–1097, 2006.
- [149] M.D. Abramoff, and M. Niemeijer, “The automatic detection of the optic disc location in retinal images using optic disc location regression,” Proc. in *International Conference of the IEEE Engineering in Medicine and Biology Society*, New York, USA, August 30–September 3, pp. 4432–4435, 2006.

- [150] H. Kobatake, and Y. Yoshinaga, "Detection of spicules on mammogram based on skeleton analysis," *IEEE Trans. Medical Imaging*, vol. 15, no. 3, pp. 235–245, 1996.
- [151] H. Kobatake, and M. Murakami, "Adaptive filter to detect rounded convex regions: iris filter," Proc. in *International Conference on Pattern Recognition*, Vienna, Austria, August 25–29, pp. 340–344, 1996.
- [152] A.D. Fleming, K.A. Goatman, S. Philip, G.J. Williams, G.J. Prescott, G.S. Scotland, P. McNamee, G.P. Leese, W.N. Wykes, P.F. Sharp, J.A. Olson, and Scottish Diabetic Retinopathy Clinical Research Network, "The role of haemorrhage and exudate detection in automated grading of diabetic retinopathy," *Br J Ophthalmol.*, vol. 94, no. 6, pp. 706–711, 2010
- [153] S.J. Chen, P. Chou, A.F. Lee, F.L. Lee, W.M. Hsu, J.H. Liu, and T.H. Tung, "Microaneurysm number and distribution in the macula of Chinese type 2 diabetics with early diabetic retinopathy: a population-based study in Kinmen, Taiwan," *Acta Diabetol.*, vol. 47, no. 1, pp. 35-41, 2010.
- [154] X. Xie, L. Xu, H. Yang, S. Wang, and J.B. Jonas. "Frequency of diabetic retinopathy in the adult population in China: the Beijing Eye Study 2001," *Int Ophthalmol.*, vol. 29, no. 6, pp. 485-493, 2009.
- [155] M.C. Diamond, and A.B. Scheibel, "Neuroscience in China," *Exp Neurol.*, vol. 92, no. 3, pp. 461–466, 1986.
- [156] Y. Wang, L. Xu, L. Hu, Y. Wang, H. Yang, and J.B. Jonas, "Frequency of optic disk hemorrhages in adult chinese in rural and urban china: the Beijing eye study," *Am J Ophthalmol.*, vol. 142, no. 2, pp. 241–246, 2006.
- [157] Q.S. You, L. Xu, Y.X. Wang, and J.B. Jonas, "Prevalence of optic disc drusen in an adult Chinese population: the Beijing Eye Study," *Acta Ophthalmol.*, vol. 87, no. 2, pp. 227–228, 2009.
- [158] E. Ojaimi, T.T. Nguyen, R. Klein, F.M. Islam, M.F. Cotch, B.E. Klein, J.J. Wang, and T.Y. Wong, "Retinopathy Signs in People without Diabetes The Multi-Ethnic Study of

- Atherosclerosis,” *Ophthalmology.*, Nov 3, 2010.
- [159] H.H. Liu, L. Xu, Y.X. Wang, S. Wang, Q.S. You, and J.B. Jonas, “Prevalence and progression of myopic retinopathy in Chinese adults: the Beijing Eye Study,” *Ophthalmology.*, vol. 117, no. 9, pp. 1763–1768, 2010.
- [160] L.S. Lim, E. Lamoureux, S.M. Saw, W.T. Tay, P. Mitchell, and T.Y. Wong, “Are myopic eyes less likely to have diabetic retinopathy?” *Ophthalmology.*, vol. 117, no. 3, pp. 524–530, 2010.
- [161] A.K. Aralikatti, A. Mitra, A.K. Denniston, M.S. Haque, A.K. Ewer, and L. Butler, “Is ethnicity a risk factor for severe retinopathy of prematurity?” *Arch Dis Child Fetal Neonatal Ed.*, vol. 95, no. 3, F174–176, 2010.
- [162] X.W. Xie, L. Xu, J.B. Jonas, and Y.X. Wang, “Prevalence of diabetic retinopathy among subjects with known diabetes in China: the Beijing Eye Study,” *Eur J Ophthalmol.*, vol. 19, no. 1, pp. 91–99, 2009.